ISSN 2518-7198 (Print)
ISSN 2663-5089 (Online)

BULLETIN
OF THE KARAGANDA UNIVERSITY

PHYSICS
Series

2025 • Volume 30 • Issue 1(117)

ISSN 2663-5089 (Online)
ISSN 2518-7198 (Print)
Индексі 74616
Индекс 74616

ҚАРАҒАНДЫ УНИВЕРСИТЕТІНІҢ ХАБАРШЫСЫ

ВЕСТНИК КАРАГАНДИНСКОГО УНИВЕРСИТЕТА

BULLETIN OF THE KARAGANDA UNIVERSITY

ФИЗИКА сериясы

Серия ФИЗИКА

PHYSICS Series

2025

30-том • 1(117)-шығарылым
Том 30 • Выпуск 1(117)
Volume 30 • Issue 1(117)

1996 жылдан бастап шығады
Издается с 1996 года
Founded in 1996

Жылына 4 рет шығады
Выходит 4 раза в год
Published 4 times a year

Қарағанды / Караганда / Karaganda
2025

Редакцияның мекенжайы: 100024, Қазақстан, Қарағанды қ., Университет к-сі, 28
E-mail: vestnikku@gmail.com; karabekova71@mail.ru
Сайты: physics-vestnik.ksu.kz

Қарағанды университетінің хабаршысы. «Физика» сериясы. — 2025. — 30-т., 1(117)-шығ. — 88 б. — ISSN 2518-7198 (Print). ISSN 2663-5089 (Online).

Меншік иесі: «Академик Е.А. Бөкетов атындағы Қарағанды университеті» КЕАҚ.

Қазақстан Республикасы Ақпарат және қоғамдық даму министрлігімен тіркелген. 30.09.2020 ж. № KZ38VPY00027378 қайта есепке қою туралы куәлігі.

Басуға 30.03.2025 ж. қол қойылды. Пішімі 60×84 1/8. Қағазы офсеттік. Көлемі 11,0 б.т. Таралымы 200 дана. Бағасы келісім бойынша. Тапсырыс № 8.

«Акад. Е.А. Бөкетов ат. Қарағанды ун-ті» КЕАҚ баспасының баспаханасында басылып шықты.
100024, Қазақстан, Қарағанды қ., Университет к-сі, 28. Тел. (7212) 35-63-16. E-mail: izd_karu@mail.kz

Адрес редакции: 100024, Казахстан, г. Караганда, ул. Университетская, 28
E-mail: vestnikku@gmail.com; karabekova71@mail.ru
Сайт: physics-vestnik.ksu.kz

Исполнительный редактор

д-р PhD **Г.Б. Саржанова**

Корректоры

С.С. Балкеева, И.Н. Муртазина

Компьютерная верстка

В.В. Бутяйкин

Вестник Карагандинского университета. Серия «Физика». — 2025. — Т. 30, вып. 1(117). — 88 с. — ISSN 2518-7198 (Print). ISSN 2663-5089 (Online).

Собственник: НАО «Карагандинский университет имени академика Е.А. Букетова».

Зарегистрирован Министерством информации и общественного развития Республики Казахстан. Свидетельство о постановке на переучет № KZ38VPY00027378 от 30.09.2020 г.

Подписано в печать 30.03.2025 г. Формат 60×84 1/8. Бумага офсетная. Объем 11,0 п.л. Тираж 200 экз. Цена договорная. Заказ № 8.

Отпечатано в типографии издательства НАО «Карагандинский университет им. акад. Е.А. Букетова». 100024, Казахстан, г. Караганда, ул. Университетская, 28. Тел.(7212) 35-63-16. E-mail: izd_karu@mail.kz

Postal address: 28, University Str., 100024, Karaganda, Kazakhstan
E-mail: vestnikku@gmail.com; karabekova71@mail.ru
Web-site: physics-vestnik.ksu.kz

Bulletin of the Karaganda University. "Physics" Series. — 2025. — Vol. 30, Iss. 1(117). — 88 p. — ISSN 2518-7198 (Print). ISSN 2663-5089 (Online).

Proprietary: NLC "Karagandy University of the name of academician E.A. Buketov".

Registered by the Ministry of Information and Social Development of the Republic of Kazakhstan. Rediscount certificate No. KZ38VPY00027378 dated 30.09.2020.

Signed in print 30.03.2025. Format 60×84 1/8. Offset paper. Volume 11,0 p.sh. Circulation 200 copies. Price upon request. Order № 8.

Printed in the Publishing house of NLC "Karagandy University of the name of acad. E.A. Buketov".
28, University Str., Karaganda, 100024, Kazakhstan. Tel. (7212) 35-63-16. E-mail: izd_karu@mail.kz

МАЗМҰНЫ – СОДЕРЖАНИЕ – CONTENTS

КОНДЕНСАЦИЯЛАНҒАН КҮЙДІҢ ФИЗИКАСЫ
ФИЗИКА КОНДЕНСИРОВАННОГО СОСТОЯНИЯ
PHYSICS OF THE CONDENSED MATTER

ТЕХНИКАЛЫҚ ФИЗИКА
ТЕХНИЧЕСКАЯ ФИЗИКА
TECHNICAL PHYSICS

ЖЫЛУФИЗИКАСЫ ЖӘНЕ ТЕОРИЯЛЫҚ ЖЫЛУТЕХНИКАСЫ
ТЕПЛОФИЗИКА И ТЕОРЕТИЧЕСКАЯ ТЕПЛОТЕХНИКА
THERMOPHYSICS AND THEORETICAL THERMOENGINEERING

Article
https://doi.org/10.31489/2025PH1/6-12
UDC 539.261, 539.193, 539.194

Received: 10.06.2024
Accepted: 24.10.2024

K.B. Kopbalina[1*], A.S. Makhmutova[2], D.M. Turdybekov[3],
M.B. Smirnov[4], N.Kh. Ibrayev[3]

[1]Karaganda Buketov University, Kazakhstan;
[2]Karaganda Medical University, Kazakhstan;
[3]Abylkas Saginov Karaganda Technical University, Kazakhstan;
[4]Saint Petersburg State University, Russian Federation
*(*Corresponding author's e-mail: kopbalina82@mail.ru)*

Quantum Chemical Study of the Structure and Properties of a Quinolysine Alkaloid Derivative Molecule

Derivatives of quinolisidine alkaloids obtained from plants of the genus *Lupinus* and *Anabasis* is one of such important compounds from the point of view of searching for new biologically active substances. The presence of the primary alcoholic group allows obtaining various modifications of lupinin derivatives. The task of complex study of the spatial structure of quinolisidine derivatives molecules, pathways and obstacles of their conformational transitions, conformational states, and reactivity data remains relevant. Therefore, in continuation of the study of the conformational states of these derivatives, quantum-chemical calculations of the molecule 1-((4-(4-(*m*-tolyl)-1H-1,2,3-triazol-1-yl)methyl)octahydro-1H-quinolysine were performed. Geometrical properties of this molecule, obtained as a result of quantum chemical calculations, were analyzed and compared with experimental data of X-ray diffraction analysis. According to the results of the conformational analysis, conducted by rotating along the labile C12-C13 and C10-N2 bonds, the most favorable conformational states of the molecule were determined. It was shown that the localization of the boundary molecular orbitals falls on the 1-ethyl-4-(*m*-tolyl)-1H-1,2,3-triazole substituent at C12 and C10 atoms, which suggests its participation in the subsequent modification reactions carried out in the search for new biologically active substances.

Keywords: quantum chemical calculations, alkaloids, computer modeling, quinolysine derivative, conformational analysis, thermodynamic stability, lupinine derivatives, X-ray structure analysis

Introduction

Among various lupinine derivatives, compounds with biological activities that are not specific for compounds of this class (antispasmodic, antiarrhythmic, hepatoprotective, analgesic, cholinergic, insecticidal, antioxidant, etc.) are regularly encountered. This has attracted the attention of many researchers to study comprehensively and also to design more complex structures of these derivatives to study the structure-activity relationship.

One of the most effective methods for studying complex systems is computer modeling. Computer modeling methods are aimed at solving various problems and consist in performing a series of computational experiments on a computer. The purpose of these experiments is to analyze, interpret, and compare the results of the modeling with the specific behavior of the object under study. If necessary, the model is refined on the basis of the data obtained.

Molecular modeling is the process of creating a computer model of an object by transferring its spatial coordinates. Information about the initial geometry can be obtained in several ways: by extracting data from the X-ray diffraction database, by searching libraries for standard geometries, or by building structural models using various software tools.

The activity of a molecule in chemical reactions depends mainly on its composition, structure and energy properties. The prediction of reaction centers of organic molecules is an important and urgent task. Using modern quantum chemical methods, chemists can design experimental studies and carry out targeted synthesis of important chemical products.

Research Methods

The object of work is the molecule of lupinine alkaloid derivative 1-((4-(m-tolyl)-1H-1,2,3-triazol-1-yl)methyl)octahydro-1H-quinolysine (*molecule 1*) (Fig. 1) synthesized earlier by the authors [1].

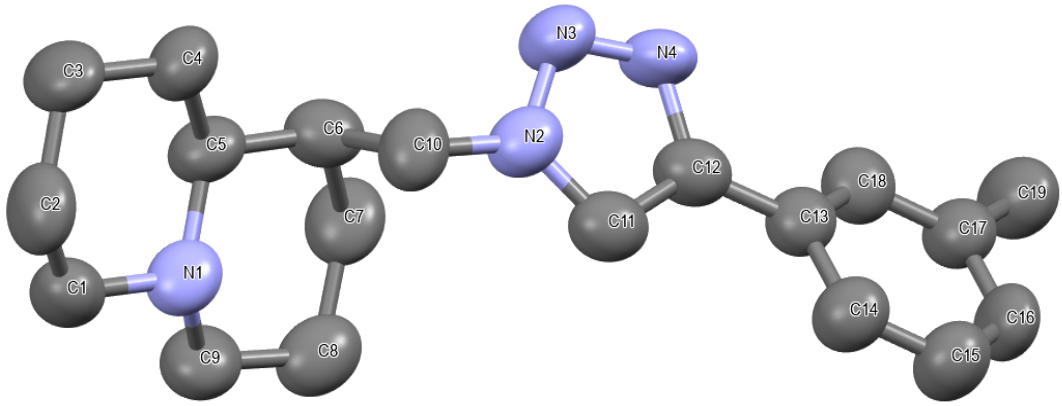

Figure 1. 3D structure of ((4-(m-tolyl)-1H-1,2,3-triazol-1-yl)methyl)octahydro-1H-quinolysine (1)

Nowadays, there is a sufficient number of free and commercial quantum chemistry programs, such as GAMESS, NWChem, HyperChem, VASP, Quantum Espresso, CRYSTAL, etc., for calculating organic molecules [2–3].

For the quantum-chemical study of molecule **1** we used the non-empirical DFT B3LYP density functional method using the valence-splitting basis set 3-21. To take into account the possibility of displacement of the electron density distribution center from the nucleus (polarization of atomic orbitals), we included a *d*-type polarization function in the basis set. The use of polarization basis functions allows us to correctly describe the energy and geometrical characteristics of organic compounds, including those with heteroatoms, which are present in the molecule under study.

The optimization of the geometry of molecule 1 was performed using the keywords Opt+freg. Opt — means that it is necessary to optimize the configuration of the molecule, i.e. during the optimization process, according to the applied method of extremum search, the program will change the bond lengths and valence angles of the studied structure until a stationary point — the most stable state of the molecule — is found. The keyword Freg was used by us to calculate the thermodynamic properties of molecules, as well as to determine the type of the stationary point (minimum or saddle point).

To find the most favorable conformational states, we used the keyword Scan, with opt=(modredundant, maxcycles=1000) selected in the problem section, and the corresponding dihedral angle after the coordinates by a blank line labeled with the letter D and the four atom numbers of that angle. We used modredundant for incomplete optimization.

Results and discussions

The first step of study was to optimize the geometry of *Molecule 1* — to find the minimum of total energy in all geometrical parameters.

In the course of studying the spatial structure of *Molecule 1*, we compared its geometric properties with X-ray diffraction (XRD) data, as well as with the data of the molecule 1-((4-(4-(3-methoxyphenyl)-1H-1,2,3-

triazol-1-yl)methyl)octahydro-1H-quinolysine (*Molecule 2*) [4], which has a similar structure and has been studied by us previously [5].

The geometric properties of *Molecules 1* and *2* obtained from quantum chemical calculations are close to the corresponding XRD data, which indicates the correctness of the calculated data. The values of the torsion angles are given in Table 1.

Table 1

Values of torsional angles in *Molecules 1* and *2*

Torsional angles	*Molecule 1*		*Molecule* 2	
	XRD	B3LyP 3/21	XRD	B3LyP 3/21
C1-N1-C5-C4	59.2(1)	53.4	–58.0(9)	59.2
C9-N1-C5-C4	176.8(1)	175.2	–176.6(9)	–175.4
C11-N2-C10-C6	–120.8(1)	–129.9	124(1)	–138.5
C10-N2-C11-C12	177.1(1)	–179.5	–176.2(8)	–178.1
N3-N4-C12-C11	0.0(1)	0.2	0(1)	0.2
C2-C3-C4-C5	57.0(2)	57.3	–57(1)	55.0
C3-C4-C5-N1	–58.2(1)	–54.8	59(1)	–56.3
C3-C4-C5-C6	177.5(1)	–176.8	–175.0(9)	–178.0
C4-C5-C6-C7	179.4(1)	–177.0	179.3(8)	112.0
C4-C5-C6-C10	55.2(1)	60.0	–54(1)	–124.1
C5-C6-C7-C8	–54.0(1)	–56.9	54(1)	58.4
C5-C6-C10-N2	175.9(1)	168.4	179.2(7)	61.1
N2-C11-C12-N4	0.7(1)	–0.1	–0(1|)	0.0
N2-C11-C12-C13	–179.8(1)	–179.9	178.1(9)	–179.7
C11-C12-C13-C18	151.6(1)	179.9	160(1)	179.7

The difference in the values of the torsion angles C4-C5-C6-C7, C4-C5-C6-C10 and C5-C6-C10-N2 can be explained by the fact that all the quantum chemical calculations are carried out in the liquid phase of the molecules, whereas the XRD data are obtained in the solid state. Therefore, molecule 2 adopts an energetically more favourable conformation upon crystallization.

To determine the most favorable conformational states of *Molecule 1*, conformational analysis was performed by rotating around the labile C12-C13 (Fig. 2) and C10-N2 (Fig. 3) bonds.

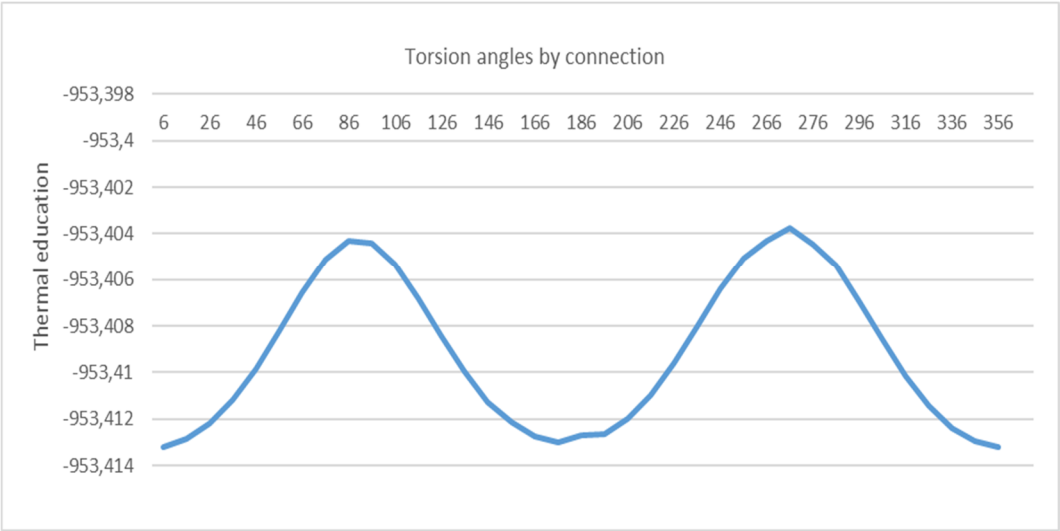

Figure 2. Dependence of the total energy of *Molecule 1* on the rotation along the C12-C13 bond

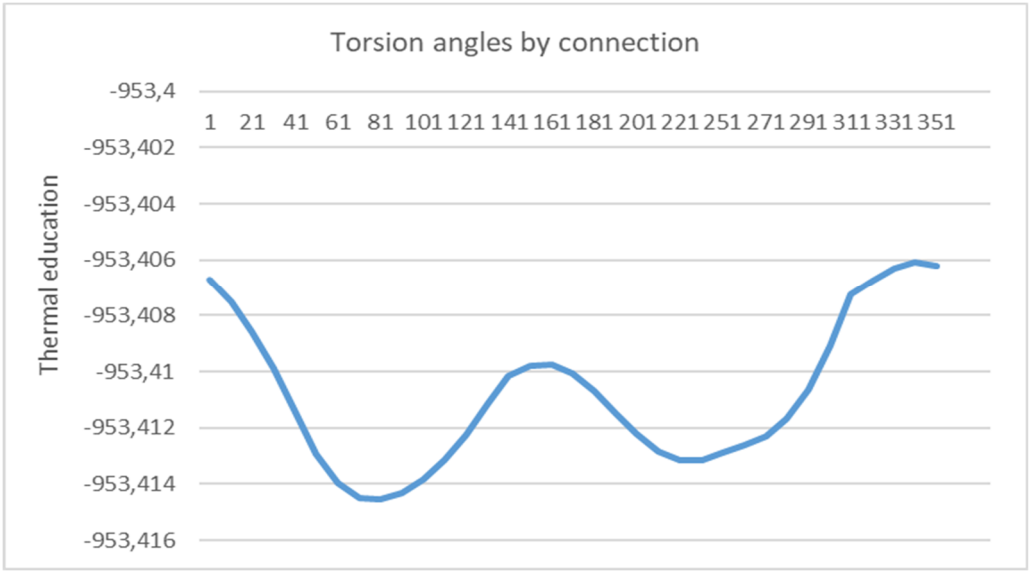

Figure 3. Dependence of the total energy of *Molecule 1* on the rotation along the C10-N2 bond

From the analysis of the obtained data we can conclude that the most thermodynamically favorable (having the minimum electron energy of the molecule) conformational states of the free *Molecule 1* takes at the values of the torsional angle C11-C12-C13-C14 355° and 176° and at values of the torsional angle C6-C10-N2-C11 71° and 221° (–953.41HF) –2502 kJ/mol. The conformation along the C12-C13 and C10-N2 bonds has an energy minimum in the range of -2502 kJ/mol.

It is believed that the reactivity of a molecule depends on its boundary molecular orbitals (MOs): the highest occupied and the lowest free orbitals (HBMOs and LFMOs) [6]. One of the most important properties of the MOs is the boundary electron density, i.e. the electron density on the individual atoms of the molecule involved in the reaction. According to this theory, a reaction between molecules is most likely to occur when there is a maximum overlap of boundary MOs. This process results in a charge transfer from the highest occupied orbital of the donor (gives) to the lowest free orbital of the acceptor (receives).

It is known that the reactivity of a molecule is characterized by the values and localization of HBMOs (highest occupied molecular orbital) and LFMOs (lowest free molecular orbital) [7]. The energy characteristics and localization of MBOs (molecular boundary orbitals) have therefore been calculated.

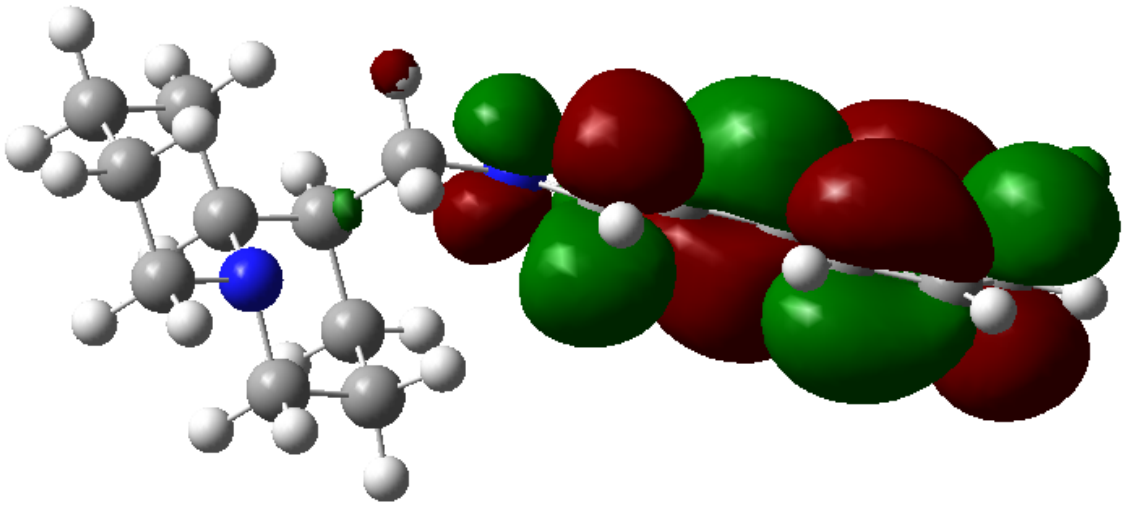

Figure 4. Localization of MBOs in molecule 1

Figure 4 shows that the localization of MBOs in molecule 1 falls on the substituent — 1-((4-(*m*-tolyl)-1H-1,2,3-triazol-1-yl)methyl. Therefore, it can be assumed that further reactions of synthesis of new derivatives of molecule 1 will take place with participation of this substituent.

The "hardness" or "softness" of the studied molecules can be estimated from the values of HBMO and LFMO energies (Table 2). The "hardness η/softness" of molecules according to the Pearson criterion can be calculated on the basis of the formula η = (LFMO – HBMO)/2, and then S =1/(2η) = 1/(LFMO – HBMO). The application of these formulas implies that the studied molecular systems are "rigid" reactants, since they have an energy gap of more than 1 eV between LFMO and HBMO [8]. The calculated rigidity (Ƞ) indicates that this molecule is quite rigid, which in turn indicates its low reactivity and high electronic stability. Sufficient thermodynamic stability is indicated by the value of heat of formation also presented in Table 2.

Table 2

The energy properties of *Molecule 1*

Basis	B3LYP/3-21
ΔH, hartree, eV	–953.413251
HBMO, eV	–9.2326
LFMO, eV	–8.6188
Ƞ, eV	–3.6951

Conclusion

Thus, as a result of quantum chemical calculations performed by density functional theory methods B3LYP/6-21G*:

– geometrical parameters of conformational states of molecule 1 with values of torsional angles C11-C12-C13-C14 355° and 176°, and C6-C10-N2-C11 90° and 230° were determined;

– a satisfactory agreement between the computational-theoretical and experimental structural data is shown;

– the studied molecule was found to exhibit low reactivity and high electronic stability.

These calculations will allow further modelling of the chemical properties of molecules for the subsequent synthesis and search for new drugs based on quinolizidine derivatives.

References

1 Sparatore, A., Cagnotto, A., & Sparatore, F. (1999). Quinolizidinyl derivatives of 2,3-dihydro-2-oxo-1H-benzimidazole-1-carboxylic acid and 1-homolupinanoyl benzimidazolones as ligands for 5-HT3 and 5-HT4 receptors. *Farmaco*, 54, 248–254.

2 Stewart, J. J. (2007). Optimization of parameters for semiempirical methods V: Modification of NDDO approximations and application to 70 elements. *Journal of Molecular modeling, 13*, 1173–1213.

3 Frisch, M. J. (2009). Gaussian 09, Revision D. 01/Gaussian.

4 Nurmaganbetov, Zh.S., Fazylov, S.D., Turdybekov, K.M., Minayeva, Ye.V., & Khabdolda, G. (2022). Synthesis and Structure of 4-Substituted (1S,9aR)-1-[(1,2,3-triazol-1-yl)methyl]octahydro-1H-quinolysines of Lupinine. *Bulletin of the Karaganda University Chemistry Series, 106*(2), 12–22.

5 Kopbalina, K.B., Makhmutova, A.S., Turdybekov, D.M., Turdybekov, K.M., & Tolenova, G.K. (2023). Quantum-chemical study of the structure and properties of molecule of the lupinine alkaloid derivative. *Eurasian Physical Technical Journal, 4*, 33–38.

6 Allen, F.H., Kennard, O., Watson, D.G., Brammer, L., Orpen, A.G., & Taylor, R. (1987). Tables of bond lengths determined by X-ray and neutron diffraction. *J. Chem. Soc. Perkin Trans.*, 2, 1–19.

7 Shiryaev A.K. (2020). Quantum chemistry: textbook. Samara: Samara State Technical University, 134 p. [in Russian].

8 Tsyshevsky, R.V. (2012). *Quantum-chemical calculations of chemical reaction mechanisms: textbook*. Kazan: Kazanskii Natsionalnyi Issledovatelskii Tekhnologicheskii Universitet, 88 p. [in Russian].

Қ.Б. Копбалина, А.С. Махмутова, Д.М. Турдыбеков,
М.Б. Смирнов, Н.Х. Ибраев

Хинолизин алкалоидты туынды молекуласының құрылымы мен қасиеттерін кванттық химиялық зерттеу

Lupinus және *Anabasis* тұқымдас өсімдіктерден алынған хинолизидин алкалоидтарының туындылары жаңа биологиялық белсенді заттарды іздеу тұрғысынан маңызды қосылыстардың бірі. Бастапқы спирттік тобының болуы лупинин туындыларының әртүрлі модификацияларын алуға мүмкіндік береді. Хинолизидин туындыларының молекулаларының кеңістіктік құрылымын, олардың конформациялық ауысуларының жолдары мен кедергілерін, конформациялық күйлер мен реакциялық қабілеттілігін кешенді зерттеу міндеті маңызды. Сондықтан, бұл туындылардың конформациялық күйін зерттеуді жалғастыра отырып, 1-((4-(*м*-толил)–1Н-1,2,3-триазол-1-ил)метил)октагидро–1Н-хинолизин молекуласына кванттық-химиялық есептеулер жүргізілді. Кванттық-химиялық есептеулер нәтижесінде алынған бұл молекуланың геометриялық сипаттамалары талданып, рентгендік құрылымдық талдаудың эксперименттік мәліметтерімен салыстырылған. C12-C13 және C10-N2 лабильді байланыстары бойымен айналу арқылы жүргізілген конформациялық талдау нәтижелері бойынша молекуланың ең тиімді конформациялық күйлері анықталды. Шекаралық молекулалық орбитальдардың локализациясы C12 және C10 атомдарындағы 1-этил-4-(*м*-толил)-1Н-1,2,3-триазол алмастырғышында болатындығы көрсетілген, бұл оның жаңа биологиялық белсенді заттарды іздеу үшін жүргізілетін кейінгі модификация реакцияларына қатысуын болжайды.

Кілт сөздер: кванттық химиялық есептеулер, алкалоидтар, компьютерлік модельдеу, хинолизин туындысы, конформациялық талдау, термодинамикалық тұрақтылық, лупинин туындылары, рентгендік құрылымдық талдау

К.Б. Копбалина, А.С. Махмутова, Д.М. Турдыбеков,
М.Б. Смирнов, Н.Х. Ибраев

Квантово-химическое исследование структуры и свойств молекулы производного хинолизинового алкалоида

Производные хинолизидиновых алкалоидов, полученные из растений рода *Lupinus* и *Anabasis*, с точки зрения поиска новых биологически активных веществ, являются важными соединениями. Наличие первичной спиртовой группы позволяет получать различные модификации производных лупинина. Актуальной остается задача комплексного изучения пространственной структуры молекул производных хинолизидина, а также путей и препятствий их конформационных переходов и состояний, определяемых реакционной способностью. В продолжение изучения конформационных состояний этих производных были проведены квантово-химические расчеты молекулы 1-((4-(*m*-толил)–1Н-1,2,3-триазол-1-ил)метил)октагидро–1Н-хинолизина. Геометрические характеристики данной молекулы, полученные в результате квантово-химических расчетов, проанализированы и сопоставлены с экспериментальными данными рентгеноструктурного анализа. По результатам конформационного анализа, осуществленного путем вращения вдоль лабильных связей C12-C13 и C10-N2, были установлены наиболее стабильные конформационные состояния молекулы. Показано, что локализация граничных молекулярных орбиталей приходится на 1-этил-4-(*m*-толил)-1Н-1,2,3-триазоловый заместитель при атомах C12 и C10, что предполагает его участие в последующих реакциях модификации, проводимых для поиска новых биологически активных веществ.

Ключевые слова: квантово-химические расчеты, алкалоиды, компьютерное моделирование, производное квинолизина, конформационный анализ, термодинамическая стабильность, производные лупинина, рентгеновский структурный анализ

Information about the authors

Kopbalina, Kymbat — Master of Physics, Abylkas Saginov Karaganda Technical University, N. Nazarbayev str., 56, 100010 Karaganda, Kazakhstan; e-mail: kopbalina82@mail.ru; https://orcid.org/0000-0001-6378-9756

Makhmutova, Almagul — Candidate of chemical sciences, Karaganda Medical University, Gogol str., 40, 100010, Karaganda, Kazakhstan; e-mail: Almagul_312@mail.ru; https://orcid.org/0000-0002-0194-8739

Turdybekov, Dastan — Candidate of chemical sciences, Abylkas Saginov Karaganda Technical University, N. Nazarbayev str., 56, 100010, Karaganda, Kazakhstan; e-mail: turdas@mail.ru; https://orcid.org/0000-0002-0245-022X

Smirnov, Mikhail — Doctor of physical and mathematical sciences, Professor of Saint Petersburg State University, Saint Petersburg, Russian Federation; e-mail: smirnomb@rambler.ru; https://orcid.org/0000-0002-4292-1989

Ibrayev, Niyazbek — Doctor of physical and mathematical sciences, Professor, Karaganda Buketov University, Karaganda, Kazakhstan; e-mail: niazibraev@mail.ru; https://orcid.org/0000-0002-5156-5015

Article
https://doi.org/10.31489/2025PH1/13-19
UDC:538.91, 538.958
Received: 05.07.2024
Accepted: 10.10.2024

A. Bakytkyzy[1], Z.T. Karipbayev[1*], Y. Suchikova[2], A.B. Usseinov[1], T.A. Koketai[3], N.K. Mussabek[3], A.I. Popov[4]

[1]*L.N. Gumilyov Eurasian National University, Astana, Kazakhstan;*
[2]*Berdyansk State Pedagogical University, Ukraine;*
[3]*Karaganda Buketov University, Kazakhstan;*
[4]*University of Latvia, Riga, Latvia*
*(*Corresponding author's e-mail: karipbayev_zht_1@enu.kz)*

Exploration of β-Ga_2O_3 Ceramics Synthesized via Solid-State Method

β-Ga_2O_3 ceramic was synthesized using the solid-state method, a well-established technique for creating ceramic materials with controlled composition and structure. The process began by pressing gallium oxide (Ga_2O_3) powder into a unified form, ensuring even distribution and compactness of the material. This pressed form was then subjected to annealing at 1400 °C for 10 hours, a critical step facilitating the formation of a stable and crystalline β-Ga_2O_3 phase. Energy dispersive X-ray analysis (EDS) was employed to investigate the elemental composition of the synthesized β-Ga_2O_3ceramic. The analysis confirmed that the material closely adhered to the ideal stoichiometric ratio of oxygen to gallium (O/Ga) at 3:2, ensuring the purity and consistency of the ceramic. The optical properties of the β-Ga_2O_3 ceramics were thoroughly studied. Surface morphology analysis and elemental composition measurements were complemented by the recording of photoluminescence excitation and transmission spectra at successive wavelengths ranging from 200 to 800 nm. These spectra provided valuable insights into the material's electronic and optical behavior. Both the synthesized β-Ga_2O_3ceramic and commercial β-Ga_2O_3 crystals exhibited distinct photoluminescence peaks in the blue (~2.7 eV) and ultraviolet (3.3, 3.4, 3.8 eV) spectral ranges.

Keywords: synthesis, β-Ga_2O_3 ceramics, photoluminescence, annealing, stoichiometric ratios, morphology, elemental composition, point defects

Introduction

Gallium oxide (Ga_2O_3) stands out due to its broad bandgap, significant breakdown electric field, and unmatched thermal and chemical robustness [1, 2]. These attributes position it as a premier material for high-power electronic devices, UV LEDs, and gas sensors. Moreover, its resilience to radiation damage, bandgap, and thermal stability hint at its potential in advanced scintillators and phosphors. Its luminescence is enhanced through doping with rare-earth ions or other luminescent agents.

Ga_2O_3 encompasses five recognized phases: α, β, γ, δ, and ε [3, 4]. The β-phase garners the most attention, being the most stable and noted for its superb electrical and optical characteristics. Specifically, β-Ga_2O_3 possesses a vast bandgap of 4.9 eV [5] and an impressive breakdown field, approximately 8 MV/cm [6]. Such attributes hint at its capability to surpass silicon carbide (SiC) and gallium nitride (GaN) in power applications.

Notably, β-Ga_2O_3 has displayed commendable scintillation properties [7, 8]. It emerges as a prime candidate for several applications, with its broad bandgap reducing self-absorption, thus augmenting light output. Its thermal fortitude and radiation resistance also make it apt for challenging settings. The enhanced photoelectric absorption and Compton scattering properties of β-Ga_2O_3, attributed to its high atomic number and density, amplify its scintillation efficacy.

For bulk β-Ga_2O_3 crystal growth, a slew of techniques is available, including casting [9], EFG [10], Czochralski [11, 12], Bridgman [13], Pulsed laser deposition [14], and hydrothermal methods [15]. The EFG method is lauded for its prowess in yielding sizable, top-tier β-Ga_2O_3 crystals [16]. However, the final crystal's quality can vary based on temperature, extraction rate, and starting material.

In terms of crafting ceramic Ga_2O_3, processes such as solid-state reactions [17], sol-gel techniques [18], and spark plasma sintering [19] can be harnessed. While these avenues facilitate various shapes and dimensions, they sometimes fail to deliver the desired electronic crystallographic purity.

Adding to the methods above, novel research has spotlighted remarkable outcomes in manufacturing refractory ceramics, especially magnesium fluoride (MgF_2) and yttrium-aluminum-garnet (YAG) ceramics,

using a potent electron beam [20–23]. Such breakthroughs have increased enthusiasm for honing this emergent synthesis technique for refractory substances using an influential electron beam.

Solid-phase synthesis offers significant advantages for producing oxide materials, including high-purity products, simplified purification, and enhanced reaction efficiency. This method is scalable, environmentally friendly, and allows for precise control over stoichiometry, crucial for creating complex oxides with specific properties. Direct combination of metal powders or oxides at high temperatures eliminates the need for solvents, simplifying the synthesis process and reducing environmental impact. Solid-phase synthesis is versatile and capable of producing a wide range of oxides — simple, mixed, and doped — by selecting appropriate precursors and conditions. Its simplicity, scalability, and alignment with green chemistry principles make it an attractive choice for materials science research and industrial applications, ensuring phase-pure oxide materials are essential for catalysis, electronics, and materials science sectors.

Experimental

The synthesis of β-Ga_2O_3 ceramics was meticulously carried out employing a solid-state method, utilizing an initial β-Ga_2O_3 powder that boasted an exceptionally high purity level of 99.999 %. This high-purity powder was methodically pressed into tablets under a substantial pressure of 2 tons, achieving a uniform diameter of 1 cm for each tablet. Figure 1 shows a pressed β-Ga_2O_3 ceramic. Subsequently, these compacted tablets were subjected to a rigorous annealing process within the confines of a high-temperature furnace. The annealing procedure was conducted for an extended duration of 10 hours, at a significantly high temperature of 1400 °C, ensuring the tablets were placed in an alundum crucible to withstand the high-temperature conditions. Following the annealing phase, the ceramic segments were allowed to gradually return to ambient temperature, a crucial step to prevent thermal shock and ensure structural integrity. Once cooled, these segments were then meticulously segmented and subjected to a thorough analysis to assess their structural and compositional attributes. This careful and precise synthesis process is aimed at achieving optimal ceramic properties through controlled high-temperature treatment and subsequent detailed examination of the resulting ceramic segments.

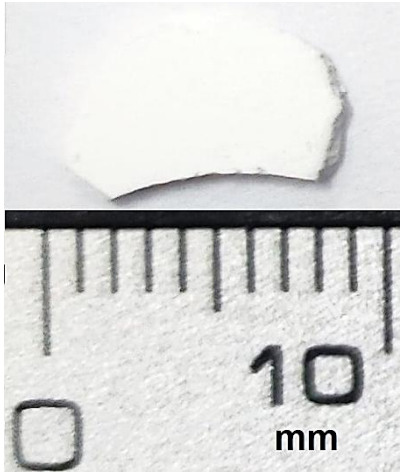

Figure 1. β-Ga_2O_3 ceramics

The surface morphology of the crafted ceramic samples was inspected using a Hitachi TM3030 scanning electron microscope, paired with a BrukerXFlash MIN SVE energy dispersive system (or energy-dispersive spectroscopy, EDS), set at an acceleration voltage of 15 kV. This was integral for the compositional analysis of β-Ga_2O_3. To further comprehend the ceramics' electronic and optical characteristics, excitation and PL emission spectra were logged in a wavelength span between 200 and 800 nm. These measurements were conducted using a CM-2203 spectrofluorimeter at room temperature. For a more comprehensive interpretation, the data from these newly synthesized samples were juxtaposed with equivalent metrics obtained from commercially available unintentional doped (UID) β-Ga_2O_3 crystals with *a* (–201) orientation, sourced from Tamura Corp., Japan.

Results and Discussion

Luminescence spectra of sintered and commercial β-Ga_2O_3 ceramic

Figure 2(*a*, *b*) showcases the photoluminescence spectra of both newly synthesized ceramics and commercial crystals upon excitation at 4.9 eV. Through the application of Gaussian approximation, we were able to delineate three separate components within these spectra. These identified components are characterized by peaks that correspond to blue luminescence, observed at approximately 2.7 eV, and UV luminescence, noted at energy levels of 3.3, 3.4, and 3.8 eV, as illustrated in Figure 2(*a*). A comparative analysis of the spectra from both the synthesized ceramics and the commercial crystals reveals a striking similarity in their overall profiles. However, a discernible variation is observed in the luminescence peak of the synthesized ceramics, which manifests at a slightly diminished energy level, around 3 eV, as indicated in Figure 2(*a*). This downward shift in energy suggests the presence of structural distortions and defects within the crystal lattice of the synthesized ceramics. These structural anomalies are implicated in the modification of electronic properties, thereby rendering them distinct from those observed in commercial crystals. The observed reduction in luminescence intensity can be attributed to two primary factors: a decrease in the levels of oxygen vacancies (VO) and the entrapment of electrons, which are essential for luminescence, by specific defect sites or traps within the crystal structure.

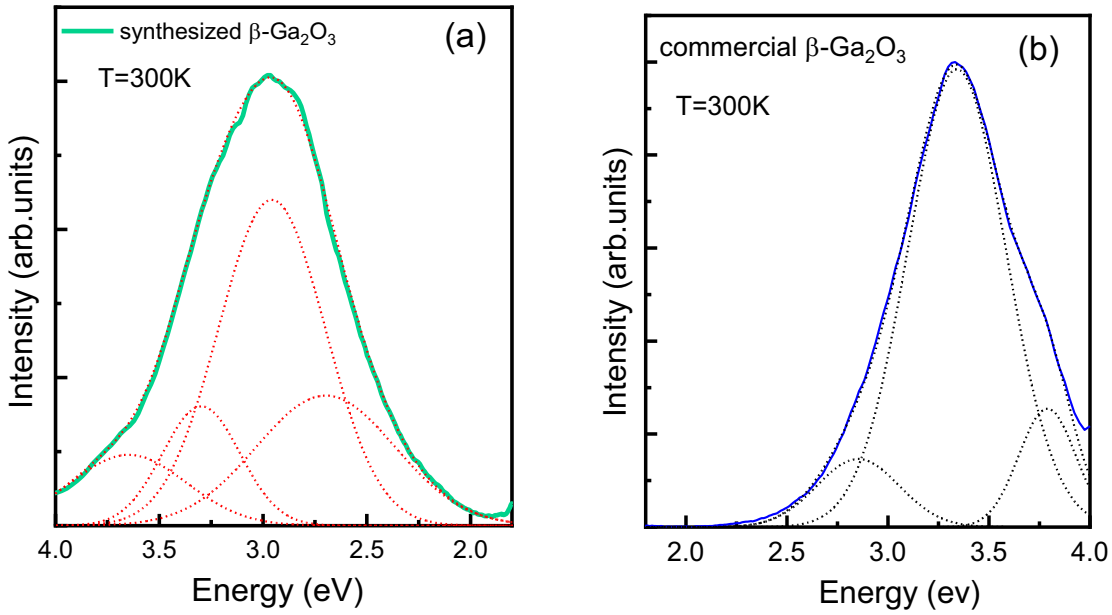

Figure 2. β-Ga_2O_3 ceramics synthesized under a powerful electron beam

Surface morphology and elemental composition

The equipment utilized facilitated the examination of three-dimensional samples with shadow and volume contrast, achieving a resolution as precise as 30 nm. As depicted in Figure 3, the standard SEM images of the crafted β-Ga_2O_3 ceramic surfaces span an area of roughly 0.016 mm^2 (*a*), and the magnified image of the powdered sample is 1000 times its original size (*b*). The derived ceramic exhibits a unified surface structure, signifying the total elimination of powder granules or other defects, culminating in a solidified phase. The primary gallium oxide powder comprises particles ranging from 1 to 15 μm, as shown in Figure 3*b*.

The composition of the synthesized β-Ga_2O_3 ceramic is meticulously aligned with the ideal stoichiometric ratio of oxygen to gallium (O/Ga) of 3/2, a proportion that is critical for achieving desired material properties and is comprehensively documented in Table [24]. This precise compositional alignment mirrors the stoichiometric design principles established in prior studies of β-Ga_2O_3 nanowires [25, 26], underscoring the reproducibility and precision of the synthesis process. Notably, post-annealing treatments have been observed to significantly alter the O/Ga ratio, leading to a notable reduction in gallium content alongside an increase in oxygen levels. This shift towards a higher oxygen content is attributable to the environmental oxygen influx and the subsequent reduction in vacancy concentrations within the crystal lattice, a phenomenon

consistent with behaviors observed in other crystalline oxide systems [27–38]. Such alterations in stoichiometry highlight the dynamic nature of the material's composition, influenced by thermal treatments. Moreover, the initial stoichiometry of the gallium oxide powder used in the synthesis process closely mirrors that of the annealed ceramic samples, indicating a high fidelity in the transference of stoichiometric ratios from the starting materials to the final ceramic product. This observation reinforces the importance of precise starting material composition for achieving the desired characteristics in the annealed ceramics.

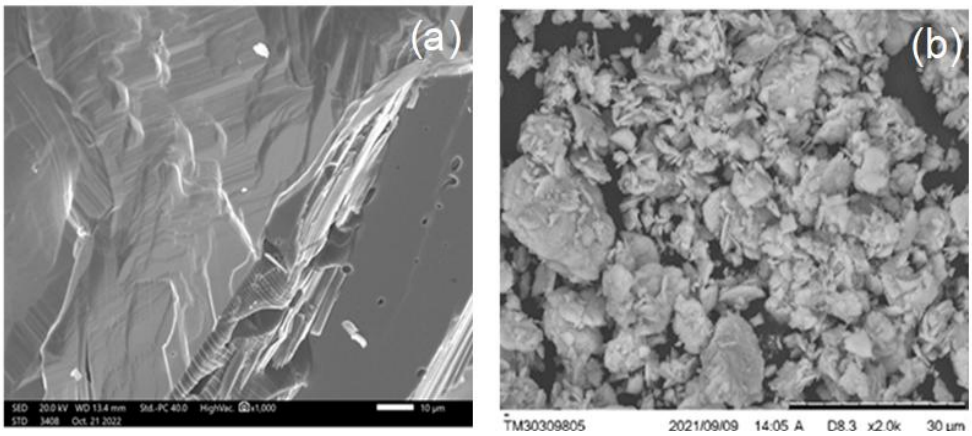

Figure 3. SEM images of synthesized ceramics and the initial Ga_2O_3 powder

T a b l e

Elemental analysis of the powder sample and synthesized β-Ga_2O_3 ceramics (in At. %)

Atom	Synthesized β-Ga_2O_3	Pristine powder β-Ga_2O_3
Ga	33.2	33.4
O	66.8	66.6
O/Ga ratio	2.0	1.99

Conclusions

The spectral, surface morphology and elemental composition of β-Ga_2O_3 ceramics derived from a powdered sample under the influence of a potent solid-state synthesis method have been investigated. These attributes were further compared to the properties of commercial crystals utilized in solar-blind photodetector and scintillator manufacturing. The spectral characteristics of the created ceramics closely mirror those of commercial crystals. When excited in the primary absorption band, the variance in luminescence spectra between the crafted ceramics and commercial crystals can be attributed to lingering distortions and flaws. These irregularities are notably diminished after further annealing. Post-annealing, UV luminescence remains a predominant component of the entire spectrum, but blue luminescence diminishes. This reduction is attributed to the partial annealing of oxygen vacancies and the trapping of luminescent electrons by specific sites. Moreover, the annealing process enhances the Ga/O ratio, giving it an edge over commercial crystals.

The solid-state synthesis method paves the way for the more rapid and cost-efficient creation of β-Ga_2O_3 ceramics, negating the necessity for supplementary equipment or interventions. This method is an effective strategy for generating doped and pure refractory ceramics with elevated melting thresholds.

Acknowledgment

This research has been funded by the Science Committee of the Ministry of Science and Higher Education of the Republic of Kazakhstan (Grant No. AP14972858). Furthermore, J. Purans is grateful to the ERAF project 1.1.1.1/20/A/057. In addition, the research of A.P. and Y.S. was partly supported by COST Action CA20129 "Multiscale Irradiation and Chemistry Driven Processes and Related Technologies" (MultIChem). J.P. and A.P. thank to the Institute of Solid-State Physics, University of Latvia. ISSP UL as the Center of Excellence is supported through the Framework Program for European universities, Union Horizon 2020, H2020-WIDESPREAD-01–2016–2017-TeamingPhase2, under Grant Agreement No. 739508, CAMART2 project.

References

1 Usseinov, A., Koishybayeva, Z., Platonenko, A., Purans, J., & Popov, A.I. (2021). Vacancy defects in Ga_2O_3: First-principles calculations of electronic structure. *Materials*, *14* (23), 7384; https://doi.org/10.3390/ma14237384

2 Suchikova, Y., Lazarenko, A., Kovachov, S., Karipbaev, Z., & Popov, A.I. (2022). Formation of porous Ga_2O_3/GaAs layers for electronic devices. *Proceedings of the 16th International Conference on Advanced Trends in Radioelectronics, Telecommunications and Computer Engineering, TCSET 2022*, 410–413; https://doi.org/10.1109/TCSET55632.2022.9766890

3 Stepanov, S.I., Nikolaev, V.I., Bougrov, V.E., & Romanov, A.E. (2016). Gallium Oxide: Properties and Applications. *A Review, Rev. Adv. Mater. Sci.,* 44, 63–86.

4 Mastro, M.A., Kuramata, A., Calkins, J., Kim, J., Ren, F., & Pearton, S.J. (2017). Perspective — Opportunities and Future Directions for Ga_2O_3, *ECS J. Solid State Sci. Technol.,* 6, 356–359; https://doi.org/10.1149/2.0031707jss

5 Orita, M., Ohta, H., Hirano, M., & Hosono, H. (2000). Deep-Ultraviolet Transparent Conductive β-Ga_2O_3 Thin Films. *Appl. Phys. Lett.,* 77, 4166–4168 https://doi.org/10.1063/1.1330559

6 Varley, J.B. & Schleife, A. (2015). Bethe–Salpeter Calculation of Optical-Absorption Spectra of In_2O_3 and Ga_2O_3. *Semicond. Sci. Technol.*, 30, 024010 https://doi.org/10.1088/0268-1242/30/2/024010

7 Li, W., Zhao, X., Zhi, Y., Zhang, X., Chen, Z., Chu, X., Yang, H., Wu, Z., & Tang, W. (2018). Fabricati on of Cerium-Doped β-Ga_2O_3 Epitaxial Thin Films and Deep Ultraviolet Photodetectors. *Appl. Opt.*, 57, 538; https://doi.org/10.1364/AO.57.000538

8 Luchechko, A., Vasyltsiv, V., Zhydachevskyy, Y., Kushlyk, M., Ubizskii, S, & Suchocki, A. (2020). Luminescence Spectroscopy of Cr^{3+} Ions in Bulk Single Crystalline β-Ga_2O_3. *J. Phys. D. Appl. Phys.*, 53, 354001; https://doi.org/10.1088/1361-6463/ab8c7d

9 Xia, N., Liu, Y., Wu, D., Li, L., Ma, K., Wang, J., Zhang, H., & Yang, D. (2023). β-Ga_2O_3 Bulk Single Crystals Grown by a Casting Method. *J. Alloys Compd.,* 935, 168036; https://doi.org/10.1016/j.jallcom.2022.168036

10 Aida, H., Nishiguchi, K., Takeda, H., Aota, N., Sunakawa, K., & Yaguchi, Y. (2008). Growth of β-Ga_2O_3 Single Crystals by the Edge-Defined, Film Fed Growth Method. Jpn. *J. Appl. Phys*., 47, 8506–8509; https://doi.org/10.1143/JJAP.47.8506

11 Galazka, Z., Uecker, R., Irmscher, K., Albrecht, M., Klimm, D., Pietsch, M., Brützam, M., Bertram, R., Ganschow, S., & Fornari, R. (2010). Growth and Characterization of β-Ga_2O_3 Single Crystals. *Cryst. Res. Technol.,* 45, 1229–1236 https://doi.org/10.1002/crat.201000341

12 Tomm, Y., Reiche, P., Klimm, D., & Fukuda, T. (2000). Czochralski grown Ga_2O_3 crystals. *J. Cryst. Growth 220*, 510–514; https://doi.org/10.1016/S0022-0248(00)00851-4

13 Galazka, Z. (2022). Growth of Bulk β-Ga_2O_3 Single Crystals by the Czochralski Method. *J. Appl. Phys.,* 131, 031103; https://doi.org/10.1063/5.0076962

14 Hoshikawa, K., Ohba, E., Kobayashi, T., Yanagisawa, J., Miyagawa, C., & Nakamura, Y. (2016). Growth of β-Ga_2O_3 Single Crystals Using Vertical Bridgman Method in Ambient Air, *J. Cryst. Growth*, 447, 36–41; https://doi.org/10.1016/j.jcrysgro.2016.04.022

15 Wakabayashi, R., Oshima, T., Hattori, M., Sasaki, K., Masui, T., Kuramata, A., Yamakoshi, S., Yoshimatsu, K., & Ohtomo, A. (2015). Oxygen-Radical-Assisted Pulsed-Laser Deposition of β-Ga_2O_3 and β-$(Al_xGa_{1-x})_2O_3$ Films. *J. Cryst. Growth,* 424, 77–79; https://doi.org/10.1016/j.jcrysgro.2015.05.005

16 Kang, B.K., Mang, S.R., Lim, H.D., Song, K.M., Song, Y.H., Go, D.H., Jung, M.K., Senthil, K., & Yoon, D.H. (2014). Synthesis, Morphology and Optical Properties of Pure and Eu^{3+} Doped β-Ga_2O_3 Hollow Nanostructures by Hydrothermal Method. *Mater. Chem. Phys.,* 147, 178–183; https://doi.org/10.1016/j.matchemphys.2014.04.025

17 Fu, B., Mu, W., Li, Y., Shi, Y., Li, Y., Jia, Z., & Tao, X. (2021). Investigation of the Blue Color Center in β-Ga2O3 Crystals by the EFG Method. *Cryst.Eng.Comm*, 23, 8360–8366. https://doi.org/10.1039/D1CE01078F

18 Ramana, C.V., Roy, S., Zade, V., Battu, A.K., Makeswaran, N., & Shutthanandan, V. (2021). Electronic Structure and Chemical Bonding in Transition-Metal-Mixed Gallium Oxide (Ga_2O_3) Compounds. *J. Phys. Chem. Solids*, 157, 110174. https://doi.org/10.1016/j.jpcs.2021.110174

19 Gopal, R., Goyal, A., Saini, A., Nagar, M., Sharma, N., Gupta, D.K., & Dhayal, V. (2018). Sol-Gel Synthesis of Ga_2O_3 Nanorods and Effect of Precursor Chemistry on Their Structural and Morphological Properties. *Ceram. Int.*, 44, 19099–19105. https://doi.org/10.1016/j.ceramint.2018.07.173

20 Yu, S., Zhang, G., Carloni, D., & Wu, Y. (2020). Fabrication, Microstructure and Optical Properties of Ga_2O_3 Transparent Ceramics. *Ceram. Int.*, 46, 21757–21761; https://doi.org/10.1016/j.ceramint.2020.05.285

21 Alpyssova, G., Lisitsyn, V., Golkovski, M., Mussakhanov, D., Karipbayev, Z., Grechkina, T., Karabekova, D. & Kozlovskiy, A. (2021). Luminescence Efficiency of Cerium-Doped Yttrium Aluminum Garnet Ceramics Formed by Radiation Assisted Synthesis. *Eastern-European J. Enterp. Technol.*, 6, 49–57; https://doi.org/10.15587/1729-4061.2021.246379

22 Karipbayev, Z.T., Lisitsyn, V.M., Mussakhanov, D.A., Alpyssova, G.K., Popov, A.I., Polisadova, E.F., Elsts, E., Akilbekov, A.T., Kukenova, A.B., Kemere, M. et al. (2020). Time-Resolved Luminescence of YAG:Ce and YAGG:Ce Ceramics Prepared by Electron Beam Assisted Synthesis. *Nucl. Instruments Methods Phys. Res. Sect. B Beam Interact. with Mater. Atoms*, 479, 222–228; https://doi.org/10.1016/j.nimb.2020.06.046

23 Lisitsyna, L.A., Popov, A.I., Karipbayev, Z.T., Mussakhanov, D.A., & Feldbach, E. (2022). Luminescence of MgF_2-WO_3 Ceramics Synthesized in the Flux of 1.5 MeV Electron Beam. *Opt. Mater. (Amst)*, *133*, 112999. https://doi.org/10.1016/j.optmat.2022.112999

24 Avilov, M., Fadeev, S., Fernandes, S., Golkovsky, M., Mittig, W., Pellemoine, F., & Schein, M. (2015). A 50-KW Prototype of the High-Power Production Target for the FRIB. *J. Radioanal. Nucl. Chem*., 305, 817–823. https://doi.org/10.1007/s10967-014-3908-1

25 Ahman, J., Svensson, G., & Albertsson, J. (1996). A Reinvestigation of β-Gallium Oxide. *Acta Crystallogr. Sect.* C, 52, 1336–1338. https://doi.org/10.1107/S0108270195016404

26 Cui, H., Sai, Q., Qi, H., Zhao, J., Si, J., & Pan, M. (2019). Analysis on the Electronic Trap of β-Ga_2O_3 Single Crystal. *J. Mater. Sci.,* 54, 12643–12649. https://doi.org/10.1007/s10853-019-03777-1

27 Suchikova, Y., Kovachov, S., Bohdanov, I., Pankratov, V., & Popov, A.I. (2023). Study of the structural and morphological characteristics of the $Cd_xTe_yO_z$ nanocomposite obtained on the surface of the CdS/ZnOheterostructure by the SILAR method. *Appl. Phys. A: Mater. Sci. Process*, 129, 7, 499; https://doi.org/10.1007/s00339-023-06776-x

28 Suchikova, Y., Kovachov, S., Bohdanov, I., Moskina, A., & Popov, A. (2023). Characterization of $Cd_xTe_yO_z$/CdS/ZnO Heterostructures Synthesized by the SILAR Method. *Coatings,* 13 (3), 639. https://doi.org/10.3390/coatings13030639

29 Vambol, S.O., Bohdanov, I.T., Vambol, V.V., Nestorenko, T.P., & Onyschenko, S.V. (2017). Formation of filamentary structures of oxide on the surface of monocrystalline gallium arsenide. *J. Nano-Electron. Phys.,* 9(6), 06016. https://doi.org/10.21272/jnep.9(6).06016

30 Suchikova, Y., Kovachov, S., & Bohdanov, I. (2022). Formation of oxide crystallites on the porous GaAs surface by electrochemical deposition. *Nanomater. Nanotechnol*., 12. https://doi.org/10.1177/18479804221127307

31 Kovachov, S., Bohdanov, I., Karipbayev, Z., Tsebriienko, T., & Popov, A.I. (2022). Layer-by-Layer Synthesis and Analysis of the Phase Composition of $Cd_xTe_yO_z$/CdS/por-ZnO/ZnOHeterostructure. *Proc. 2022 IEEE 3rd KhPI Week on Adv. Technol., KhPI Week 2022.* https://doi.org/10.1109/KhPIWeek57572.2022.9916492

32 Usseinov, A., Platonenko, A., Koishybayeva, Z., Akilbekov, A., Zdorovets, M., & Popov, A.I. (2022). Pair vacancy defects in β-Ga_2O_3 crystal: Ab initio study. *Optical Materials: X,* 16, 100200. https://doi.org/10.1016/j.omx.2022.100200

33 Zachinskis, A., Grechenkov, J., Butanovs, E., Platonenko, A., Piskunov, S., Popov, A.I., Purans, J., & Bocharov, D. (2023). Ir impurities in α-and β-Ga_2O_3 and their detrimental effect on p-type conductivity. *Scientific Reports,* 13(1), 8522. https://doi.org/10.1038/s41598-023-35112-9

34 Usseinov, A., Koishybayeva, Z., Platonenko, A., Akilbekov, A., Purans, J., Pankratov, V., Suchikova, Y., & Popov, A.I. (2021). Ab-Initio Calculations of Oxygen Vacancy in Ga_2O_3 Crystals. *Latv. J. Phys. Tech. Sci.,* 58, 3–10. https://doi.org/10.2478/lpts-2021-0007

35 Klym, H., Karbovnyk, I., Luchechko, A., Kostiv, Y., Pankratova, V., & Popov, A.I. (2021). Evolution of Free Volumes in Polycrystalline $BaGa_2O_4$ Ceramics Doped with Eu^{3+} Ions. *Crystals*, 11, 1515. https://doi.org/10.3390/cryst11121515

36 Luchechko, A., Zhydachevskyy, Y., Ubizskii, S., Kravets, O., Popov, A.I., Rogulis, U., Elsts, E., Bulur, E., & Suchocki, A. (2019). Afterglow, TL and OSL Properties of Mn^{2+}-doped $ZnGa_2O_4$ Phosphor. *Scientific Reports Rep.,* 9, 9544. https://doi.org/10.1038/s41598-019-45869-7

37 Klym, H., Karbovnyk, I., Luchechko, A., Kostiv, Y., & Popov, A.I. (2022). Extended positron trapping defects in the Eu^{3+}-doped $BaGa_2O_4$ ceramics studied by PAL method. *Phys. Status Solidi*, 259, Article 2100485, 10.1002/pssb.202100485

38 Luchechko, A., Zhydachevskyy, Y., Sugak, D., Kravets, O., Martynyuk, N., Popov, A.I., Ubizskii, S., & Suchocki, A. (2019). Luminescence Properties and Decay Kinetics of Mn^{2+} and Eu^{3+} Co-Dopant Ions in $MgGa_2O_4$ Ceramics. Latv. *J. Phys. Tech. Sci.,* 55, 43–51. https://doi.org/10.2478/lpts-2018-0043

А. Бақытқызы, Ж.Т. Карипбаев, Я. Сучикова, А.Б. Усеинов,
Т.Ә. Көкетай, Н.Қ. Мұсабек, А.И. Попов

Қатты дене әдісімен синтезделген β-Ga_2O_3 керамикасын зерттеу

β-Ga_2O_3 керамикалық құрамы мен құрылымы бақыланатын керамикалық материалдарды жасаудың жақсы қалыптасқан әдісі қатты күй әдісі арқылы синтездеу. Процесс материалдың біркелкі таралуы мен ықшамдылығын қамтамасыз ететін галий оксиді (Ga_2O_3) ұнтағын біртұтас пішінге престеу арқылы басталады. Содан кейін бұл престелген пішін 1400 °C температурада 10 сағат бойы жасытуға ұшырайды, бұл тұрақты және кристалды β-Ga_2O_3 фазасының түзілуін жеңілдететін маңызды қадам. Синтезделген β-Ga_2O_3 керамикасының элементтік құрамын зерттеу үшін энергетикалық дисперсиялық рентгендік талдау (EDS) қолданылды. Талдау материалдың керамиканың тазалығы мен консистенциясын қамтамасыз ете отырып, оттегі мен галлийдің (O/Ga) мінсіз стехиометриялық арақатынасына 3:2 сәйкес келетінін растады. β-Ga_2O_3 керамикасының оптикалық қасиеттері мұқият зерттелді. Беттік морфологияны талдау және элементтік құрамды өлшеу 200-ден 800 нм-ге дейінгі дәйекті толқын ұзындығында фотолюминесценцияның қозуы мен өткізу спектрлерін тіркеумен толықтырылды. Бұл спектрлер материалдың электрондық және оптикалық қасиеттері туралы құнды түсініктер береді. Синтезделген β-Ga_2O_3 керамикалық және коммерциялық β-Ga_2O_3 кристалдары көк (~2,7 эВ) және ультракүлгін (3,3, 3,4, 3,8 эВ) спектрлік диапазондарда фотолюминесценцияның айқын шыңдарын көрсетті.

Кілт сөздер: синтез, β-Ga_2O_3 керамика, фотолюминесценция, күйдіру, стехиометриялық қатынас, морфология, элементтік құрам, нүктелік ақаулар

А. Бакыткызы, Ж.Т. Карипбаев, Я. Сучикова, А.Б. Усеинов,
Т.А. Кокетай, Н.К. Мусабек, А.И. Попов

Исследование керамики β-Ga_2O_3, синтезированной твердотельным методом

Керамика β-Ga_2O_3 была синтезирована с использованием твердотельного метода, хорошо зарекомендовавшего себя в создании керамических материалов с контролируемым составом и структурой. Процесс начался с прессования порошка оксида галлия (Ga_2O_3) в единую форму, что обеспечило равномерное распределение и компактность материала. Затем прессованная форма была подвергнута отжигу при 1400 C в течение 10 часов, что является важным шагом, способствующим образованию стабильной и кристаллической фазы β-Ga_2O_3. Для исследования элементного состава синтезированной керамики β-Ga_2O_3 был использован энергодисперсионный рентгеновский анализ (EDS), который подтвердил, что материал близок к идеальному стехиометрическому соотношению кислорода к галлию (O/Ga) в 3:2, что обеспечивает чистоту и однородность керамики. Оптические свойства керамики β-Ga_2O_3 были тщательно изучены. Анализ морфологии поверхности и измерения элементного состава были дополнены регистрацией спектров возбуждения и пропускания фотолюминесценции на последовательных длинах волн в диапазоне от 200 до 800 нм. Эти спектры предоставили ценную информацию об электронных и оптических свойствах материала. Как синтезированная керамика β-Ga_2O_3, так и коммерческие кристаллы β-Ga_2O_3 показали отчетливые пики фотолюминесценции в синем (~2,7 эВ) и ультрафиолетовом (3,3, 3,4, 3,8 эВ) спектральных диапазонах.

Ключевые слова: синтез, керамика β-Ga_2O_3, фотолюминесценция, отжиг, стехиометрические соотношения, морфология, элементный состав, точечные дефекты

Information about the authors

Bakytkyzy, Aizat — PhD student, Institute of Physical and Technical Sciences, L.N. Gumilyov Eurasian National University, Astana 010008, Kazakhstan; e-mail: kukenova_ab_1@enu.kz; ORCID ID: https://orcid.org/0000-0002-6304-8365

Karipbayev, Zhakyp (*corresponding author*) — PhD, Institute of Physical and Technical Sciences, L.N. Gumilyov Eurasian National University, Astana 010008, Kazakhstan; e-mail: karipbayev_zht_1@enu.kz; ORCID ID: https://orcid.org/0000-0003-4066-1826

Suchikova, Yana — Doctor of physical and mathematical sciences, Professor of the Department of Physics and Methods of Teaching Physics, Berdyansk State Pedagogical University, 71100 Berdyansk, Ukraine; e-mail: yanasuchikova@gmail.com; ORCID ID: https://orcid.org/0000-0003-4537-966X

Usseinov, Abay — PhD, Institute of Physical and Technical Sciences, L.N. Gumilyov Eurasian National University, Astana 010008, Kazakhstan; e-mail: usseinov_ab@enu.kz; ORCID ID: https://orcid.org/0000-0002-4066-8422

Koketai, Temirgali — Doctor of physical and mathematical sciences, Professor, Department of Physics and Nanotechnology, Karaganda Buketov University, Karaganda, Kazakhstan; e-mail: katkargu@mail.ru; https://orcid.org/0000-0003-2575-7280

Mussabek, Nurassyl — Master of Science, Institute of Technical Physics and Ecological Problems, Karaganda Buketov University, Karaganda, Kazakhstan; e-mail: nyri-t-ara@mail.ru; ORCID ID: //https://orcid.org/0009-0002-4319-3319

Popov, Anatoli — Doctor of physical and mathematical sciences, Professor, Institute of Solid-State Physics, University of Latvia, 8 Kengaraga Str., Lv-1063 Riga, Latvia; e-mail: popov@latnet.lv; ORCID ID: https://orcid.org/0000-0003-2795-9361

Article
https://doi.org/10.31489/2025PH1/20-28
UDC 538.9+544.65

Received: 09.09.2024
Accepted: 12.09.2024

A. Serikkazyyeva[1,2], M. Yegamkulov[1,3], Y. Raiymbekov[1,3], B. Uzakbaiuly[3,4], Z. Bakenov[1,2,3], A. Mukanova[1,3*]

[1]*National Laboratory Astana, Nazarbayev University, Astana, Kazakhstan;*
[2]*Department of Chemical and Materials Engineering, School of Engineering and Digital Sciences, Nazarbayev University, Astana, Kazakhstan;*
[3]*Institute of Batteries LLC, Astana, Kazakhstan;*
[4]*Fraunhofer IKTS, Forchheim, Germany*
*(*Corresponding author's e-mail: aliya.mukanova@nu.edu.kz)*

Morphological Investigation of Li Thin Film Deposited on LiPON Solid Electrolyte and the Influence of Interlayers on It

All-solid-state thin-film lithium metal batteries (ASSTFBs) hold great promise for next-generation energy storage due to their long cycle life, stability across a wide temperature range, and low self-discharge, making them ideal for applications in wearable devices, medical implants, and IoT systems. Achieving uniform lithium (Li) deposition on lithium phosphorus oxynitride (LiPON) solid electrolytes is a critical challenge for advancing ASSTFBs. This study evaluates the role of various interlayers in improving film uniformity and adhesion and compares thermal evaporation (TE) and magnetron sputtering (MS) methods for depositing Li films on LiPON. Initial TE trials revealed discontinuous, droplet-like Li particles with poor interconnection and adhesion on the LiPON surface. To address these issues, metallic interlayers (Sn, Al, Ag, Au, Pt) and metal oxides (ZnO, Al_2O_3) were explored. Among these, Pt demonstrated the most promising results, forming a lithophilic alloy that improved particle connectivity and interface uniformity. MS produced more consistent Li films compared to TE, attributed to its better-controlled deposition rate and reduced thermal effects. However, MS requires precautions due to Li's reactivity and potential system contamination. The findings emphasize the importance of interlayer selection and deposition method optimization in achieving dense, uniform Li films. This work contributes to the development of high-performance, reliable microbatteries for advanced energy storage applications. Future studies will focus on refining deposition parameters and evaluating electrochemical performance to further enhance battery efficiency and stability.

Keywords: lithium, LiPON, thin film, solid electrolyte, thermal evaporation, magnetron sputtering, all-solid-state lithium metal microbattery

Introduction

Lithium-ion batteries (LiBs) have become a leading energy storage technology, widely utilized in electric vehicles, power tools, and portable devices due to their high energy and power density. As the demand for microscale devices, such as medical apparatus, grows, advancements in LiBs have extended to energy storage microsystems using thin-film technology. Thin-film electrodes enable the reduction of inactive components, ensuring sufficient electrical conductivity, improved cycling stability, and enhanced power density, making them ideal for miniaturized applications [1–3].

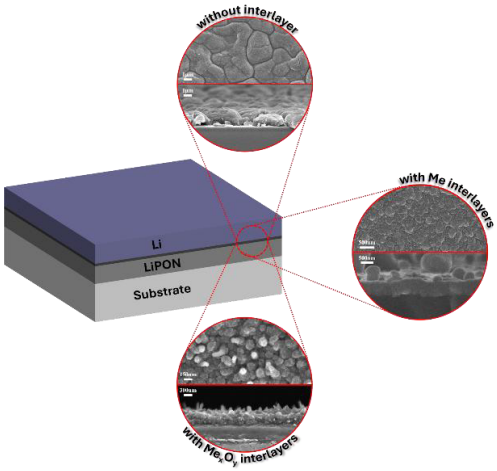

Rechargeable lithium-metal batteries (LMBs), which use metallic lithium (Li) as an anode or operate as anode-free systems, have emerged as promising alternatives to conventional LiBs with graphite anodes. The advantages of LMBs include a high theoretical capacity (3860 mAh g^{-1}), low negative potential (–3.04 V), low density (0.59 g cm^{-3}), and high electrical conductivity, along with the potential to eliminate inactive components in the negative electrode [4–6]. However, challenges such as dendritic Li growth, safety risks due to short circuits, and the formation of dead Li layers resulting from side reactions have hindered their practical application.

The cycling performance of Li-metal anodes is highly dependent on the electrolyte. Solid electrolytes, particularly lithium phosphorus oxynitride (LiPON), offer advantages such as high ionic conductivity, chem-

ical stability, and compatibility with thin-film systems. These properties enable the development of safer, longer-lasting, and more compact Li-ion microbatteries [7]. However, challenges persist at the Li-LiPON interface, including poor adhesion, high interfacial resistance, and the formation of dendrites, all of which need to be addressed to unlock the potential of LMBs for practical applications [8, 9].

Thermal evaporation (TE) is a common method for depositing Li thin films due to its simplicity and applicability in various industries. This process involves heating a source material under high vacuum until it sublimes, condensing onto a substrate as a thin film [10]. Despite its advantages, TE often results in nonuniform Li films with low surface coverage, posing challenges for achieving consistent morphology and adhesion.

A critical issue limiting the performance of solid-state LMBs is the lithiophobic nature of solid electrolytes like LiPON. This results in poor wettability, space charge layer formation, interfacial resistance, and dendritic growth. Enhancing lithiophilicity is essential for improving Li deposition and overall battery performance. Approaches to achieving better lithiophilicity include modifying surface energy, introducing alloying additives (e.g., Sn, In, Mg), or applying coatings like Al_2O_3, ZnO, Au, or Al, which improve physical contact and chemical compatibility between Li and the electrolyte [11–20].

In this study, we aimed to achieve uniform and consistent Li deposition on LiPON solid electrolytes using TE. To address the limitations of TE, we explored various interlayers, including metals (Ag, Au, Al, Sn, Pt) and metal oxides (Al2O3, ZnO), to improve lithiophilicity and adhesion. Additionally, magnetron sputtering (MS) was investigated as an alternative technique, which demonstrated superior uniformity and contact at the Li-LiPON interface without requiring interlayers.

Experimental

The deposition of Li was performed mainly by TE, utilizing a resistive heating technique involving high electric current and low voltage, in a COVAP Physical Vapor Deposition (PVD) chamber (Angstrom Engineering), maintaining a high vacuum of around 10^{-6} mbar, integrated with a glove box filled with argon (Ar) with H_2O concentrations below 0.1 ppm and O_2 levels below 0.1 ppm.

For the process of depositing a thin layer of lithium onto a silicon wafer, Li metal chips (99.9 %, MTI Corp.) were placed in a tantalum evaporation boat. For evaporation of metals, pure pieces of Ag, Au, Sn (Angstrom Engineering, 99.9 %) were placed on Al_2O_3 coated tungsten boat and Al pieces on graphite coated boat (Angstrom Engineering). The system, with a maximum power output of 2000 W, allocated approximately 12 % of this power for the evaporation of the Li metal, and 25–30 % for Al, Ag, Au, Sn metals. The deposition rate for all metals was approximately 1 Å s^{-1}.

The thickness of film was monitored using quartz crystal microbalance (QCM) sensors operating at 6 MHz frequencies and controlled by an SQC-310 controller (Inficon). This setup allowed for adjustments to deposition rate, additional heating settings, and the final film thickness. The substrate, mounted on a holder, rotated at a speed of 50 rpm, and a shutter was employed to protect the substrate until the desired deposition rate of 1Å s^{-1} was achieved. Once the required rate was reached, the shutter opened giving a start to the deposition. For all samples, the optimized thickness of 10 nm was chosen due to the quicker lithium diffusion [21].

To deposit oxides, targets of Al_2O_3, ZnO (Kurt J. Lesker 99.99 %), Pt (Angstrom Engineering, 99.99 %) and Li (home-made) were used in a magnetron sputtering (MS) system (Nexdep, Angstrom Engineering). To prepare a Li target, 10–15 pieces of Li chips were melted in a 2-inch copper mold at 350 °C for 30–40 minutes, after which it was left to cool and harden. The whole process was carried out inside a glove box. The sputtering chamber was evacuated down to 2×10^{-6} mTorr by a turbo vacuum pump. Argon gas was introduced into the chamber, and pressure was balanced to 5 mTorr. The target was cleaned by a 10 min presputtering before the substrate shutter was opened to eliminate oxide layer and other contaminations on the target surface. The lithium depositing rate was calculated to be 0.39 Å s^{-1} by QCM sensor at a power of 1.78 W cm^{-2}.

To analyze the sample morphology, the ZEISS Crossbeam 540 model Scanning Electron Microscope (SEM) was used. The SEM images were acquired with an accelerating voltage of 3 kV and a variable working distance spanning from 3.5 to 4 mm.

Results and Discussion

Initially, passing all the optimization steps of thin-film electrodes and coming to the point of their integration into microcells, unexpected topological challenges with the formed Li film on LiPON solid were

faced and it was decided to explore this phenomenon deeper. In Figure 1 *a*, *b*, the SEM images of the bare Li film thermally evaporated on the surface of LiPON can be seen, which demonstrates non-uniformly distributed, island-shaped lithium droplet-like particles on the electrolyte surface, lacking interconnection, potentially resulting in poor adhesion. The observed configuration may give rise to the formation of space charge layers between lithium and the electrolyte [22, 23]. This spatially discontinuous distribution of Li particles elevates concerns about the overall coherence and effectiveness of the electrode-electrolyte interface, emphasizing the importance of addressing adhesion issues for enhanced electrochemical performance in the studied microsystem.

The poor deposition of evaporated lithium onto LiPON can be attributed to its compositional complexity, morphology and the deposition parameters. LiPON surfaces may have different chemical compositions and surface energies, which can affect the adhesion and nucleation of evaporated lithium atoms. The presence of phosphorus, oxygen, and nitrogen species on the LiPON surface may interact unfavorably with lithium atoms, leading to non-uniform deposition. The surface morphology of LiPON may also not provide suitable sites for the nucleation and growth of lithium atoms. Irregularities or roughness on the LiPON surface can hinder the formation of a continuous and uniform lithium film. However, from all the SEM images (Fig. 1), it can be seen that the sputtered LiPON is well deposited and uniform. Next, the electrochemical properties, such as ion conductivity and stability, may not be compatible with the deposition of evaporated Li. Chemical reactions or diffusion limitations within the LiPON material may inhibit the deposition process. Finally, the temperature and pressure conditions during the deposition process can significantly influence the behavior of evaporated Li and its interaction with LiPON [24]. Here, we should mention that the conditions were optimized to achieve the lowest possible deposition rate since at higher one, the morphology was even worse.

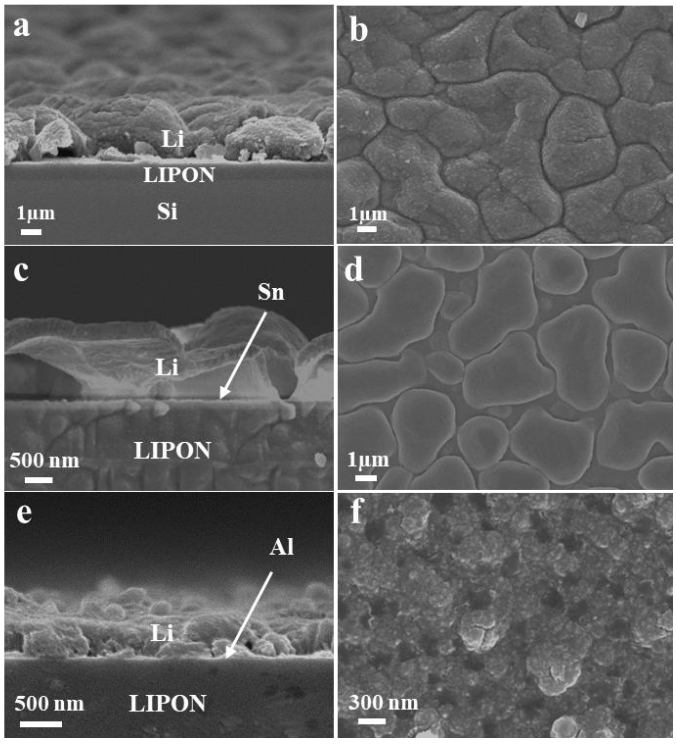

a, b — Li-LiPON; *c, d* — Li-Sn-LiPON; *e, f* — Li-Al-LiPON

Figure 1. The cross-sectional and top-view SEM images of the samples

With the goal to improve the uniformity of the evaporated Li onto LiPON interface, we explored the application of various metals, including Sn, Al, Ag, Pt, and Au, as well as some metal oxides like Al_2O_3 and ZnO as intermediary layers between Li and the LiPON solid electrolyte.

Firstly, as an interlayer, Sn metal was investigated due to the better adhesion, faster Li ions diffusion as well as immediate alloying reaction with Li, which is supposed to result in the dense Li-Sn interlayer formation [25–27]. A 10 nm thick Sn film was evaporated on the LiPON substrate. The obtained re-

sults (Fig. 1 *c*, *d*) exhibited a lack of uniformity, showing the surface with an island-shaped structure that lacked proper interconnection between particles, as illustrated in Figure 1 *d*. Furthermore, a detailed examination of the cross-sectional image (Fig. 1 *c*) revealed the presence of noticeable voids within the particles. These observations suggest the existing challenges in achieving a homogeneous structure and effective interparticle contact, emphasizing the complexity involved in optimizing the electrode-electrolyte interface for improved performance in Li-Sn-LiPON system.

Similarly, hoping to get ionically conductive Li-Al alloy that serves as an interfacial layer when Al is added [28], Al was evaporated on LiPON. The resulting structure is prominently illustrated in Figure 1 *e, f*. Notably, the Li-Al-LiPON samples exhibit a denser configuration in contrast to those with above-mentioned Sn. A discernible improvement is observed in the connectivity of particles, indicating a more cohesive arrangement without the presence of large clusters. The enhanced connectivity of particles is indicative of a potentially improved electrode-electrolyte interface. It may promote efficient ion transport and minimize impedance at the interface. However, unevenly distributed bumps and cracks are still visible on the surface of the thin lithium film.

The subsequent metal, Ag, has the lowest electrical contact resistance and the maximum electrical conductivity when compared to other metals. This can prevent the production of lithium dendrites and encourages more uniform plating of lithium ions [29]. From Figure 2 *a, b*, the examination of the images reveals a surface characterized by enhanced smoothness and a more uniform distribution of the deposited layer. Additionally, there is an observable reduction in the size of the particles compared to previous instances with other metals. The distinct improvements in surface smoothness and homogeneity, coupled with the reduction in particle size, highlight the favorable impact of Ag as an intermediary layer in the Li and LiPON interface. These characteristics are indicative of a more controlled and refined deposition process, underscoring the potential of silver to contribute to the development of a highly uniform and well-structured electrode-electrolyte interface.

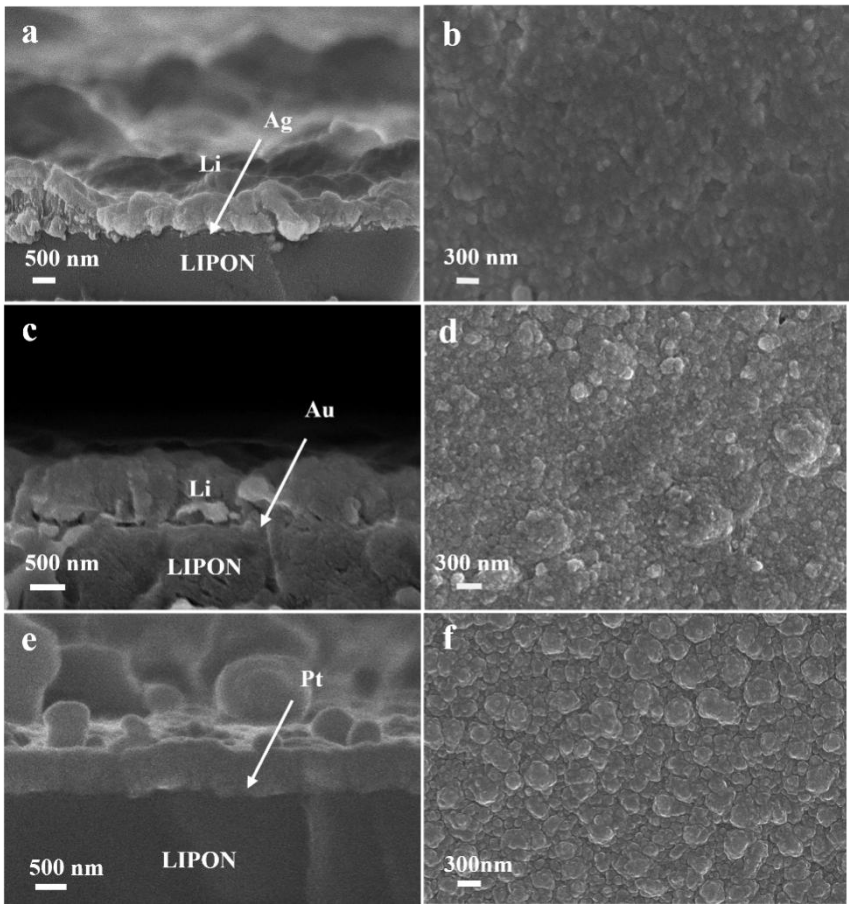

Figure 2. The cross-sectional and top-view SEM images
of the samples with Ag (*a, b*), Au (*c, d*), Pt (*e, f*) interlayers

Next, the Au was tested, as it has been already reported for maintaining a stable Li deposition [30]. The results obtained from this investigation (Fig. 2 *c, d*) indicate that the application of gold as an intermediary layer also yielded notably superior characteristics. A discernible enhancement in the wettability of Li was observed, accompanied by a more even and flattened surface in comparison to preceding samples. The superior characteristics exhibited by the Au-deposited samples suggest a positive influence on the overall homogeneity of the Li layer. The improved wettability is particularly noteworthy, as it underscores the effectiveness of gold as an intermediary material in facilitating a more uniform and well-adhered Li film evaporated on the LiPON solid electrolyte.

Consequently, Pt was incorporated as the interlayer to assess its potential impact (Fig. 2 *e, f*) on morphology of evaporated Li film. The desired uniformity in the deposition process was achieved by this metal since it might alloy with Li metal in electrochemical systems [31]. As it can be seen from the cross-sectional image (Fig. 2 *e*), the interface of the Li on LiPON is more improved, particles are well connected and form dense thin film with the uniform thickness. The additional particles can be noted on the top surface of Li which might be attributed to non-uniformly deposited Li on top of alloy layer.

Pt and Li have Gibbs free energies that are less than zero, which means that they could combine to produce $LiPt_x$ alloy. The creation of a three-dimensional framework also facilitates the plating and stripping of Li ions and keeps the volume of Li metal from expansion. By forming a $LiPt_x$ alloy, the 10 nm thin Pt the surface of electrolyte changes from lithiophobic to lithiophilic. In literature, for the garnet surface, the $LiPt_x$ alloy layer increases the wettability of the Li–electrolyte contact, favorable Li transport across the interface [32].

Further, the impact of incorporating an inorganic metal oxide interlayer was systematically investigated. The ZnO layer can effectively lower the interface impedance and enhance solid electrolyte compatibility with metallic Li [33]. To achieve this, a 10 nm thick ZnO layer was meticulously deposited through RF MS, strategically positioned between the lithium phosphorus oxynitride (LIPON) and lithium (Li) layers. The outcome of this investigation (Fig. 3 *a, b*) revealed notable enhancements, particularly in the uniformity of Li deposition, accompanied by a discernible increase in particle density.

The addition of the ZnO layer yielded a more homogeneous deposition of lithium, evident in the observed uniformity across the substrate. The resultant particles exhibited a denser configuration, which is a favorable characteristic for enhancing the overall performance of the battery system. However, a closer examination of cross-sectional images unveiled the formation of knots on the surface. This observation suggests the possibility of side reactions occurring during the deposition process, impacting the uniformity of the film.

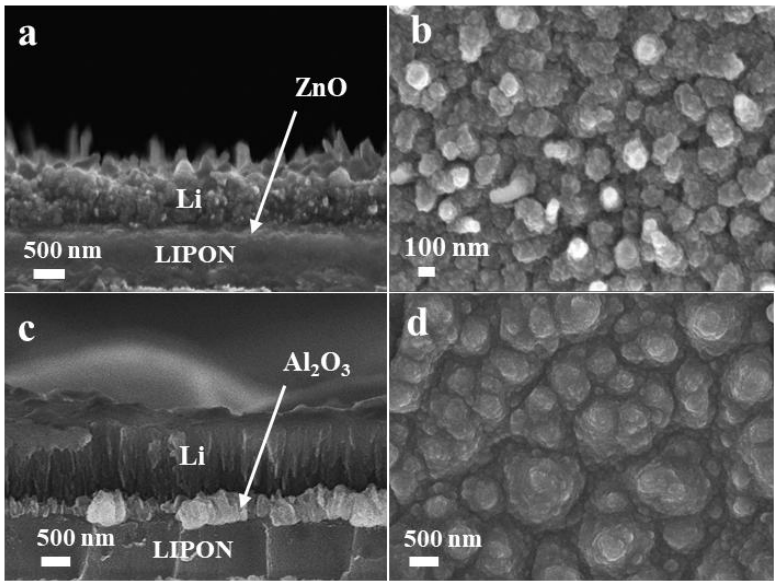

Figure 3. The cross-sectional and top-view SEM images of the samples with ZnO (*a, b*), Al_2O_3 (*c, d*) interlayers

Another metal oxide implemented as an interface layer was Al_2O_3, which was previously applied with ionic liquid electrolyte and was reported for better stability and lithiophilicity [34]. As a result of the investigation (Fig. 3 *c, d*), the homogeneous deposition of Li was achieved. As it can be seen from the SEM image, Li on Al-LiPON formed the dense structure with the interconnected particles. This can be explained by the good adhesive properties and chemical inactivity of alumina towards different materials, including Li. Some roughness on the Li thin film surface can be observed; however, it is within acceptable limits.

The advantage of TE compared to MS is its high deposition rate. But as our above-mentioned experimental results have shown, the evaporated Li films are not always uniform, which are very crucial for mcrobattery. To compare TE and MS, the Li thin films were sputtered on LiPON surface using MS. Figure 4 *a, b* shows the top and cross-sectional SEM image of the obtained Li thin film. As can be seen, the surface of the resulting film is uniform as usual for other MS materials, which is an advantage of the magnetron.

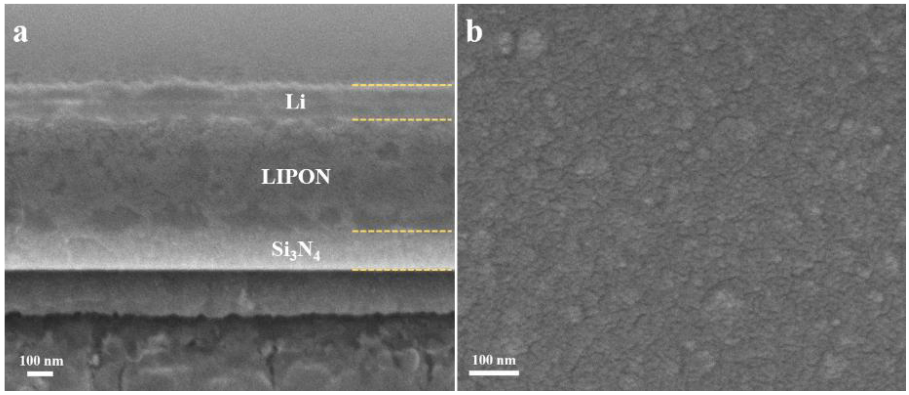

Figure 4. The cross-sectional (*a*) and top-view (*b*) SEM images of Li-LiPON sample

This can be probably explained by the better-controlled deposition rate of MS. The rate fluctuates extensively during TE. Even though the thickness of Li is measured after stabilization, the evaporation rate after several tens of minutes slowly decreases from 1–1.5 Å s^{-1} to 0.45 Å s^{-1} [35]. Among the other possible reasons of uniform morphology by MS are the better directionality of deposition which is controlled using magnetic fields, ensuring that Li atoms or ions are deposited evenly onto the substrate, and reduced heating effects on substrate, minimizing thermal effects and promoting uniformity.

Magnetron sputtering systems are more commonly used equipment, but precautions must be taken when sputtering Li due to its tendency to form deposits within the work chamber and react with other system components such as targets and walls. This can degrade system performance and lifespan, causing electrical shorts, increased electrical resistance, and potential plasma instabilities due to Li's unique properties, including high reactivity and low ionization potential. In contrast, evaporation of Li poses a lower risk of damage because the process occurs in a deep vacuum with negligibly low gas impurities, minimizing the potential for reactions with Li.

The results obtained offer a comprehensive investigation into the challenges faced during the integration of thin-film electrodes into microcells, particularly concerning the deposition of Li onto LiPON solid electrolytes using TE. This study highlights the intricate influence of interlayers on the lithium deposition process, stressing the need for a thorough understanding of both the beneficial and potentially adverse effects of various materials. Addressing the non-uniform distribution of Li particles on the LiPON surface can be achieved by switching to the MS technique with proper handling and equipment maintenance.

Conclusion

This study highlights key challenges and solutions for lithium (Li) deposition on LiPON solid electrolytes in all-solid-state thin-film lithium microbatteries. Initial thermal evaporation (TE) of Li produced discontinuous, droplet-like particles on LiPON, resulting in poor adhesion. Interlayers of Sn, Al, Ag, Au, and Pt were evaluated to improve uniformity, with Pt achieving the best results due to the formation of a lithophilic alloy that enhanced particle connectivity and adhesion. Metal oxides like ZnO and Al_2O_3 also improved Li film density, though minor surface irregularities remained.

Magnetron sputtering (MS) provided a more consistent Li film than TE, benefiting from controlled deposition and reduced thermal effects. These findings underline the importance of selecting interlayers and

deposition methods carefully to optimize Li films for microbatteries. Further refinement of these parameters will support the development of high-performance, stable energy storage for applications from portable electronics to electric vehicles.

Funding

This research was supported by the research grant № AP19578472 (2023-2025), AP19680567 (2023-2025), and № BR21882402 (2023-2025) and a research grant from the Ministry of Science and Higher Education of the Republic of Kazakhstan.

Acknowledgments

Authors extend their sincere gratitude to Core Facility at Nazarbayev University for their invaluable assistance with the data characterization in this study.

А. Серікқазыева, М. Егамқұлов, Е. Райымбеков,
Б. Ұзақбайұлы, Ж. Бакенов, А. Муканова

LiPON қатты электролитіне тұндырылған жұқа литий пленкасын және оған аралық қабаттардың әсерін морфологиялық зерттеу

Толық қатты күйдегі жұқа пленкалы литий аккумуляторлары (ТҚЖПЛА) ұзақ қызмет ету мерзіміне, әртүрлі температурадағы тұрақтылыққа және өзін-өзі разрядтаудың төмен деңгейіне байланысты энергия сақтау құрылғыларының келесі буыны үшін үлкен әлеуетке ие. Бұл оларды киюге болатын құрылғыларда, имплантацияланатын аспаптарда және интернет заттары жүйелерінде қолдануға өте ыңғайлы етеді. Алайда, металл литий мен LiPON сияқты қатты электролит арасындағы тұрақты интерфейсті құру үлкен қиындық тудырады. Себебі LiPON-ның төмен литийфильділігі қарсылықты арттырып, иондардың тиімді тасымалдануын тежейді. Осы зерттеу барысында литийдің біркелкі түзілуін жақсарту мақсатында LiPON бетінің литийфильділігін оксидтік және металл аралық қабаттар арқылы арттыру қарастырылды. Толық СЭМ-талдау нәтижесінде Pt және Au металдары литийдің біркелкі және жақсы байланысуын қамтамасыз ететін үйлесімділіктің жоғары екенін көрсетті, ал ZnO және Al_2O_3 оксидтері тұндыру консистенциясын жақсартты. Бұл нәтижелер ТҚЖПЛА жүйелерінде фаза аралық кедергілерді төмендету және литийдің біркелкі түзілуін жақсарту мүмкіндігін көрсетіп, қатты денелі микробатареяларды кеңейтілген қолдануға жол ашады.

Кілт сөздер: литий, LiPON, жұқа пленка, қатты электролит, термиялық булану, магнетронды бүрку, толық қатты күйдегі жұқа пленкалы литий аккумуляторлары (ТҚЖПЛА).

А. Серикказыева, М. Егамкулов, Е. Райымбеков,
Б. Узакбайулы, Ж. Бакенов, А. Муканова

Морфологическое исследование тонкой пленки лития, осажденной на твердый электролит LiPON, и влияние промежуточных слоев

Полностью твердотельные тонкопленочные литиевые аккумуляторы (ПТТЛА) обладают большим потенциалом для следующего поколения накопителей энергии благодаря длительному сроку службы, стабильности при различных температурах и низкому уровню саморазряда, что делает их идеальными для применения в носимых устройствах, имплантируемых приборах и системах интернет-вещей. Однако создание стабильного интерфейса между металлическим литием и твердым электролитом, таким как фосфороксинитрид лития (LiPON), представляет значительные трудности, связанные с его низкой литиефильностью. Это увеличивает сопротивление и препятствует эффективному переносу ионов. В данном исследовании изучено улучшение литиефильности поверхности LiPON с помощью оксидных и металлических промежуточных слоев, направленное на повышение равномерности осаждения лития. Детальный СЭМ-анализ показал, что металлы, такие как Pt и Au, обладают высокой совместимостью, способствуя более равномерному и прочному осаждению лития, в то время как ZnO и Al_2O_3 обеспечивают улучшенную консистентность осаждения. Полученные результаты демонстрируют возможность снижения межфазного сопротивления и повышения равномерности осаждения лития в ПТТЛА, что открывает путь для расширенного применения твердотельных микробатарей.

Ключевые слова: литий, фосфороксинитрид лития (LiPON), тонкая пленка, твердый электролит, термическое испарение, магнетронное распыление, полностью твердотельные тонкопленочные литиевые аккумуляторы (ПТТЛА).

References

1 Kim, T., Song, W., Son, D., Ono, L.K., & Qi, Y. (2019). Lithium-ion batteries: outlook on present, future, and hybridized technologies. *Journal of Materials Chemistry A*, *7*(7), 2942–2964.

2 Armand, M., Axmann, P., Bresser, D., Copley, M., Edström, K., Ekberg, C., Guyomard, D., Lestriez, B., Novák, P., Petranikova, M., Porcher, W., Trabesinger, S., Wohlfahrt-Mehrens, M., & Zhang, H. (2020). Lithium-ion batteries — Current state of the art and anticipated developments. *Journal of Power Sources*, *479*, 228708.

3 Masias, A., Marcicki, J., & Paxton, W.A. (2021). Opportunities and challenges of lithium ion batteries in automotive applications. *ACS Energy Letters*, *6*(2), 621–630.

4 Wang, H., Yu, Z., Kong, X., Kim, S.C., Boyle, D.T., Qin, J., Bao, Z., & Cui, Y. (2022). Liquid electrolyte: The nexus of practical lithium metal batteries. *Joule*, *6*(3), 588–616.

5 Kim, S., Kim, J., Miara, L., Wang, Y., Jung, S., Park, S.Y., Song, Z., Kim, H., Badding, M., Chang, J., Roev, V., Yoon, G., Kim, R., Kim, J., Yoon, K., Im, D., & Kang, K. (2022). High-energy and durable lithium metal batteries using garnet-type solid electrolytes with tailored lithium-metal compatibility. *Nature Communications*, *13*(1), 1883.

6 Kim, S., Park, G., Lee, S.J., Seo, S., Ryu, K., Kim, C.H., & Choi, J.W. (2022). Lithium-Metal Batteries: From fundamental research to industrialization. *Advanced Materials*, *35*(43), 2206625.

7 Uzakbaiuly, B., Mukanova, A., Kurmanbayeva, I., & Bakenov, Z. (2019). Optimization of deposition parameters for thin film lithium phosphorus oxynitride (LIPON). *Eurasian Journal of Physics and Functional Materials*, *3*(2), 174–182.

8 Zhang, X., Yang, Y., & Zhou, Z. (2020). Towards practical lithium-metal anodes. *Chemical Society Reviews*, *49*(10), 3040–3071.

9 Zhang, R., Li, N., Cheng, X., Yin, Y., Zhang, Q., & Guo, Y. (2017). Advanced Micro/Nanostructures for lithium metal anodes. *Advanced Science*, *4*(3), 1600445.

10 Adhitama, E., Brandao, F.D., Dienwiebel, I., Bela, M. M., Javed, A., Haneke, L., Stan, M.C., Winter, M., Gomez-Martin, A., & Placke, T. (2022). Pre-Lithiation of silicon anodes by thermal evaporation of lithium for boosting the energy density of lithium ion cells. *Advanced Functional Materials*, *32*(22), 2201455.

11 Li, C., Zhang, X., Zhu, Y., Zhang, Y., Xin, S., Wan, L., & Guo, Y. (2022). Modulating the lithiophilicity at electrode/electrolyte interface for high-energy Li-metal batteries. *Energy Materials*, *1*(2), 100017.

12 Wang, J., Wang, H., Xie, J., Yang, A., Pei, A., Wu, C., Shi, F., Liu, Y., Lin, D., Gong, Y., & Cui, Y. (2018). Fundamental study on the wetting property of liquid lithium. *Energy Storage Materials*, *14*, 345–350.

13 Wang, S., Yue, J., Dong, W., Zuo, T., Li, J., Liu, X., Zhang, X., Liu, L., Shi, J., Yin, Y., & Guo, Y. (2019). Tuning wettability of molten lithium via a chemical strategy for lithium metal anodes. *Nature Communications*, *10*(1), 4930.

14 Fu, K., Gong, Y., Liu, B., Zhu, Y., Xu, S., Yao, Y., Luo, W., Wang, C., Lacey, S. D., Dai, J., Chen, Y., Mo, Y., Wachsman, E., & Hu, L. (2017). Toward garnet electrolyte–based Li metal batteries: An ultrathin, highly effective, artificial solid-state electrolyte/metallic Li interface. *Science Advances*, *3*(4), e1601659.

15 Tolganbek, N., Serikkazyyeva, A., Kalybekkyzy, S., Sarsembina, M., Kanamura, K., Bakenov, Z., & Mentbayeva, A. (2022). Interface modification of NASICON-type Li-ion conducting ceramic electrolytes: a critical evaluation. *Materials Advances*, *3*(7), 3055–3069.

16 Wang, Z., Tan, R., Wang, H., Yang, L., Hu, J., Chen, H., & Pan, F. (2017). A Metal–Organic-Framework-Based Electrolyte with Nanowetted Interfaces for High-Energy-Density Solid-State Lithium Battery. *Advanced Materials, 30*(2), 1704436.

17 Wang, L., Zhang, L., Wang, Q., Li, W., Wu, B., Jia, W., Wang, Y., Li, J., & Li, H. (2017). Long lifespan lithium metal anodes enabled by Al_2O_3 sputter coating. *Energy Storage Materials*, *10*, 16–23.

18 Il'ina, E., Druzhinin, K., Lyalin, E., Antonov, B., Pankratov, A., Vovkotrub, E., & Pryakhina, V. (2021). Influence of Al layer thickness on $Li_{6.6}Al_{0.05}La_3Zr_{1.75}Nb_{0.25}O_{12}$ solid electrolyte | Li anode interface in all-solid-state batteries. *Solid State Ionics*, *370*, 115736.

19 Pang, Y., Pan, J., Yang, J., Zheng, S., & Wang, C. (2021). Electrolyte/Electrode interfaces in All-Solid-State Lithium Batteries: A review. *Electrochemical Energy Reviews*, *4*(2), 169–193.

20 Li, C., Zhang, X., Zhu, Y., Zhang, Y., Xin, S., Wan, L., & Guo, Y. (2022b). Modulating the lithiophilicity at electrode/electrolyte interface for high-energy Li-metal batteries. *Energy Materials*, *1*(2), 100017.

21 Müller, A., Paravicini, L., Morzy, J., Krause, M., Casella, J., Osenciat, N., Futscher, M. H., & Romanyuk, Y.E. (2023). Influence of AU, PT, and C seed layers on lithium nucleation dynamics for Anode-Free Solid-State batteries. *ACS Applied Materials & Interfaces*, *16*(1), 695–703.

22 Nomura, Y., Yamamoto, K., Hirayama, T., Ouchi, S., Igaki, E., & Saitoh, K. (2019). Direct observation of a Li-Ionic Space-Charge layer formed at an Electrode/Solid-Electrolyte interface. *Angewandte Chemie International Edition*, *58*(16), 5292–5296.

23 De Klerk, N.J.J., & Wagemaker, M. (2018). Space-Charge layers in All-Solid-State batteries; important or negligible? *ACS Applied Energy Materials*, *1*(10), 5609–5618.

24 Lorger, S., Fischer, D., Usiskin, R., & Maier, J. (2019). Sputter deposition and thermal evaporation of Li_2O, Li_2S, and Li_2Se films. *Journal of Vacuum Science & Technology a Vacuum Surfaces and Films*, *37*(6).

25 Lou, J., Chen, K., Yang, N., Shuai, Y., & Zhu, C. (2021). Improved cycle stability of LiSn alloy anode for different electrolyte systems in lithium battery. *Nanomaterials*, *11*(2), 300.

26 Wan, M., Kang, S., Wang, L., Lee, H., Zheng, G.W., Cui, Y., & Sun, Y. (2020). Mechanical rolling formation of interpenetrated lithium metal/lithium tin alloy foil for ultrahigh-rate battery anode. *Nature Communications*, *11*(1), 829.

27 Serikkazyyeva, A., Mashekova, A., Uzakbaiuly, B., Bakenov, Z., & Mukanova, A. (2023). Novel Li/Li_xSn_y thin film designed as an anode for lithium-ion microbatteries. *Journal of Alloys and Compounds*, *965*, 171381.

28 Fu, K., Gong, Y., Liu, B., Zhu, Y., Xu, S., Yao, Y., Luo, W., Wang, C., Lacey, S.D., Dai, J., Chen, Y., Mo, Y., Wachsman, E., & Hu, L. (2017b). Toward garnet electrolyte–based Li metal batteries: An ultrathin, highly effective, artificial solid-state electrolyte/metallic Li interface. *Science Advances*, *3*(4), e1601659.

29 Zhong, X., Li, X., Yang, L., Wang, D., Qu, X., & Liu, H. (2021). Predicted stable structures of the Li–Ag system at high pressures. *The Journal of Physical Chemistry Letters*, *12*(6), 1671–1675.

30 Kato, A., Hayashi, A., & Tatsumisago, M. (2016). Enhancing utilization of lithium metal electrodes in all-solid-state batteries by interface modification with gold thin films. *Journal of Power Sources*, *309*, 27–32.

31 Sheng, O., Jin, C., Chen, M., Ju, Z., Liu, Y., Wang, Y., Nai, J., Liu, T., Zhang, W., & Tao, X. (2020). Platinum nanointerlayer enhanced interface for stable all-solid-state batteries observed via cryo-transmission electron microscopy. *Journal of Materials Chemistry A*, *8*(27), 13541–13547.

32 Liao, Y., Tong, Z., Fang, C., Liao, S., Chen, J., Liu, R., & Hu, S. (2021). Extensively Reducing Interfacial Resistance by the Ultrathin Pt Layer between the Garnet-Type Solid-State Electrolyte and Li–Metal Anode. *ACS Applied Materials & Interfaces*, *13*(47), 56181–56190.

33 Li, C., Muruganantham, R., Hsu, W., Ihrig, M., Hsieh, C., Wang, C., & Liu, W. (2023). Atomic layer deposition of ZnO on $Li_{1.3}Al_{0.3}Ti_{1.7}(PO_4)_3$ enables its application in all solid-state lithium batteries. *Journal of the Taiwan Institute of Chemical Engineers*, *144*, 104681.

34 Wen, Z., Li, Y., Zhao, Z., Qu, W., Chen, N., Xing, Y., Ma, Y., Li, L., Wu, F., & Chen, R. (2020). A leaf-like Al_2O_3-based quasi-solid electrolyte with a fast Li+ conductive interface for stable lithium metal anodes. *Journal of Materials Chemistry A*, *8*(15), 7280–7287.

35 Mochalov S.E., Nurgaliev A.R., Kuzmina E.V., Ivanov A.L., & Kolosnitsyn V.S. (2019). Specifics of magnetron sputtering of lithium from liquid-phase target. *Vacuum*, 68, 108816.

Information about the authors

Serikkazyyeva, Assel — Junior Researcher, National Laboratory Astana, Nazarbayev University, Astana, Kazakhstan; e-mail: assel.serikkazyyeva@nu.edu.kz, https://orcid.org/0000-0002-4567-3917

Yegamkulov, Mukagali — Junior Researcher, National Laboratory Astana, Nazarbayev University, Astana, Kazakhstan; e-mail: mukagali.yegamkulov@nu.edu.kz, https://orcid.org/0000-0002-1133-3201

Raiymbekov, Yessimzhan — Researcher, National Laboratory Astana, Nazarbayev University, Institute of batteries, Kazakhstan; e-mail: yessimzhan.raiymbekov@nu.edu.kz, https://orcid.org/0000-0003-3380-9263

Mukanova, Aliya (*corresponding author*) — Leading Researcher, PhD in Science, Engineering and Technology, Associate Professor, National Laboratory Astana, Nazarbayev University, Institute of batteries, Kazakhstan; e-mail: aliya.mukanova@nu.edu.kz, https://orcid.org/0000-0002-1171-176X

Uzakbaiuly, Berik — Researcher, Fraunhofer IKTS, Forchheim, Germany; https://orcid.org/0000-0002-0964-0392

Bakenov, Zhumabay — Professor, School of Engineering and Digital Sciences, Vice Provost for Industry Engagement, Nazarbayev University, Director, Center for Energy and Advanced Materials Science, National Laboratory Astana, Astana, Kazakhstan; e-mail: zbakenov@nu.edu.kz, https://orcid.org/0000-0003-2781-4955

Article
https://doi.org/10.31489/2025PH1/29-36
UDC 539.171.016

Received: 8.11.2024
Accepted: 24.01.2025

D. Soldatkhan[1], B. Mauyey[1,2*], A.A. Baratova[1], K.M. Makhanov[1]

[1]*L.N. Gumilyov Eurasian National University, Astana, Kazakhstan;*
[2]*Joint Institute for Nuclear Research, Dubna, Russia*
*(*Corresponding author's e-mail: bahytbek01@yandex.kz)*

Introduction of a New B3Y-Fetal Potential in the Semimicroscopic Analysis of the $^{15}N + ^{27}Al$ Nuclear System

The experimental data analysis of the low-energy elastic scattering process in the $^{15}N+^{27}Al$ nuclear system used a new microscopic approach. In the microscopic analysis, new B3Y-Fetal potentials, calculated using the variational method with lower-order constraints (LOCV) in two-body matrices, were applied. Based on the double folding model (DFM), the CDM3Y2-Paris, CDB3Y2-Fetal, and CDB3Y3-Fetal microfolding potentials were constructed by adjusting density-dependent parameters *C*, α, β, and γ. These density-dependent parameters were introduced based on the effective nucleon-nucleon (NN) interaction and the form factor of the nucleon density distribution of the colliding ^{15}N and ^{27}Al nuclei. The uniqueness of the analysis lies in the fact that the introduced density-dependent parameters were calculated using the optimal value of the *K* — compressibility factor, which characterizes the saturation properties of the nuclear medium. The optimal parameter sets for the optical and folding potentials were determined from the results of the optical model (OM) and DFM analyses. The theoretical cross-sections of elastic scattering obtained from phenomenological and microscopic analyses were found to describe the experimental data well. In the semi-microscopic analysis, the effectiveness of the B3Y-Fetal folding potential was determined. Based on the analysis of the experimental data of elastic scattering, it was concluded that the saturation properties of nuclear matter can be determined more accurately. The low-energy elastic scattering reaction in the $^{15}N+^{27}Al$ nuclear system is important for studying the properties of materials and nuclear fuels. This study of the nuclear process contributes to the development of future nuclear materials and energy technologies.

Keywords: microscopic analysis, elastic scattering, double folding model, B3Y-Fetal potential, nucleon density distribution.

Introduction

Studying the processes occurring during nuclear collisions helps to obtain valuable information about nuclear forces and their behavior, understand nuclear reaction mechanisms, and the structure of complex nuclei. Research on $^{15}N+^{27}Al$ nuclear systems has been actively conducted in recent years from both fundamental and applied science perspectives. Such studies make it possible to determine the energy levels and states of nuclei, which is important for the theoretical modeling of nuclear interactions.

Studying reactions between light elements such as ^{15}N and ^{27}Al helps to understand nucleosynthesis processes and model the evolution of stars, which is important for nuclear astrophysics. In nuclear energy, processes involving light nuclei like nitrogen and aluminum under thermonuclear synthesis conditions are considered as a potential future energy source. Understanding the effect of thermonuclear reaction products and fast neutrons on the high-energy characteristics of materials containing the ^{27}Al nucleus is one of the key aspects. Analyzing the $^{15}N+^{27}Al$ reaction aids in the development of radiation detectors and monitoring devices for nuclear reactors. Thus, the $^{15}N+^{27}Al$ system has a wide range of practical applications in nuclear energy, from fundamental research to technology and safety.

In addition to obtaining important information about nuclear structure and reaction mechanisms through the analysis of the elastic scattering process, it is possible to enhance the saturation properties of the nuclear medium. The saturation point of the binding energy density dependence, *K* — nuclear incompressibility, is directly related to the nuclear binding energy [1]. The approach to constructing the equation of state of a nucleus based on the overlap of nucleon densities of interacting nuclei is performed through a microscopic method. Constructing an effective NN-interaction potential dependent on nucleon density enables the calculation of the saturation properties of nuclear matter [2]. The novelty of this work lies in investigating the efficiency of using the effective NN-interaction B3Y-Fetal potential with density-dependent parameters *C,* α, β, γ. The effective NN-interaction B3Y-Fetal potential of Fiase, incorporating these density-dependent parameters, was recently obtained based on calculating nuclear matrix elements of two-body interactions using the LOCV method [3–6].

From this, an analysis was carried out on the basis of density — dependent parameters calculated at the value $\rho_0 = 0.17$ fm^{-3} of the actual density determined at the saturation point. The density-dependent α-parameters are determined in the effective NN-interaction formula in the DFM formula [7].

$$t_i(r_{NN}) = C_i\left[1 + \alpha_i \rho_{P(T)}^{2/3}\left(S_{P(T)}\right)\right] V_{KK}^i(r_{NN}), \quad (1)$$

where $V_{KK}^i(r_{NN})$ is the potential of singlet and triplet states.

In the articles Dao Khoa, 2 types of $F(p)$ — density-dependent form factor are proposed [8, 9]. The article identified density-dependent parameters C, α, β, γ — at optimal values of the K-incompressibility factor and analyzed in a wide energy range [9–12].

The folding model allows modification of the density-dependent form factor of nucleon distributions taking into account the ideas of microscopic theory. Therefore, the properties of nuclear matter can be described more clearly using effective NN-interaction. No such analysis has been done for system ^{15}N+^{27}Al. In our upcoming work [13, 14], analyses were made using the new B3Y-Fetal potential that resulted in global dependencies.

Calculation of the K-incompressibility factor depending on the saturation property of the nucleus

To increase the saturation property of nuclear matter, the equilibrium condition of the density-dependent specific bond energy is sufficient. We apply density-dependent parameters calculated for the equilibrium condition to the effective NN-interaction M3Y potential. In particular, it is necessary to construct the equations of state at the value $\rho_0 = 0.17$ fm^{-3} of the saturation density of nuclear matter. Specific binding energy of density-dependent infinite nuclear matter [4, 8]:

$$\frac{\varepsilon_0}{A}(\rho) = \frac{3\hbar^2 k_F^2}{10m} + F(\rho)\frac{\rho}{2}\left(J_D + \int\left[\hat{j}_1(k_F r)\right]^2 \upsilon^{EX}(r) d^3 r\right), \quad (2)$$

where m is the mass of the nucleon; J_D is the integral obtained by volume from the direct part of the interaction $\hat{j}_1(x) = \frac{3\mathrm{j}1(x)}{X}$ — Bessel spherical function ($n = 1$), ρ is the density of the nucleons, k_F is the Fermi momentum.

From the equilibrium saturation condition of the binding energy of the nucleus:

$$\frac{d\varepsilon}{d\rho} = \frac{\hbar^2 k_F^2}{5mp} + \frac{J_D C}{2}\left(1 - \frac{5}{3}\beta(\varepsilon)\rho^{2/3}\right) = 0. \quad (3)$$

Based on the density-dependent parameters from Equations (4) and (3), the ε — bond energy formula is written as follows:

$$\varepsilon = \frac{3\hbar^2 k_F^2}{10m} + \frac{\rho J_D}{2} C\left(1 - \beta(\varepsilon)\rho^{2/3}\right). \quad (4)$$

Density-dependent c, β — parameters and ρ_0 — actual (saturation) density [4]:

$$C = -\frac{2\hbar^2 k_F^2}{5mJ_D\rho\left(1 - \frac{5}{3}\beta(\varepsilon)\rho^{\frac{2}{3}}\right)} \quad (5)$$

$$\beta(\varepsilon) = \frac{(3-3p)}{(9-5p)} \cdot \frac{1}{\rho^{5/3}}, \quad (6)$$

$$\rho_0 = -\frac{10m\varepsilon}{\hbar^2 (1.5\pi^2\rho)^{2/3}}. \quad (7)$$

The nuclear incompressibility factor is calculated by the following equation [4]:

$$K_\infty = \left[-\frac{3\hbar^2 k_F^3}{5m} + 5J_D C\beta(\varepsilon)\rho^{5/3}\right]_{\rho=\rho_0}. \quad (8)$$

The saturation density point ($\rho_0 = 0.17$ fm^{-3}) defined according to the specific binding energy of the nucleus using the B3Y-Fetal interactionand shown in Figure 1 [4].

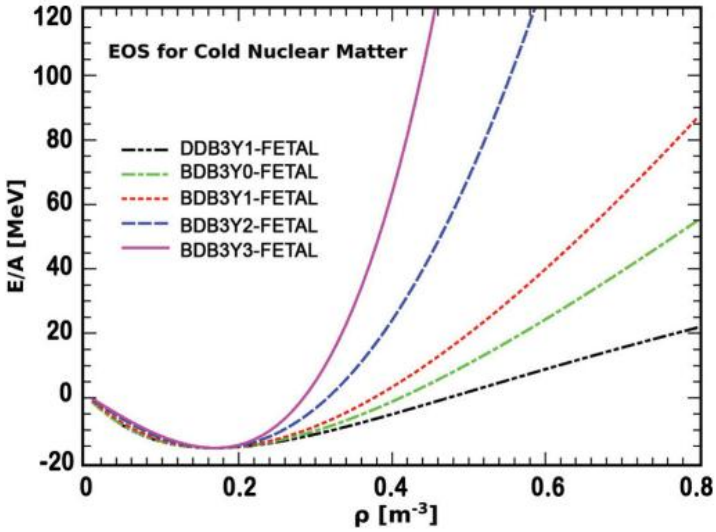

Figure 1. Saturation point of the core binding energy density dependence [4]

NN-interaction on effective forces M3Y-Paris and B3Y-Fetal potentials

The interaction potential for effective NN forces consists of the sum of the $U^D\left(\vec{R}\right)$ — direct and $U^{EX}\left(\vec{R}\right)$ — exchange potentials.

$$U\left(\vec{R}\right)=U^D\left(\vec{R}\right)+U^{EX}\left(\vec{R}\right). \tag{9}$$

Double integrated direct potential on the distribution of nucleons of beam and target nuclei [15, 16]:

$$U^D\left(\vec{R}\right)=\iint\rho^{(1)}\left(r_1\right)\upsilon_D\left(s\right)\rho^{(2)}\left(r_2\right)dr_1dr_2\,, \tag{10}$$

where $\upsilon_D\left(\vec{s}\right)$ — direct component of effective interaction; $\rho^{(i)}\left(r_i\right)$ — nucleon density of colliding nuclei; s — effective NN-interaction distance, $s=r_2-r_1+R$.

Double integrated Exchange potential on the distribution of nucleons of beam and target nuclei [16, 17]:

$$U^{EX}\left(\vec{R}\right)=\iint\rho^{(1)}\left(\vec{r}_1,\vec{r}_1+\vec{s}\right)\upsilon_{EX}\left(\vec{s}\right)\rho^{(2)}\left(\vec{r}_2,\vec{r}_2-\vec{s}\right)\exp\left[i\vec{k}\left(\vec{R}\right)\vec{s}/\eta\right]d\vec{r}_1d\vec{r}_2\,, \tag{11}$$

where $\upsilon_{EX}\left(\vec{s}\right)$ — effective NN-interaction exchange component, $\rho^{(i)}\left(\vec{r},\vec{r}'\right)$ — density matrix of colliding nuclei.

Matrix in singlet, triplet states of nucleon interaction (Hartree Fock) calculation for coefficients direct and transition components [18]:

$$\upsilon_{D(EX)}=1/16\left(3\upsilon^c_{TE}+3\upsilon^c_{SE}\pm9\upsilon^c_{T0}\pm\upsilon^c_{S0}\right), \tag{12}$$

where the triplet and singlet components of the central forces are even $\left(\upsilon^c_{TE},\upsilon^c_{SE}\right)$ and odd $\left(\upsilon^c_{T0},\upsilon^c_{S0}\right)$ [19].

Direct and exchange components based on the G-matrix element of the M3Y-Paris potential [20].

$$\upsilon_D\left(s\right)=11061.6\frac{\exp(-4s)}{4s}-2537.5\frac{\exp(-2.5s)}{2.5s}\,, \tag{13}$$

$$\upsilon_D\left(s\right)=-1524.0\frac{\exp(-4s)}{4s}-518.8\frac{\exp(-2.5s)}{2.5s}-7.8474\frac{\exp(-0.7072s)}{0.7072s}\,. \tag{14}$$

The direct and transition components based on the *G*-matrix element of the B3Y-Fetal potential is given in the radial form of the isoscalar part [6, 14]:

$$\upsilon_D\left(s\right)=10472.13\frac{\exp(-4s)}{4s}-2203.11\frac{\exp(-2.5s)}{2.5s}, \tag{15}$$

$$\upsilon_{EX}\left(s\right)=499.63\frac{\exp(-4s)}{4s}-1347.77\frac{\exp(-2.5s)}{2.5s}-7.8474\frac{\exp(-0.7072s)}{0.7072s}\,. \tag{16}$$

The theory of semi-microscopic analysis

When analyzing experimental data of elastic scattering within the framework of an optical model (OM), the Woods-Saxon form of potential was used.

$$U(r) = V_o\left[1+\exp\left(\frac{r-R_V}{a_V}\right)\right] - iW_o\left[1+\exp\left(\frac{r-R_W}{a_W}\right)\right] + V_C(r), \quad (17)$$

where V_o, W_V, a_V, a_W, R_V, R_W are real, imaginery potentials, diffusion, radius, $V_C(r)$ is the Coulomb potential.

In a semi-microscopic analysis, we replace the real part of the op with the $V_F(r)$ — folding potential:

$$U(r) = N_r\left[V_D(r) + V_{EX}(r)\right] - iW_o\left[1+\exp\left(\frac{r-R_W}{a_W}\right)\right] + V_C(r), \quad (18)$$

where N_r is a re-rationing factor of the folding potential.

The folding potential of an effective NN-interaction [17]:

$$V_F = \iint \rho_1(r_1)\rho_2(r_2)\vartheta_{NN}(s)d^3r_1d^3r_2, \quad (19)$$

where ϑ_{NN} is the effective NN-interaction potential; $\rho_1(r_1)$ and $\rho_2(r_2)$ is the distribution of the matter density of the beam and target nuclei, respectively.

$V_C(r)$ — the Coulomb potential is defined as follows:

$$V_C(R) = \begin{cases} \dfrac{Z_1Z_2e^2}{2R_C}\left(3-\dfrac{R^2}{R_C}\right) & \text{For} \quad R \le R_C \\ \dfrac{Z_1Z_2e^2}{R} & \text{For} \quad R \ge R_C \end{cases} \quad (20)$$

For the ^{15}N-core, the harmonic-oscillator model was selected as the distribution of the density of matter [21]:

$$\rho(r) = \rho_0\left(1+\alpha(r/a)^2\right)\exp\left(-(r/a)^2\right), \quad (21)$$

where α = 1.756 fm, a = 1.29 fm [22].

For the ^{27}Al core, the two-parameter Fermi modelwas selected as the distribution of the density of matter [21]:

$$\rho(r) = \rho_0 \Big/ \left(1+\exp\left(\frac{r-c}{z}\right)\right), \quad (22)$$

where c = 3.07 fm, z = 0.519 fm [22].

Dependence function of direct and exchange potentials [8].

$$\upsilon_{D(EX)}(\rho, r) = g(E)f(\rho)\upsilon'_{D(EX)}(r), \quad (23)$$

where $g(E)$ — energy dependent type; ρ — density of the overlapping medium of nucleons of nuclei; r is the distance between the interacting nucleons.

In the process of elastic scattering, there is a re-distribution of energy between the colliding nuclei. Energy dependent type [13].

$$g(E) = 1 - 0.003(E/A). \quad (24)$$

A type proposed by Dao Khoa of introducing density-dependent C, α, β — parameters to the effective NN-interaction [6]:

$$1)\ f(\rho) = C\left(1+\alpha e^{-\beta\rho}\right), \quad \text{the DDM3Y-type,} \quad (25)$$

$$2)\ f(\rho) = C\left(1-\alpha\rho^{\beta}\right), \quad \text{the BDM3Y-type.} \quad (26)$$

Based on this $f(p)$ — density-dependent form factor, you can enter density-dependent parameters for the correct values of K-incompressibility [8, 13]. γ — parameter dependent formula [6, 13]:

$$f(\rho) = C\left(1+\alpha\exp(-\beta\rho) - \gamma\rho\right). \quad (27)$$

Table 1

Density-dependent modified microfolding potentials [6, 22]

Density dependence	C	α	β (fm^3)	γ (fm^3)	K (MeV)
CDM3Y2-Paris CDB3Y2-Fetal	0.3346	3.0357	3.0685	1.0	204
CDB3Y3-Fetal	0.2985	3.4528	2.6388	1.5	217

Discussion of results

At energies E_{Lab} = 33 MeV, E_{Lab} = 48 MeV, E_{Lab} = 62 MeV, E_{Lab} = 70 MeV [23], for the nuclear system $^{15}N+^{27}Al$, phenomenolic and semi-microscopic analyses of experimental data of elastic scattering were performed.

The analysis used density-dependent CDM3Y2-Paris, CDB3Y2-Fetal and CDB3Y3-Fetal folding potentials. All OM and DFM calculations were carried out on the basis of using the Fresco Code [24]. The following figure shows the result of the OM and DFM analyzes and shown in Figures 2–5.

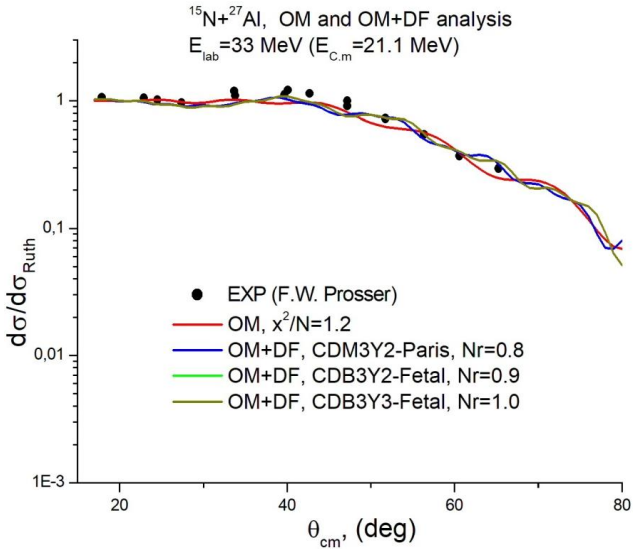

Figure 2. Results of the analysis of OM and DFM

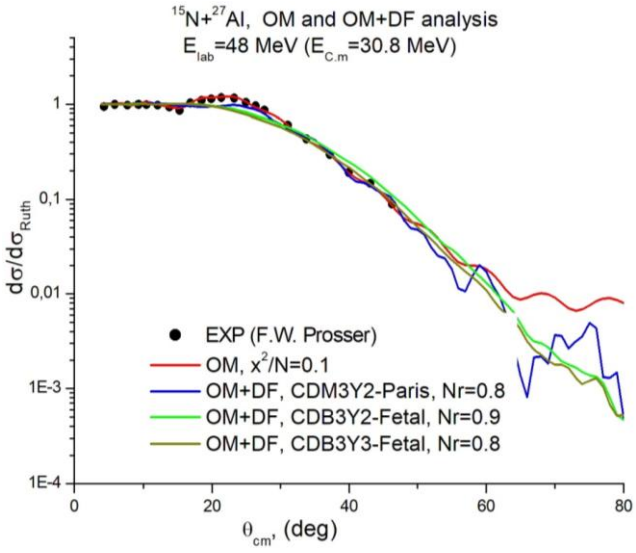

Figure 3. Results of the analysis of ohms and DFM

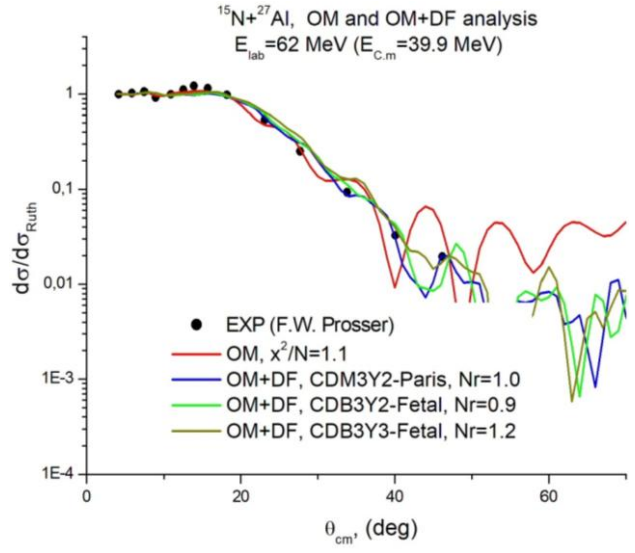

Figure 4. Results of the analysis of ohms and DFM

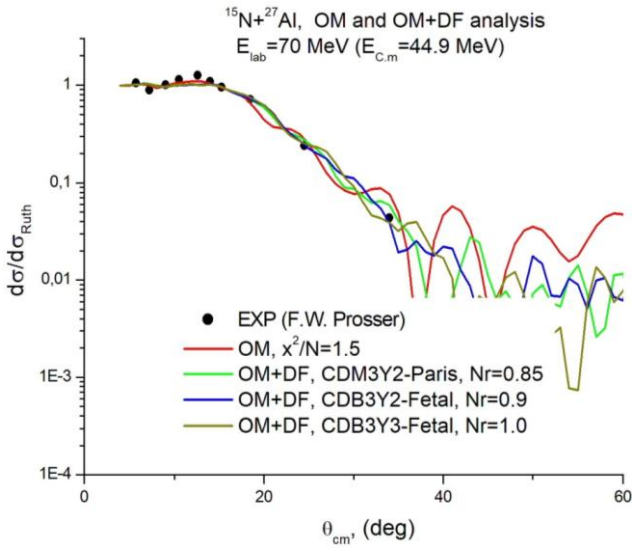

Figure 5. Results of the analysis of OM and DFM

Microfolding potentials CDM3Y2-Paris, CDB3Y2-Fetal, CDB3Y3-Fetal were used in the OM+DF analysis. The N_r — re-rationing factor was determined at intervals of 0.8–1.2.

The values of the optimal parameters for theoretical analysis are shown in Table 2. There is an energy dependence of the characteristics of the parameters.

Table 2

Parameters of OM and DFM analysis for $^{15}N+^{27}Al$ system

E (MeV)	Model	Type of real potential			N_R	Imaginary potential parameter (WS)			σ_R (mb)	χ^2/N
		V_0 (MeV)	Rv (fm)	av (fm)		W_0 (MeV)	r_W (fm)	a_W (fm)		
33	OM	280.0	0.97	0.5	–	4.6	1.2	1.15	1093	1.2
	OM+DF	CDM3Y2-Paris			0.8	4.6	1.2	1.15	1085	–
	OM+DF	CDB3Y2-Fetal			0.9	4.6	1.2	1.17	1055	–
	OM+DF	CDB3Y3-Fetal			1.0	4.6	1.2	1.17	1055	–
48	OM	240.8	1.13	0.5	–	24.9	1.37	0.2	1552	0.1
	OM+DF	CDM3Y2-Paris			0.8	24.9	1.37	0.2	1602	–
	OM+DF	CDB3Y2-Fetal			0.9	24.9	1.37	0.2	1570	–
	OM+DF	CDB3Y3-Fetal			0.8	24.9	1.37	0.2	1554	–
62	OM	279.9	1.04	0.47	–	4.6	1.24	1.17	1834	0.1
	OM+DF	CDM3Y2-Paris			1.0	4.6	1.24	1.17	1848	–
	OM+DF	CDB3Y2-Fetal			0.9	4.6	1.24	1.17	1782	–
	OM+DF	CDB3Y3-Fetal			1.2	4.6	1.24	1.17	1820	–
70	OM	240.8	1.13	0.5	–	24.9	1.37	0.2	1904	0.5
	OM+DF	CDM3Y2-Paris			0.85	24.9	1.37	0.2	1894	–
	OM+DF	CDB3Y2-Fetal			0.9	24.9	1.37	0.2	1885	–
	OM+DF	CDB3Y3-Fetal			1.0	24.9	1.37	0.2	1910	–

Conclusion

• A semi-microscopic analysis was carried out for the $^{15}N+^{27}Al$ system using the new B3Y-Fetal potential calculated on the basis of LOCV.

• Density-dependent parameters C, α, β, γ were introduced into the new B3Y-Fetal potential, and the CDM3Y2-Paris, CDB3Y2-Fetal, and CDB3Y3-Fetal folding potentials were created. Theoretical elastic scattering cross sections have been determined for the $^{15}N+^{27}Al$ system.

• The efficiency of the microscopic CDB3Y-Fetal potential was determined for the $^{15}N+^{27}Al$ system. The accuracy of the analysis of OM was determined in the range of $\chi^2/N = 0.1–1.8$. The reordering coefficient of semi-microscopic analysis was determined at the interval $N_r = 0.8–1.2$.

• Density-dependent study of the B3Y-Fetal potential, created on the basis of LOCV made it possible to clarify the saturation property of nuclear matter, to fully take into account nuclear forces.

Acknowledgment

This research has been funded by the Science Committee of the Ministry of Science and Higher Education of the Republic of Kazakhstan (Grant No. AP13268907).

References

1. Ochala, I., Fiase, J.O., & Anthony, E. (2017). Computation of nuclear binding energy and incompressibility with a new M3Y-type effective interaction. *Int Res J Pure Applied Physics*, *5*, 5–13.
2. Khoa, D.T., Satchler, G.R., & Von Oertzen, W. (1997). Nuclear incompressibility and density dependent NN interactions in the folding model for nucleus-nucleus potentials. *Physical Review C*, *56*(2), 954. https://doi.org/10.1103/PhysRevC.56.954.
3. Fiase, J.O., Devan, K.R.S., & Hosaka, A. (2002). Mass dependence of M3Y-type interactions and the effects of tensor correlations. *Physical Review C*, *66*(1), 014004. https://doi.org/10.1103/PhysRevC.66. 014004.
4. Ochala, I., & Fiase, J.O. (2018). Symmetric nuclear matter calculations: A variational approach. *Physical Review C*, *98*(6), 064001. https://doi.org/10.1103/PhysRevC.98.064001.
5. Ochala, I., Fiase, J.O., Gbaorun, F., & Bamikole, J.A. (2021). A Study of Asymmetric Nuclear Matter with the B3Y-Fetal Effective Interaction. *International Research Journal of Pure and Applied Physics*, *8*(2), 10–35. https://doi.org/10.37745/irjpap.13.

6. Ochala, I., & Fiase, J.O. (2021). B3Y-FETAL effective interaction in the folding analysis of elastic scattering of $^{16}O+^{16}O$. *Nuclear Science and Techniques*, *32*(8), 81. https://doi.org/10.1007/s41365-021-00920-z.
7. Majka, Z., Gils, H.J., & Rebel, H. (1978). 104 MeV alpha particle and 156 MeV6Li scattering and the validity of refined folding model approaches for light complex projectile scattering. *Zeitschrift für Physik A Atoms and Nuclei*, *288*(2), 139–152.
8. Khoa, D.T., Von Oertzen, W., & Bohlen, H.G. (1994). Double-folding model for heavy-ion optical potential: Revised and applied to study C12 and O16 elastic scattering. *Physical Review C*, *49*(3), 1652. https://doi.org/10.1103/PhysRevC.49.1652.
9. Khoa, D.T., & Von Oertzen, W. (1995). Refractive alpha-nucleus scattering: a probe for the incompressibility of cold nuclear matter. *Physics Letters B*, *342*(1-4), 6–12. https://doi.org/10.1016/0370-2693(94)01393-Q.
10. Amangeldi, N., Burtebayev, N., Soldatkhan, D., Nassurlla, M., Mauyey, B., Yergaliuly, G., ... & Hamada, S. (2024). Recent Measurement and Theoretical Analysis for the Elastic Scattering of the $^{15}N+^{11}B$ System. *Brazilian Journal of Physics*, *54*(5), 169. https://doi.org/10.1007/s13538-024-01547-2
11. Amangeldi, N., Burtebayev, N., Artemov, S. V., Nassurlla, M., Mauyey, B., Yergaliuly, G., ... & Hamada, S. (2024). Efficiency of the new B3Y-fetal potential in the analysis of the elastic and inelastic angular distributions for the $^{10}B+^{12}C$ system. *Pramana*, *98*(3), 106. https://doi.org/10.1007/s12043-024-02760-z.
12. Soldatkhan, D., Amangeldi, N., Baltabekov, A.S., & Yergaliuly, G. (2022). Investigation of the energy dependence of the interaction potentials of the $^{16}O+^{12}C$ nuclear system with a semi-microscopic method. https://doi.org/10.31489/2022No3/39-44.
13. Soldatkhan, D., Yergaliuly, G., Amangeldi, N., Mauyey, B., Odsuren, M., Ibraheem, A.A., & Hamada, S. (2022). New Measurements and Theoretical Analysis for the $^{16}O+^{12}C$ Nuclear System. *Brazilian Journal of Physics*, *52*(5), 152. https://doi.org/10.1007/s13538-022-01153-0.
14. Soldatkhan, D., Amangeldi, N., Makhanov, K.M., Smagulov, Zh.K. (2023). Application of the new B3Y-Fetal potential in the semi-microscopic analysis of the scattering of accelerated ^{6}Li — lithium and ^{16}O — oxygen nuclei from the ^{12}C — carbon nucleus. *Eurasian Physical Technical Journal*, 25, 4(46), 22–30.
15. Khoa, D.T., & Satchler, G.R. (2000). Generalized folding model for elastic and inelastic nucleus–nucleus scattering using realistic density dependent nucleon–nucleon interaction. *Nuclear Physics A*, *668*(1–4), 3–41.
16. Kobos, A.M., Brown, B.A., Lindsay, R., & Satchler, G.R. (1984). Folding-model analysis of elastic and inelastic α-particle scattering using a density-dependent force. *Nuclear Physics A*, *425*(2), 205–232. https://doi.org/10.1016/0375-9474(84)90073-3.
17. Satchler, G.R. (2005). Folding models for elastic and inelastic scattering. In *Heavy-Ion Collisions: Proceedings of the International Summer School Held in Rábida (Huelva), Spain, June 7–18, 1982* (pp. 25–43). Berlin, Heidelberg: Springer Berlin Heidelberg.
18. Bertsch, G., Borysowicz, J., McManus, H., & Love, W.G. (1977). Interactions for inelastic scattering derived from realistic potentials. *Nuclear Physics A*, *284*(3), 399–419. https://doi.org/10.1016/0375-9474(77)90392-X.
19. Anantaraman, N., Toki, H., & Bertsch, G.F. (1983). An effective interaction for inelastic scattering derived from the Paris potential. *Nuclear Physics A*, *398*(2), 269–278.
20. Khoa, D.T., Phuc, N.H., Loan, D.T., & Loc, B.M. (2016). Nuclear mean field and double-folding model of the nucleus-nucleus optical potential. *Physical Review C*, *94*(3), 034612.
21. De Vries, H., De Jager, C.W., & De Vries, C. (1987). Nuclear charge-density-distribution parameters from elastic electron scattering. *Atomic data and nuclear data tables*, *36*(3), 495–536. https://doi.org/10.1016/0092-640X(87)90013-1.
22. Ochala, I., Gbaorun, F., Bamikole, J.A., & Fiase, J.O. (2019). A Microscopic Study of Nuclear Symmetry Energy with an Effective Interaction Derived from Variational Calculations. *Int Res J Pure Applied Physics*, *6*, 22–33.
23. Prosser Jr, F.W., Racca, R.A., Daneshvar, K., Geesaman, D.F., Henning, W., Kovar, D.G., ... & Tabor, S.L. (1980). Complete fusion of N15+Al27. *Physical Review C*, *21*(5), 1819.
24. Thompson, I.J. (1988). Getting started with FRESCO. *Comput. Phys. Rep*, *7*, 167–212.

Д. Солдатхан, Б. Мауей, А.А. Баратова, К.М. Маханов

$^{15}N + ^{27}Al$ ядролық жүйені жартылай микроскопиялық талдау кезінде жаңа B3Y-Fetal потенциалын енгізу

$^{15}N+^{27}Al$ ядролық жүйенің төмен энергиядағы серпімді шашырау процесінің эксперименттік деректерін талдауда жаңа микроскопиялық тәсіл қолданылды. Микроскопиялық талдауда екі дене матрицасында төменгі ретті шектеулері бар вариациялық тәсілде (LOCV) есептелген жаңа B3Y-Fetal потенциалдары пайдаланылды. Екілік фолдинг модель (DFM) негізінде тығыздыққа тәуелді *C*, α, β, γ — параметрлерді реттеу арқылы CDM3Y2-Paris, CDB3Y2-Fetal және CDB3Y3-Fetal микрофолдинг потенциалдары құрылды. Тығыздыққа тәуелді параметрлер тиімді нуклон-нуклондық (NN) өзара әрекеттесуі негізінде соқтығысқан ^{15}N және ^{27}Al ядролардың нуклондар тығыздығының таралуының форм-факторы бойынша енгізілді. Талдаудың ерекшелгі енгізілген тығыздыққа тәуелді параметрлер ядролық ортаның қанықтылық қасиетін сипаттайтын *K* — сығылмаушылық факторының оңтайлы мәнінде есептелген. Оптикалық модель (ОМ) және DFM талдаулар нәтижесінде оптикалық және фолдинг потенциалдардың оңтайлы параметрлер жиынтығы табылды. Феноменологиялық және

микроскопиялық талдау нәтижелерінде серпімді шашыраудың теориялық қималары эксперименттік деректерді жақсы сипаттай алды. Жартылай микроскопиялық талдауда B3Y-Fetal фолдинг потенциалдың тиімділігі анықталды. Серпімді шашыраудың эксперименттік деректерін талдау негізінде ядролық материяның қанықтылық қасиетін дәлірек анықтауға болады деген қорытынды жасалды. $^{15}N + ^{27}Al$ ядролық жүйенің төмен энергиядағы серпімді шашырау реакциясы материалдар мен ядролық отындардың қасиеттерін зерттеу үшін маңызды. Бұл ядролық процесін зерттеу жұмысы болашақ ядролық материалдар мен энергетикалық технологияның дамуына үлес қосады.

Кілт сөздер: микроскопиялық талдау, серпімді шашырау, екілік фолдинг моделі, B3Y-Fetal потенциалы, нуклондар тығыздығының таралуы

Д. Солдатхан, Б. Мауей, А.А. Баратова, К.М. Маханов

Введение нового потенциала B3Y-Fetal при полукомикроскопическом анализе ядерной системы $^{15}N + ^{27}Al$

В экспериментальном анализе процесса упругого рассеяния на ядерной системе $^{15}N + ^{27}Al$ при низких энергиях был применен новый микроскопический метод. В микроскопическом анализе использовались новые потенциалы B3Y-Fetal, рассчитанные в вариационном методе с ограничениями низшего порядка в двухтелевой матрице (LOCV). На основе модели двойного фолдинга (МДФ) были построены микрофолдинг потенциалы CDM3Y2-Paris, CDB3Y2-Fetal и CDB3Y3-Fetal. Эти потенциалы были получены путем настройки плотностных параметров *C*, α, β, γ. Зависимые от плотности параметры вводились с учетом эффективного взаимодействия нуклон-нуклонность (NN) через форм-фактор распределения плотности нуклонов в столкнувшихся ядрах ^{15}N и ^{27}Al. Особенностью исследования является расчет введенных плотностных параметров при оптимальном значении сжимаемости — *K*, описывающем насыщение ядерного вещества. Результаты анализа оптической модели (ОМ) и МДФ показали оптимальные значения параметров оптических и фолдинг потенциалов. Теоретические сечения упругого рассеяния, полученные в феноменологическом и микроскопическом анализах, хорошо согласуются с экспериментальными данными. В полумикроскопическом анализе была определена эффективность фолдинг потенциала B3Y-Fetal. На основе анализа экспериментальных данных упругого рассеяния можно сделать вывод о возможности более точного определения насыщающих свойств ядерной материи. Упругое рассеяние на ядерной системе $^{15}N+^{27}Al$ при низких энергиях важно для исследования свойств материалов и ядерного топлива. Это исследование ядерного процесса способствует дальнейшему развитию ядерных материалов и энергетических технологий.

Ключевые слова: микроскопический анализ, упругое рассеяние, модель двойного фолдинга, потенциал B3Y-Fetal, распределение плотности нуклонов

Information about the authors

Soldatkhan, Dauren — PhD, Senior Teacher, L.N. Gumilyov Eurasian National University, Astana, Kazakhstan; SCOPUS Author ID: 57768566200; ORCID ID https://orcid.org/0000-0001-7981-4100; e-mail: soldathan.dauren@gmail.com.

Mauyey, Bahytbek (*corresponding author*) — PhD, Senior Teacher, Joint Institute for Nuclear Research, Dubna, Russia; L.N. Gumilyov Eurasian National University, Astana, Kazakhstan; SCOPUS Author ID: 57193847043; ORCID ID: https://orcid.org/0000-0003-4301-1327; e-mail: bahytbek01@yandex.kz.

Baratova, Aliya — Candidate of physico-mathematical sciences, Senior Teacher, L.N. Gumilyov Eurasian National University, Astana, Kazakhstan; SCOPUS Author ID 55221822500; ORCID ID: https://orcid.org/0000-0002-7015-3657; e-mail: baratova_aa@enu.kz.

Makhanov, Kanat — Candidate of physico-mathematical sciences, L.N. Gumilyov Eurasian National University, Astana, Kazakhstan; SCOPUS Author ID: 57217354220; ORCID ID: https://orcid.org/0000-0002-1263-0734; e-mail: makanov@inbox.ru

Article
https://doi.org/10.31489/2025PH1/37-44
UDC 537.52
Received: 11.11.2024
Accepted: 21.01.2024

T. Koshtybayev[1*], A. Tatenov[1], M. Aliyeva[2], K. Zhantleuov[2]

[1]*Kazakh National Women's Pedagogical University, Almaty, Kazakhstan;*
[2]*Abai Kazakh National Pedagogical University, Almaty, Kazakhstan*
*(*Corresponding author's e-mail: koshtybayev70@mail.ru)*

Influence of a Constant Magnetic Field and a High-Frequency Electric Field on Plasma

A new method of determining the expression of the averaged high-frequency pressure force (Miller force) based on the solution of the kinetic equation for the electron distribution function and the method of successive approximations (separation of slow motions and fast oscillations) is proposed for the case when a high-frequency electric field and a stationary magnetic field acting simultaneously on weakly inhomogeneous plasma. Moreover, widely recognized methods of theoretical and mathematical physics, such as averaging over the period of oscillation of the electric field and integration over the trajectory, have been applied. Collisions between electrons and stationary ions have been considered. The electric field amplitude is considered a slowly varying function of time and coordinates. The obtained expression allows us to estimate the influence of collisions of plasma particles on the Miller force, and under limiting conditions it coincides with the known expressions for the high-frequency pressure force derived from the equation of plasma electrons motion in high-frequency fields. The calculations neglect the contribution of the magnetic component of the electromagnetic field, which is applicable to longitudinal electric fields. The results obtained in this article are primarily of theoretical interest and reveal the interaction of weakly inhomogeneous plasma with a high-frequency electric field. They can also be used in constructing the kinetic theory of inhomogeneous plasma in high frequency electromagnetic fields.

Keywords: weakly inhomogeneous plasma, plasma electrons, kinetic equation, averaged force, electric field, particle collisions, fixed ions, high frequency

Introduction

It is known that in high-frequency electromagnetic fields, particles (specifically, electrons) experience not only the generalized Lorentz force $\vec{F}_0$ but also an additional force $\vec{f}_M$ determined by the high-frequency quasi-potential U_e, i.e., $\vec{f}_M = -n_e grad_{\vec{r}} U_e$ where n_e is the electron concentration. As a result of its action, the plasma electrons tend to move to the field minimum. The physics of such a phenomenon can be explained as follows. The electromagnetic field, causing high-frequency oscillations of electrons with velocity $\vec{\upsilon}_e$ creates as if an additional high-frequency pressure $P_{вч} \sim n_e m_e \upsilon_e^{\,2}$ (or $P_{вч} \sim n_e U_e$, where m_e is the electron mass), as a result of which the plasma electrons are displaced from the areas occupied by the field. In oscillatory motion, the force $\vec{f}_M = -grad_{\vec{r}} P_{вч}$ is directed against the displacement of electrons, so when an electron is displaced to the right, a return force of greater magnitude acts on it compared to when it is displaced to the left. The averaged force $\vec{f}_M$, so called the high-frequency pressure force, or sometimes the quasi-potential Miller force, do not depend on the particle charge sign. An expression for the studied force, based on the equation of motion of electrons, was defined in the works of a number of authors [1–4], devoted to the acceleration of plasma particles and the confinement of high-temperature plasma by high-frequency electromagnetic fields. In this article, the expression for the Miller force is derived from the kinetic equation for the electron distribution function, taking into account electron-ion collisions and the influence of longitudinal, high-frequency, and inhomogeneous electric fields and stationary magnetic fields on weakly inhomogeneous magnetically active plasma. This is done using the method of successive approximations (separation of slow motions and fast oscillations).

In this regard, this article addresses the problem of the impact of high-frequency electric and constant magnetic fields on weakly inhomogeneous plasma. In particular, the contributions of external fields to the kinetics of weakly inhomogeneous plasma in the approximation of pair collisions between particles are evaluated. Expressions for the collision integrals of electrons with electrons and electrons with stationary ions, as well as for the force of high-frequency pressure, are also determined, taking into account the

presence of a high-frequency longitudinal electric field and a constant magnetic field. Despite the increased interest in research in this direction, the question of the mechanisms of plasma behavior in external fields is far from fully studied and remains open, which makes the topic of the article relevant.

Materials and Methods

Motion of charged particles in electric and magnetic fields based on classical physics concepts, has been studied in papers [5–8]. These concepts not only remain valid when analyzing the motion of charged particles under the influence of macroscopic external fields but also form the foundation required for understanding processes of particle interaction in plasma — processes involving the microscopic fields of single particles. When analytically investigating various properties of plasma, one of the common methods is the kinetic equations approach. Although the Landau, Klimontovich, Lenard-Balescu-Silin, etc. equations have long been known in kinetic theory, the interest in this area of plasma physics remains unabated. In addition, widely recognized methods of theoretical and mathematical physics have been applied in plasma research, such as averaging over the period of oscillation of the electric field and integration over trajectory.

Literature review

The external high-frequency pressure force from the equation of motion is considered in the literature [1–4] in the case of a plasma without an external magnetic field and homogeneous. In the literature [5–10], one can become familiar with the interactions between plasma and external fields, kinetic processes, and electrophysical laws. Additionally, the results of recent years, which have been added to the kinetic theory of ionized plasma, are analyzed and discussed in references [11–18].

Main part. Experimental

Assume that the plasma, except for the high-frequency field

$$\vec{E} = \vec{E}_0\left(\varepsilon\vec{r}, \varepsilon t\right)\sin\omega_0 t \tag{1}$$

is influenced by an external constant magnetic field $\vec{B}_o$, oriented along the axis z. The kinetic equation for the electron distribution function F_e, considering the collisions of electrons with ions and effecting external fields, is written in the form of [9–12]

$$\frac{\partial F_e}{\partial t} + \vec{\upsilon}\frac{\partial F_e}{\partial \vec{r}} - \vec{F}_o\frac{\partial F_e}{\partial \vec{p}} = St_{ei}\left\{F_e\right\}, \tag{2}$$

$$\vec{F}_o = e\left(\vec{E} + \frac{1}{c}\left[\vec{\upsilon}\vec{B}_o\right]\right),$$

where $\vec{\upsilon} = \vec{p}/m_e$ is the electron velocity. The field amplitude $\vec{E}_0$ is considered a slowly varying function of time t and as per coordinates $\vec{r}$. The parameter ε characterizing the slowness of the amplitude change, fulfills the condition $\varepsilon = \left(V_T/\omega_0 L\right) << 1$, where V_T is the electron thermal velocity, ω_0 is the frequency, and L is typical value of the change F_e. When referring to high field frequencies, we assume that during the period of field oscillation, the electron travels a distance much shorter than its free path length, and thus can be considered to move in an almost homogeneous field [13–16]. Here $l_{\omega_0} = V_T\omega_0^{-1}$ and $l = V_T\nu_{ei}^{-1}$; ν_{ei} is the frequency of electron-ion collisions. We will assume that the plasma is weakly inhomogeneous, i.e., the functions F_e and $\vec{E}$ do not change much at a distance of the Debye radius r_d or the condition $\left(L/\upsilon_0 T\right) >> 1$ is fulfilled, where υ_0 is the average particle velocity.

As known, the collision integral characterizes the change in the particle distribution function due to collisions between them. It has dimensionality F/t, where is the F distribution function. The characteristic time t of change F due to time-of-collisions between particles, i.e. $t \sim \tau$. Furthermore, the collision integral becomes zero when F coincides with Maxwell distribution function.

Therefore, in (2), the collision integral is determined using the following approximate expression (τ -approximation): $St_{ei}\left\{F_e\right\} = -\nu_{ei}\left(F_e - < F_e^0 >\right)$, here the relation is taken onto account $\nu_{ei} \sim 1/\tau_{ei}$. Substituting (2), we obtain:

$$\begin{cases} \hat{L}_2 F_e^{\,0} = v_{ei} < F_e^{\,0(0)} >; & (3) \\ \hat{L}_2 F_e^{\,1} = -\upsilon \dfrac{\partial F_e^{\,0}}{\partial \varepsilon \vec{r}}, & (4) \end{cases}$$

where

$$\hat{L}_2 = \frac{\partial}{\partial t} - \vec{F}_0 \frac{\partial}{\partial \vec{p}} + v_{ei}\,.$$

In the presence of $\vec{B}_0$ a small parameter ε the relation can be determined by $\varepsilon = \left(V_T / \Delta\omega L\right) << 1$, where $\Delta\omega = \left(\omega_0 - \omega_H\right)$ is offset frequency; $\omega_H = eB_0 / m_e c$ is the electron cyclotron frequency, c is the light velocity. Under the condition $\left(\omega_H / \omega_0\right) < \varepsilon$ we have $\Delta\omega \approx \omega_0$. Since $\vec{p}\left(p_x, p_y, p_z\right)$, $\vec{r}\left(r_x, r_y, r_z\right)$ and $\vec{E}\left(E_{0x}, E_{0y}, E_{0z}\right)$ the equations (3) and (4) can be rewritten as:

$$\hat{L}_3 F_e^{\,0} = v_{ei} < F_e^{\,0(0)} >; \quad (3A)$$

$$\hat{L}_3 F_e^{\,1} = -S_1, \quad (4A)$$

where, for simplicity, the following notations were used:

$$\hat{L}_3 = \frac{\partial}{\partial t} - M_1 \frac{\partial}{\partial p_x} - M_2 \frac{\partial}{\partial p_y} - M_3 \frac{\partial}{\partial p_z};$$

$$S_1 = \upsilon_x \frac{\partial F_e^{\,0}}{\partial \varepsilon r_x} - \upsilon_y \frac{\partial F_e^{\,0}}{\partial \varepsilon r_y} - \upsilon_z \frac{\partial F_e^{\,0}}{\partial \varepsilon r_z};$$

$$M_1 = eE_{0x} \sin\omega_0 t + p_y \omega_H;$$

$$M_2 = eE_{0y} \sin\omega_0 t - p_x \omega_H;$$

$$M_3 = eE_{0z} \sin\omega_0 t\,.$$

The approximate solutions to equations (3A) and (4A) can be expressed as:

$$F_e^{\,0} = F_e^{\,0(0)} + F_e^{\,0(1)}; \quad (5)$$

$$F_e^{\,1} = F_e^{\,1(0)} + F_e^{\,1(1)}, \quad (6)$$

where the first terms on the right-hand sides of (5) and (6) are solutions to the homogeneous equations $\hat{L}_3 F_e^{\,0(0)} = 0$ and $\hat{L}_3 F_e^{\,1(0)} = 0$ respectively, expressed by the equality:

$$F_e^{\,0(0)} = F_e^{\,1(0)} = n_e \left(2\pi m_e k T_e\right)^{-3/2} \exp\{-\left(2 m_e k T_e\right)^{-1} [(p_x - \frac{e\omega_0 E_{0x}}{\omega_0^{\,2} - \omega_H^{\,2}} \cos\omega_0 t)^2 +$$

$$+ (p_y - \frac{e\omega_0 E_{0y}}{\omega_0^{\,2} - \omega_H^{\,2}} \cos\omega_0 t)^2 + (p_z - \frac{eE_{0z}}{\omega_0} \cos\omega_0 t)^2 + (\frac{e\omega_H}{\omega_0^{\,2} - \omega_H^{\,2}})^2 \times$$

$$\times (E_{0x}^{\,2} + E_{0y}^{\,2}) \sin^2\omega_0 t + \frac{2e\omega_H}{\omega_0^{\,2} - \omega_H^{\,2}} (p_x E_{0y} - p_y E_{0x}) \sin\omega_0 t + (2 m_e k T_e) v_{ei} t]\}.$$

The functions $F_e^{\,0(1)}$ and $F_e^{\,1(1)}$ in equations (5) and (6) are solutions to the inhomogeneous equation (3A) and (4A). Before finding them, consider the following characteristics of the homogeneous equation (2):

$$\frac{d\vec{p}}{dt} = -\vec{F}_0\,;\ m_e \frac{d\vec{r}}{dt} = \vec{p}\,. \quad (7)$$

The solutions of these characteristic equations relate the values of momentum p_x, p_y, p_z and coordinates r_x, r_y, r_z of electrons at time t to the values P_{0x}, P_{0y}, P_{0z} and R_x, R_y, R_z at the initial time, t' i.e.

$$P_X = P_{0x} \cos\omega_H \left(t - t'\right) - P_{0y} \sin\omega_H \left(t - t'\right) + N_1 e\left(\omega_0 N_2 E_{0x} + N_3 E_{0y}\right);$$

$$P_Y = P_{0x} \sin\omega_H \left(t - t'\right) - P_{0y} \cos\omega_H \left(t - t'\right) + N_1 e\left(\omega_0 N_2 E_{0y} - N_3 E_{0x}\right);$$

$$P_Z = P_{0z} - e\omega_0^{-1}E_{0z}\left\{1-\cos\omega_0\left(t-t'\right)\right\};$$

$$r_X = R_x - \left(m_e\omega_H\right)^{-1}P_{0y}\left\{1-\cos\omega_H\left(t-t'\right)\right\} + \left(m_e\omega_H\right)^{-1}P_{0x}\sin\omega_H\left(t-t'\right) + m_e^{-1}eN_1\left(N_4E_{0y}+N_5E_{0x}\right);$$

$$r_Y = R_y - \left(m_e\omega_H\right)^{-1}P_{0x}\left\{1-\cos\omega_H\left(t-t'\right)\right\} + \left(m_e\omega_H\right)^{-1}P_{0y}\sin\omega_H\left(t-t'\right) + m_e^{-1}eN_1\left(N_5E_{0y}-N_4E_{0x}\right);$$

$$r_Z = R_z + m_e^{-1}P_{0z}\left(t-t'\right) - \left(m_e\omega_0\right)^{-1}eE_{0z}\left\{\left(t-t'\right)-\omega_0^{-1}\sin\omega_0\left(t-t'\right)\right\};$$

$$N_1 = \left(\omega_0^{\,2}-\omega_H^{\,2}\right)^{-1};$$

$$N_2 = \cos\omega_0\left(t-t'\right) - \cos\omega_H\left(t-t'\right);$$

$$N_3 = \omega_0\sin\omega_H\left(t-t'\right) - \omega_H\sin\omega_0\left(t-t'\right);$$

$$N_4 = \omega_0\omega_H^{-1}\left\{1-\cos\omega_H\left(t-t'\right)\right\} - \omega_H\omega_0^{-1}\left\{1-\cos\omega_0\left(t-t'\right)\right\};$$

$$N_5 = \sin\omega_0\left(t-t'\right) - \omega_0\omega_H^{-1}\sin\omega_H\left(t-t'\right).$$

When studying kinetic effects in inhomogeneous plasma, it is required to know the perturbed distribution function of such plasma. One way to find this function is the trajectory integral method, which was first used in problems of oscillations of homogeneous and inhomogeneous plasma in a magnetic field. Transitioning from $\vec{p}$ to $\vec{P}_0$ and as well as from $\vec{r}$ to $\vec{R}$ using the method mentioned above, we determine the desired solutions $F_e^{0(1)}$ and $F_e^{1(1)}$ in the form [17]:

$$F_e^{0(1)} = \int_0^1 \nu_{ei} < F_e^{0(0)}\left(t-t',\varepsilon t,\varepsilon\vec{R},\vec{P}_0\right) > dt'; \tag{8}$$

$$F_e^{1(1)} = -\int_0^1 S_1\left(t-t',\varepsilon t,\varepsilon\vec{R},\vec{P}_0\right)dt'. \tag{9}$$

It should be noted that when integrating the integrand exponential functions in (8) and (9), the conditions were taken into account

$$\frac{eE_{0x}}{P_{0x}} < \Delta\omega; \qquad \frac{eE_{0y}}{P_{0y}} < \Delta\omega; \qquad \frac{eE_{0z}}{P_{0z}} < \Delta\omega,$$

under which these functions were expanded into a series. In this case, only terms were considered $\sim E_0^{\,2}$. Subsequently, by averaging the function F_e the following expressions for the Miller force components are obtained:

$$f_x = \int_{-\infty}^{+\infty} T^{-1}P_{0x} < F_e > d\dot{P}_0 = -N_1^{\,2}n_e\frac{\left(e\omega_0\right)^2}{2m_e}\frac{\partial}{\partial\varepsilon R_x}\left(M_1^{\,0}E_{0x}^{\,2} + M_2^{\,0}E_{0y}^{\,2}\right) - \frac{n_e}{2m_e}\left(\frac{e}{\omega_0}\right)^2\frac{\partial E_{0z}^{\,2}}{\partial\varepsilon R_x}C_1;$$

$$f_y = \int_{-\infty}^{+\infty} T^{-1}P_{0y} < F_e > d\vec{P}_0 = -N_1^{\,2}n_e\frac{\left(e\omega_0\right)^2}{2m_e}\frac{\partial}{\partial\varepsilon R_y}\left(M_1^{\,0}E_{0x}^{\,2} + M_2^{\,0}E_{0y}^{\,2}\right) - \frac{n_e}{2m_e}\left(\frac{e}{\omega_0}\right)^2\frac{\partial E_{0z}^{\,2}}{\partial\varepsilon R_y}C_1;$$

$$f_z = \int_{-\infty}^{+\infty} T^{-1}P_{0z} < F_e > d\vec{P}_0 = -N_1^{\,2}n_e\frac{\left(e\omega_0\right)^2}{2m_e}\frac{\partial}{\partial\varepsilon R_z}\left(M_3^{\,0}\left(E_{0x}^{\,2}+E_{0y}^{\,2}\right)\right) - \frac{n_e}{2m_e}\left(\frac{e}{\omega_0}\right)^2\frac{\partial E_{0z}^{\,2}}{\partial\varepsilon R_z}C_2,$$

here

$$M_1^{\,0} = \frac{3}{2}\cos\left(2\pi\frac{\omega_H}{\omega_0}\right) - \frac{1}{3}\left\{2Q + \pi^{-2}\left(1+\nu_{ei}^{\,2}\left(4\omega_0^{\,2}+\nu_{ei}^{\,2}\right)^{-1}\right)D\sin\left(2\pi\frac{\omega_H}{\omega_0}\right)\right\};$$

$$M_3^{\,0} = \frac{3}{2}\cos\left(2\pi\frac{\omega_H}{\omega_0}\right) - \frac{1}{3}\left\{2Q + \frac{5}{2}\pi^{-2}\left(1+\nu_{ei}^{\,2}\left(4\omega_0^{\,2}+\nu_{ei}^{\,2}\right)^{-1}\right)D\sin\left(2\pi\frac{\omega_H}{\omega_0}\right)\right\};$$

$$M_2^{\,0} = \frac{1}{2} + \cos\left(2\pi\frac{\omega_H}{\omega_0}\right) - \frac{1}{3}\left\{2Q + \frac{1}{2}\pi^{-2}\left(1+\nu_{ei}^{\,2}\left(4\omega_0^{\,2}+\nu_{ei}^{\,2}\right)^{-1}\right)D\sin\left(2\pi\frac{\omega_H}{\omega_0}\right)\right\};$$

$$C_1 = \frac{1}{2}\left(\cos\left(2\pi\frac{\omega_H}{\omega_0}\right)+2\right) - \frac{1}{3}\left\{2Q + \frac{1}{2}\pi^{-2}v_{ei}{}^2\left(4\omega_0{}^2 + v_{ei}{}^2\right)^{-1} D\sin\left(2\pi\frac{\omega_H}{\omega_0}\right)\right\};$$

$$C_2 = \frac{1}{2}\left(\cos\left(2\pi\frac{\omega_H}{\omega_0}\right)+2\right) - \frac{1}{3}\left\{2Q + \frac{3}{2}\pi^{-2}v_{ei}{}^2\left(4\omega_0{}^2 + v_{ei}{}^2\right)^{-1} D\sin\left(2\pi\frac{\omega_H}{\omega_0}\right)\right\};$$

$$Q = \frac{\omega_0}{2\pi}\left[\left(\omega_0 - \omega_H\right)^2 + v_{ei}{}^2\right]^{-1}\left\{v_{ei} - \left[\left(\omega_0 - \omega_H\right)\sin\left(2\pi\frac{\omega_H}{\omega_0}\right) + v_{ei}\cos\left(2\pi\frac{\omega_H}{\omega_0}\right)\right]\left(1-D\right)\right\};$$

$$D = 1 - \exp\left(-2\pi v_{ei}/\omega_0\right).$$

In the absence of a constant magnetic field $\left(\vec{B}_0 \to 0\right)$ or under the condition $\left(\omega_H/\omega_0\right) < \varepsilon$ the following expression for the force is obtained $\vec{f}_M$:

$$\vec{f}_M = -\frac{3}{2}\frac{n_e}{2m_e}\left(\frac{e}{\omega_0}\right)^2 \frac{\partial \vec{E}_0{}^2}{\partial \varepsilon \vec{R}}\left\{1 - \frac{4}{9}\left(\frac{v_{ei}}{\omega_0}\right)^2\right\}. \tag{10}$$

If we neglect collisions $\left(v_{ei} \to 0\right)$, then from (10) we have $\vec{f}_M = -\frac{3}{2} n_e \nabla_{\varepsilon\vec{R}} U_e$, where $\nabla_{\varepsilon\vec{R}}$ is nabla. Thus, an expression for the quasi-potential Miller force has been derived, taking into account for electron-ion collisions. The obtained expression, in the limiting cases $\vec{B}_0 \to 0$ and $v_{ei} \to 0$ coincides with known expression for the high-frequency pressure force up to a coefficient of order unity [18].

Conclusion

An expression for the quasi-potential force in the approximation of fixed ions and a strong external field has been obtained. This expression allows us to estimate the influence of collisions of plasma particles on the Miller force. The force components have been determined for the case when a high-frequency electric field and a stationary magnetic field acting simultaneously on weakly inhomogeneous plasma. Thus, this article introduces a new methodology for determining the expression of the averaged high-frequency pressure force. The approach is based on solving the kinetic equation and the method of successive approximations while observing limiting conditions. The motion of charged particles in an electric field is considered based on the concepts of classical physics, and these concepts retain their validity not only when analyzing the motion of charged particles under the influence of macroscopic external fields but also form the foundation necessary for understanding the processes of particle interaction in plasma — processes involving the microscopic fields of individual particles.

Practical significance of research results. The results of this article can be applied in controlling the spatial distribution of plasma parameters in external fields and in the mathematical modeling of inhomogeneous plasma processes. Furthermore, these results can be applied in the theory of electron motion in high-frequency and constant fields, fluctuations, nonequilibrium processes, the stability of inhomogeneous plasma, and other collective nonlinear phenomena.

References

1 Векслер В.И. О циклическом ускорении частиц в высокочастотных полях / В.И. Векслер, Л.М. Коврижных // Журнал экспериментальной и теоретической физики. — 1958. — Т. 35. — Вып. 5 (11). — С. 1116–1118.

2 Миллер М.А. Движение заряженных частиц в высокочастотных электромагнитных полях / М.А. Миллер // Известия вузов. Серия Радиофизика. — 1958. — Т. 1. — № 3. — С. 110–123.

3 Гапонов А.В. О потенциальных ямах для заряженных частиц в высокочастотном электромагнитном поле / А.В. Гапонов, М.А. Миллер // Журнал экспериментальной и теоретической физики. — 1958. — Т. 34. — Вып. 1. — С. 242–243.

4 Морозов А.И. Движение заряженных частиц в высокочастотном электромагнитном поле / А.И. Морозов, Л.С. Соловьев // Вопросы теории плазмы. — 1963. — Вып. 2. — С. 214–218.

5 Гильденбург В.Б. О нелинейных эффектах в неоднородной плазме / В.Б. Гильденбург // Журнал экспериментальной и теоретической физики. — 1964. — Т. 46. — Вып. 6. — С. 2156–2164.

6 Koshtybayev T. To plasma electrons motion theory in high-frequency fields / T. Koshtybayev, M. Aliyeva // Bulletin of the University of Karaganda — Physics. — 2024. — Vol. 114. — No. 2. — P. 19–26. https://doi.org/10.31489/2024ph2/19-26

7 Koshtybayev T. Correlation functions of weakly inhomogeneous plasma / T. Koshtybayev, M. Aliyeva // Bulletin of the University of Karaganda — Physics. — 2024. — Vol. 115. — No. 3. — P. 6–14. https://doi.org/10.31489/2024ph2/6-14

8 Климонтович Ю.Л. Статистическая теория неравновесных процессов в плазме / Ю.Л. Климонтович. — М.: Изд-во МГУ, 1964. — 281 с.

9 Kosarev I.N. Kinetic theory of plasmas and gases. Interaction of high-intensity laser pulses with plasmas / I.N. Kosarev // Achievements of the physical sciences. — 2006. — Vol. 49. — No. 12. — P. 1239–1252. DOI:10.1070/PU2006v049n12ABEH006027

10 Magee R.M. Direct measurements of the ionization profile in krypton helicon plasmas / R.M. Magee, M.E. Galante, N. Gulbrandsen, D.W. McCarren, E.E. Scime // Physics of Plasmas. — 2012. — Vol. 19. — P. 123506. https://doi.org/10.1063/1.4772060

11 Charles C. An experimental investigation of alternative propellants for the helicon / C. Charles, R.W. Boswell, R. Laine, P. MacLellan // Journal of Physics D: Applied Physics. — 2008. — Vol. 6. — P. 175213. DOI 10.1088/0022-3727/41/17/175213

12 Lafleur T. Detailed plasma potential measurements in a radio-frequency expanding plasma obtained from various electrostatic probes / T. Lafleur, C. Charles, R.W. Boswell // Physics of Plasmas. — 2009. — Vol. 16. — P. 044510. DOI: 10.1063/1.3125314

13 Anisimov I.A. Interaction of a modulated electron beam with an in homogeneous plasma: Two-dimensional electrostatic simulations / I.A. Anisimov, T.E. Litoshenko // Physics of Plasmas. — 2008. — Vol. 34. — No. 10. — P. 847–854. https://doi.org/10.1134/s1063780x0810005x

14 Репин А.Ю. Динамика и взаимодействие с преградой тороидального плазменного сгустка. Ионизационно-динамические характеристики и электромагнитное излучение / А.Ю. Репин, Е.Д. Ступицкий, А.В. Шапранов // Теплофизика высоких температур. — 2004. — Т. 42. — № 4. — С. 523–538. https://doi.org/10.1023/B:HITE.0000039980.35217.cb

15 Lafleur T. Ion beam formation in a very low magnetic field expanding helicon discharge / T. Lafleur, R.W. Boswell, C. Charles // Physics of Plasmas. — 2010. — Vol. 17. — P. 043505. https://doi.org/10.1063/1.3381093

16 Shaihitdinov R.Z. The Mechanism of Attraction of Negatively Charged Macroparticles in Dusty Plasma / R.Z. Shaihitdinov // Low-Temperature Plasma in Functional Coating Processes. — 2014. — Vol. 5. — P. 168–171.

17 Kralkina E.A. Radial inhomogenity of plasma parameters in a low-pressure inductive RF discharge / E.A. Kralkina, P.A. Neklyudova, V.B. Pavlov, K.V. Vavilin, V.P. Tarakanov // Moscow University Physics Bulletin. — 2014. — Vol. 1. — P. 79–89. DOI:10.3103/S0027134914010093

18 Голубков Г.В. Влияние внешнего электрического поля на параметры плазмы нижней ионосферы / Г.В. Голубков, В.Л. Бычков, Н.В. Арделян, К.В. Космачевский, М.Г. Голубков // Химическая физика. — 2019. — Т. 38. — № 7. — С. 23–29. https://doi.org/10.1134/S0207401X19070045

Т. Қоштыбаев, А. Татенов, М. Алиева, К. Жантлеуов

Тұрақты магнит өрісі мен жоғары жиілікті электр өрісінің плазмаға әсері

Мақалада әлсіз біртексіз плазмаға бірмезгілде жоғары жиілікті электр өрісі мен тұрақты магнит өрісі әсер еткен жағдай үшін орташаланған жоғары жиілікті қысым күшін (Миллер күшін) анықтаудың тың тәсілі ұсынылған. Бұл тәсіл электрондардың үлестірім функциясына арналған кинетикалық теңдеуді тізбектестік жуықтау арқылы шешуге негізделген. Аталған жуықтау бойынша баяу қозғалыстар мен қарқынды тербелістер бөлек қарастырылады. Сонымен бірге, есептеулер кезінде теориялық және математикалық физиканың жалпыға белгілі тәсілдері, атап айтқанда сыртқы айнымалы өрістің периоды бойынша орташалау және траектория бойынша интегралдау әдістері де пайдаланылды. Электрондардың қозғалмайтын иондармен соқтығысулары ескерілді. Жоғары жиілікті өрістің амплитудасы уақыт және координата бойынша мардымсыз ғана өзгеретін функция. Шығарып алынған өрнек плазма бөлшектерінің өзара соқтығысулары Миллер күшіне әсерін бағалауға мүмкүндік жасайды және белгілі бір шектеуіш шарттарда бұл өрнек электрондардың жоғары жиілікті өрістердегі қозғалысын сипаттайтын теңдеу арқылы анықталған белгілі өрнекпен сәйкес келеді. Есептеулер кезінде сыртқы электромагниттік өрістің магниттік құраушысы ескерілген жоқ, бұл жағдай жоғары жиілікті электр өрісінің бойлық (қума) екендігін айғақтайды. Аталып өтілген барлық нәтижелер теориялық сипатта болғандықтан оларды жоғары жиілікті электромагниттік өрістердің әсеріндегі біртексіз плазманың кинетикалық теориясын жасау барысында қолдануға болады.

Кілт сөздер: әлсіз біртексіз плазма, плазмалық электрондар, кинетикалық теңдеу, орташаланған күш, электр өрісі, бөлшектердің соқтығысуы, қозғалмайтын иондар, жоғары жиілік.

Т. Коштыбаев, А. Татенов, М. Алиева, К. Жантлеуов

Воздействие постоянного магнитного поля и высокочастотного электрического поля на плазму

В данной работе предложена новая методика определения выражения усредненной силы высокочастотного давления (силы Миллера). Этот метод основан на решении кинетического уравнения для функции распределения электронов и методе последовательных приближений (разделение медленных движений и быстрых осцилляций). Рассматривается случай, когда на слабо неоднородную плазму одновременно действуют электрическое поле высокой частоты и стационарное магнитное поле. В исследовании также применены общеизвестные методы теоретической и математической физики, такие как усреднение по периоду колебания электрического поля и интегрирование по траекториям. Учтены столкновения электронов с неподвижными ионами. Амплитуда электрического поля является медленно меняющейся функцией по времени и по координатам. Полученное выражение позволяет оценить влияние столкновений плазменных частиц на силу Миллера и подтвердить, что при определенных условиях оно совпадает, с точностью до постоянной, с известными выражениями для силы высокочастотного давления, полученными на основе уравнения движения электронов плазмы в высокочастотных полях. Во всех вычислениях пренебрегается вкладом магнитной составляющей электромагнитного поля, что вполне справедливо для продольного электрического поля. Результаты, полученные в данном исследовании, представляют прежде всего теоретический интерес и раскрывают механизмы взаимодействия слабо неоднородной плазмы с высокочастотным электрическим полем. Они также могут быть использованы при построении кинетической теории неоднородной плазмы, находящейся в высокочастотных электромагнитных полях.

Ключевые слова: слабо неоднородная плазма, плазменные электроны, кинетическое уравнение, усредненная сила, электрическое поле, столкновения частиц, неподвижные ионы, высокая частота.

References

1 Veksler, V.I., & Kovrizhnykh, L.M. (1958). O tsiklicheskom uskorenii chastits v vysokochastotnykh polyakh [Cyclical Acceleration of Particles in High-Frequency Fields]. *Zhurnal eksperimentalnoi i teoreticheskoi fiziki — Journal of Experimental and Theoretical Physics, 35, 5*(11), 1116–1118 [in Russian].

2 Miller, M.A. (1958). Dvizhenie zariazhennykh chastits v vysokochastotnykh elektromagnitnykh poliakh [Motion of Charged Particles in High-Frequency Electromagnetic Fields]. *Izvestiia vuzov. Seriia Radiofizika — News of universities. Radiophysics series, 1*(3), 110–123 [in Russian].

3 Gaponov, A.V., & Miller, M.A. (1958). O potentsialnykh yamakh dlia zariazhennykh chastits v vysokochastotnom elektromagnitnom pole [On Potential Wells for Charged Particles in a High-Frequency Electromagnetic Field]. *Zhurnal eksperimentalnoi i teoreticheskoi fiziki — Journal of Experimental and Theoretical Physics, 34, 1*, 242-243 [in Russian].

4 Morozov, A.I., & Solovyev, L.S. (1963). Dvizhenie zariazhennykh chastits v vysokochastotnom elektromagnitnom pole [Motion of Charged Particles in a High-Frequency Electromagnetic Field]. *Voprosy teorii plazmy — Plasma Theory Issues, 2,* 214–218 [in Russian].

5 Gildenburg, V.B. (1964). O nelineinykh effektakh v neodnorodnoi plazme [On nonlinear effects in inhomogeneous plasma]. *Zhurnal eksperimentalnoi i teoreticheskoi fiziki — Journal of Experimental and Theoretical Physics, 46, 6,* 2156–2164 [in Russian].

6 Koshtybayev, T., & Aliyeva, M. (2024). To plasma electrons motion theory in high-frequency fields. *Bulletin of the University of Karaganda — Physics, 114*(2), 19–26. https://doi.org/10.31489/2024ph2/19-26

7 Koshtybayev, T., & Aliyeva, M. (2024). Correlation functions of weakly inhomogeneous plasma. *Bulletin of the University of Karaganda — Physics*, *115*(3), 6–14. https://doi.org/10.31489/2024ph2/6-14

8 Klimontovich, Yu.L. (1964). *Statisticheskaia teoriia neravnovesnykh protsessov v plazme [Statistical theory of nonequilibrium processes in plasma]*. Moscow: Izdatelstvo Moskovskogo Gosudarstvennogo Universiteta [in Russian].

9 Kosarev, I.N. (2006). Kinetic theory of plasmas and gases. Interaction of high-intensity laser pulses with plasmas. *Achievements of the physical sciences*, *49*(12), 1239–1252. DOI:10.1070/PU2006v049n12ABEH006027

10 Magee, R.M., Galante, M.E., Gulbrandsen, N., McCarren, D.W. & Scime, E.E. (2012). Direct measurements of the ionization profile in krypton helicon plasmas. *Physics of Plasmas*, 19, 123506. https://doi.org/10.1063/1.4772060

11 Charles, C., Boswell, R.W., Laine, R., & MacLellan, P. (2008). An experimental investigation of alternative propellants for the helicon. *Journal of Physics D: Applied Physics*, *6,* 175213. DOI 10.1088/0022-3727/41/17/175213

12 Lafleur, T., Charles, C., & Boswell, R.W. (2009). Detailed plasma potential measurements in a radio-frequency expanding plasma obtained from various electrostatic probes. *Physics of Plasmas*, *16*, 044510. DOI: 10.1063/1.3125314

13 Anisimov, I.A., & Litoshenko, T.E. (2008). Interaction of a modulated electron beam with an in homogeneous plasma: Two-dimensional electrostatic simulations. *Physics of Plasmas*, *34*(10), 847–854. https://doi.org/10.1134/s1063780x0810005x

14 Repin, A.Yu., Stupicki, E.L., & Shapranov, A.V. (2004). Dinamika i vzaimodeistvie s pregradoi toroidalnogo plazmennogo sgustka. Ionizatsionno-dinamicheskie kharakteristiki i elektromagnitnoe izluchenie [Dynamics and interaction with the barrier of a toroidal plasma clot. Ionization-dynamic characteristics and electromagnetic radiation]. *Teplofizika vysokikh temperatur — High temperature thermophysics*, *42*(4), 523–538 https://doi.org/10.1023/B:HITE.0000039980.35217.cb [in Russian].

15 Lafleur, T., Boswell R.W., & Charles, C. (2010). Ion beam formation in a very low magnetic field expanding helicon discharge. *Physics of Plasmas*, *17*, 043505. https://doi.org/10.1063/1.3381093

16 Shaihitdinov, R.Z. (2014). The Mechanism of Attraction of Negatively Charged Macroparticles in Dusty Plasma. *Low-Temperature Plasma in Functional Coating Processes*, *5*, 168–171.

17 Kralkina, E.A., Neklyudova, P.A., Pavlov, V.B., Vavilin, K.V., & Tarakanov, V.P. (2014). Radial inhomogenity of plasma parameters in a low-pressure inductive RF discharge. *Moscow University Physics Bulletin, 1*, 79–89. DOI: 10.3103/S0027134914010093.

18 Golubkov, G.V., Bychkov, V.L., Ardeljan, N.V., Kosmachevskij, K.V., & Golubkov, M.G. (2019). Vliianie vneshnego elektricheskogo polia na parametry plazmy nizhnei ionosfery [Influence of external electric field on plasma parameters of the lower ionosphere]. *Khimicheskaia fizika — Chemical Physics*, *38*(7), 23–29 https://doi.org/10.1134/S0207401X19070045 [in Russian].

Information about the authors

Koshtybayev, Talgat (*corresponding author*) — Candidate of physical and mathematical sciences, Associate Professor, Department of Physics, Kazakh National Women's Pedagogical University, Almaty, Kazakhstan; e-mail: koshtybayev70@mail.ru; ORCID ID: https://orcid.org/0009-0004-7344-6801

Tatenov, Adambek — Candidate of physical and mathematical sciences, Associate Professor of the Department of Physics, Kazakh National Women's Pedagogical University, Almaty, Kazakhstan; e-mail: a.tatenov1@gmail.com; ORCID ID: https://orcid.org/0000-0003-4767-5788

Aliyeva, Moldir — Master of sciences, Senior lecturer, Department of Physics, Abai Kazakh National Pedagogical University, Almaty, Kazakhstan; e-mail: moldir-2008@mail.ru; ORCID ID: https://orcid.org/0000-0003-0440-6211

Zhantleuov, Kenzhebek — Candidate of physical and mathematical sciences, Associate Professor of the Department of Mathematics and Mathematical Modelling, Abai Kazakh National Pedagogical University, Almaty, Kazakhstan; e-mail: Kzhantleuov@mail.ru; ORCID ID: https://orcid.org/0009-0001-6658-1165

Article
https://doi.org/10.31489/2025PH1/45-52
UDC 621.315.592, 621.03

Received: 11.11.2024
Accepted: 21.01.2025

E.R. Hasanov[1, 2], Sh.G. Khalilova[2, 1*], R.K. Mustafayeva[1]

[1]*Baku State Uviversity, Baku, Azerbaijan Republic;*
[2]*Institute of Physics, Baku, Azerbaijan Republic*
*(*Corresponding author's e-mail: shahlaganbarova@gmail.com)*

Growing Waves in Semiconductors with Two Energy Minima of the GaAs Type

In two-valley semiconductors of the GaAs type, under the influence of external electric E_0 and magnetic fields H_0 at certain orientations $\vec{E}_0$ and $\vec{H}_0$, a current oscillation with a specific frequency and growth rate was obtained. The orientation of the electric E_0 and magnetic fields H_0 plays a significant role in the excitation of growing waves in semiconductors of the GaAs type. The frequencies and growth increments are determined when exciting current oscillations in a circuit. The dimensions of the crystal are determined by $L_z >> L_x$, L_y, $L_x = L_y$. If the dimensions of the sample differ from the condition $L_z >> L_x$, L_y, $L_x = L_y$, the growing waves can fade or grow. And in this case, the frequencies of the oscillation growth and the value of the electric E_0 and magnetic H_0 fields will be different. The values of the magnetic field in the valley "a" are strong, i.e. $\mu_a H_0 >> c$, and in the valley "b" are weak $\mu_b H_0 >> c$. If the magnetic field values in the valleys "a" and "b" are strong, then electromagnetic waves with other frequencies will also be excited. The theory for other values of the magnetic, electric field and, of course, for other values of the crystal dimensions will show other values for the frequency and growth increment. When preparing semiconductor devices (generators, amplifiers, etc.), the dimensions of the sample play a significant role. In this work, analytical expressions for the electric and magnetic fields for certain sample sizes L_x, L_y, L_z were obtained.

Keywords: unstable waves, fluctuations, Gunn effect, external electric field, semiconductor, magnetic field

Introduction

Among physical effects, one very interesting phenomenon stands out, which was called the Gunn effect, after the English physicist John Gunn, who discovered it in 1963. It is currently accepted that the Gunn effect [1] in n-type GaAs is due to the volumetric negative resistance arising as a result of the induced action of the electron transfer field from the conduction band valley with high carrier mobility to the valley with low mobility, i.e., it is an effect whose existence was previously predicted by Ridley and Watkins [2] and Hilsum [3]. The main confirmation of this mechanism is a decrease in the threshold electric field when the energy gap is placed between the valleys with high and low carrier mobility, caused either by uniform compression [4], or changes in GaP concentration in GaAs-GaP alloys [5]. The various characteristics of the Gunn effect identified by threshold field researchers are consistent with a two-valley mechanism.

Typical current-voltage characteristics for a plate and a notched sample made from the same ingot ($n = 4.6 \cdot 10^{15}$ cm^{-3} and $\mu = 3750$ cm^2/V·s) are presented in the Gunn experiment. In both cases, instability appears or disappears very abruptly, and no hysteresis phenomena were observed with changes in V. The plate characteristic deviates significantly from the ohmic one, apparently due to a decrease μ_L with increasing E. In the case of notched samples, any curvature of the characteristic is masked by the series resistance of the outer regions.

The measured values of the threshold field E_T for plate and notched samples with a thickness of 0.025 cm were almost the same: 2130 ± 100 V/cm for the first and 2440 ± 120 V/cm for the second. This indicates that the instability is primarily a volume effect and is not significantly related to the contacts. However, the consistently slightly lower value for plates suggests that in plate samples, the domains become affected in the high-field region near the cathode. The value of the threshold speeds ϑ_T, determined either by the magnitude E_T or by the threshold current density J_T, is mutually consistent and for the above-mentioned samples they are $9.15 \cdot 10^6$ and $9.24 \cdot 10^6$ cm/s. Such agreement was observed, as a rule, for all samples except those that were shorter than approximately 0.025 cm.

In an ideal homogeneous sample E_T, the value should be equal to E_c, the field corresponding to the maximum velocity ϑ_c. In real samples, inhomogeneities in the distribution of impurities can easily lead to field fluctuations of two to three times, or even more over several microns near the electrodes or within the

bulk. Therefore, a moderate average field can locally reach a value E_c, causing the nucleation of a domain, the movement of which will then be supported in the average field [6]. Thus, the measured values E_T, depending on the degree of field inhomogeneity, can range from E_c to field E_s, requiring a fully formed domain to maintain movement. The instability may be localized in some region of the crystal, although if the extent of this region is too small, the field distribution will be distorted, forming a new stable configuration [7, 8]. In most samples, due to heterogeneity, the value of E_T is lower than the value of E_s. A more interesting mechanism for the occurrence of negative differential resistance in the bulk of a semiconductor was proposed by Ridley and Watkins [2] and independently by Hilsum [3]. These authors drew attention to the fact that in n-type gallium arsenide, which has two minima (or valleys) in its conduction band, the carrier mobility in the upper minimum is much lower than in the lower one. For this reason, during field heating of the electron gas, the electron mobility begins to drop sharply as soon as their energy is sufficient to move to the upper minimum. This leads to the appearance of negative differential resistance. Since the time constant in this case is of the order of 10^{-11} seconds, the negative resistance is maintained up to very high frequencies.

Later, the phenomenon of the occurrence of electrical oscillations associated with the movement of domains in such a semiconductor in a strong electric field was experimentally discovered by Gunn and was called the Gunn effect [9–13]. Many studies have been conducted. Soviet scientists made a significant contribution to the creation of the Gunn effect theory [9–13]. The generation frequency in a Gunn diode is determined by the domain travel time from the formation site to the corresponding contact. Since the domain is usually formed near the cathode, this time is equal to the domain travel time through the sample. The domain velocity is about 10^7 cm/s, so with a sample thickness of 10 microns, the travel time will be about 10^{-10} s, and therefore the generated frequency is about 10^{10} GHz. However, a slightly different generation mechanism is possible that allows obtaining higher-frequency oscillations. This mechanism is not directly related to the domain travel time through the entire sample. Since the domain is not formed instantly, but over a time of about 10^{-10} s, using an external resonator with sufficiently high impedance, it is possible to prevent its complete formation. As soon as the domain begins to form, it immediately becomes an active element of the circuit, capable of delivering power to an external load. If the load is large enough (i.e., high), the voltage on the semiconductor begins to decrease and falls below the threshold value at which the domain can exist. Then the domain begins to dissipate, and the resistance of the semiconductor decreases. At some point, the voltage across it becomes higher than the critical value again, and domain formation begins anew, continuing in this manner. This mode is called the limited space-charge accumulation mode (LSA). The frequency is determined by the characteristics and size of the crystal. Therefore, in this mode, it is much easier to achieve high generation frequencies than in conventional Gunn diodes.

The discovery of the Gunn effect in 1963 stimulated intensive research of this effect in many countries around the world. At the same time, many companies began to develop serial samples of high-frequency oscillation generators based on this effect, and already in 1966, the company “International Semiconductor” (USA) released Gunn generators with a generation frequency of 2–3 GHz and a power in continuous mode of 50–70 mW [9–13].

Essence of Gunn’s effect is that if an electric field is applied to a homogeneous sample made of a special material with existing electrical contacts, the magnitude of which exceeds a certain threshold value (the effect was observed by the discoverer on gallium arsenide and indium phosphide crystals; for the first, the electric field strength should be 3 kV/cm, and for the second — 6 kV/cm), then current oscillations begin to be observed in the external electrical circuit. Moreover, it was discovered that the period of these oscillations is approximately equal to the flight time of electrons from the cathode to the anode, and the oscillation frequency was quite high and was in the microwave range: $T_0 \approx L/u_g$, here: L is the length of the sample; u_g is the drift velocity of electrons [14–16].

Another option for using the Gunn diode is to create high-speed logic circuits and memory elements due to its ability to generate pulses in one period of the operating frequency. The response time of such elements will not exceed several tens of nanoseconds. In addition, the Gunn diode can also be used as a current stabilizer, which is based on the property of its volt-ampere characteristic, which describes the possibility of saturation when certain conditions are reached. That is, in other words, a stabilizer based on it can be used as a means of stabilizing relatively small currents at high frequencies or stabilizing relatively large currents at low frequencies.

The advantages of its operation as a stabilizer are the fast time to establish the stabilization mode and the ability to operate in a very wide range of voltages and currents. Another application of the Gunn diode is the creation of so-called “neuristors”, which are physical devices that imitate an axon — a long process of a nerve fiber coming from a nerve cell.

The transformation of electromagnetic energy using semiconductors is of theoretical and practical interest from the point of view of radio engineering. Therefore, the mechanisms responsible for the occurrence of current oscillations in the image were studied in various experimental and theoretical works. The dependence of the current density (j) on the external electric field E of a GaAs semiconductor has the form.

The characteristic features of the dependence of the current density on the external electric field are that one value of the current density corresponds to several values of the electric field. This characteristic was obtained by Gunn at Mueller values.

In valleys “a” and “b” the effective mass of electrons has the value

$$m_a = 0.072 m_0,\ m_b = 1.2 m_0, \tag{1}$$

(m_0 — mass of a free electron). In GaAs $\Delta = 0.36\,\text{eV}$ based on (1) the mobility of electrons in the corresponding valleys satisfies the condition

$$\mu_a >> \mu_b . \tag{2}$$

In 1963, the English scientist Gunn experimentally [11] discovered in GaAs current oscillations with a frequency of $\omega \sim 10^9$ Hertz at fields $E \sim 3 \cdot 10^3$ V/cm. This effect was called the Gunn effect. Microscopic theories of the Gunn effect are constructed in several theoretical works. However, the frequency of current oscillations in calculations and the critical values of the electric field obtained in these theoretical works correspond to the experimental values approximately. In some theoretical works using the Balsman kinetic equation, the mean free path of charge carriers was calculated, and analytical expressions for the electric field at which current oscillations begin in two-valley semiconductors of the GaAs type were obtained. The conductivities in both zones were also calculated in the presence of an external magnetic field. However, in this theoretical work we calculated the frequencies of current oscillations in two-valley semiconductors taking into account the time of transitions between two valleys, and we will calculate the values of these times depending on the size of the GaAs semiconductor. Current oscillations begin at certain values of external electric and magnetic fields. Theoretical studies of the Gunn effect in an external constant electric and magnetic field have not been investigated. Therefore, the excitation of electromagnetic waves in GaAs semiconductors with constant electric and magnetic fields is of great scientific interest. In this theoretical work, we will calculate the value of the electric and magnetic fields. At the point of the beginning of excitation of electromagnetic waves in GaAs semiconductors. We calculated the critical values of the electric and magnetic fields at the point of excitation of the waves. The values of the electric and magnetic fields are needed to prepare semiconductor devices (generators, amplifiers, etc.) For electric and magnetic fields, we will clean out the analytical expressions at which the current oscillation begins in the semiconductor. The theoretical method for studying the Gunn effect is the solution of the equation of continuity of the current flux density in individual valleys and Maxwell’s equation for alternating electric fields inside the sample.

Main Equations of the Problem

In the Gunn effect experiment in two-valley GaAs semiconductors, the electron concentration n is constant, and therefore,

$$n_a = n_a^0 + n_a', n_b = n_b^0 + n_b'. \tag{3}$$

The transition between the valleys occurs under the condition

$$n_a' = -n_b'. \tag{4}$$

The transition times between the valleys τ_{12} and τ_{21} are determined by the continuity equations

$$\frac{\partial n_a'}{\partial t} + \operatorname{div} j_a' = \frac{n_a'}{\tau_{12}}, \frac{\partial n_b'}{\partial t} + \operatorname{div} j_b' = \frac{n_b'}{\tau_{21}}. \tag{5}$$

Here n_a' — concentration of electrons after transition from one valley to another; n_b' — concentration of electrons after transition from one valley to another; j_a' — current density of electrons after transition from one valley to another; j_b' — current density of electrons after transition from one valley to another.

The current flux densities in the presence of an external magnetic field are determined by the following equations:

$$\vec{j}_a = \sigma_a \vec{E} + \sigma_{1a}\left[\vec{E}\vec{H}\right] + \sigma_{2a}\vec{H}\left[\vec{E}\vec{H}\right];$$
$$\vec{j}_b = \sigma_b \vec{E} + \sigma_{1b}\left[\vec{E}\vec{H}\right] + \sigma_{2b}\vec{H}\left[\vec{E}\vec{H}\right]. \quad (6)$$

In (6) the condition is considered $eE_0 l >> k_0 T$ for the electric field (where e is the elementary charge, E_0 is the electric field, k_0 is the Boltzmann constant, T is the temperature of the sample). Therefore, there are no diffusion terms for the current density.

The magnetic field is determined by Maxwell's equation

$$\frac{\partial \vec{H}}{\partial t} = -\operatorname{crot}\vec{E} \quad (7)$$

.

The electrical conductivities $\sigma_a, \sigma_{1a}, \sigma_{2a}, \sigma_b, \sigma_{1b}, \sigma_{2b}$ are calculated in [17, 18].

Here σ_a — electrical conductivity in valley "*a*"; σ_{1a} — Hall electrical conductivity in valley "*a*"; σ_{2a} — focusing electrical conductivity on valley "*a*"; σ_b — electrical conductivity in valley "*b*"; σ_{1b} — Hall electrical conductivity at valley "*b*"; σ_{2b} — focusing electrical conductivity on valley "*b*".

Theory

By solving the system of equations (5, 6, 7) taking into account (3, 4), we can determine the frequencies of current oscillations in two-valley GaAs semiconductors. For small values of physical quantities $\vec{E}, \vec{H}, n$, i.e. $\vec{E} = \vec{E}_0 + \vec{E}', \vec{H} = \vec{H}_0 + \vec{H}', n = n_0 + n'$, frequencies of current oscillations will be determined.

$$\left(\vec{E}', \vec{H}', n'\right) \sim e^{i\left(\vec{k}\vec{r} - \omega t\right)}. \quad (8)$$

The fluctuation values of the electric and magnetic fields and the concentration of charge carriers when a current appears inside the sample are small compared to the constant thermodynamic values of the electric and magnetic fields and the concentration of carriers.

Selecting a coordinate system

$$\vec{E}_0 = \vec{i}E_{0x}, \vec{H}_0 = \vec{i}H_{0x}.$$

From (6) we easily obtain

$$j'_{ax} = \left(\sigma_a + \sigma_{2a}H_{0x}\right)E'_x - \sigma_{1a}H_{ox}E'_z; \quad (9)$$

$$j'_{ay} = \sigma_a E'_y + \frac{\sigma_{1a}c}{\omega}\left(k_y - k_x\right)E'_y + \sigma_{1a}H_{ox}E'_z + \frac{2\sigma_{2a}cE_{ox}H_{ox}}{\omega}\left(k_z E'_x - k_x E'_z\right); \quad (10)$$

$$j'_{by} = \sigma_b E'_y + \frac{\sigma_{1b}c}{\omega}\left(k_y - k_x\right)E'_y + \sigma_{1b}H_{ox}E'_z + \frac{2\sigma_{2b}cE_{ox}H_{ox}}{\omega}\left(k_z E'_x - k_x E'_z\right). \quad (11)$$

From (6) provided that $\vec{E}_0 = \vec{i}E_{0x}, \vec{H}_0 = \vec{i}H_{0x}$, the corresponding components of the current density in the valleys "*a*" and "*b*" have the form (10, 11), and in the valleys "*b*" the corresponding values (9, 10, 11) have the same form when "*a*" is replaced by "*b*".

In the experiment, the values of current density are measured in different directions. We will write expressions for the fluctuation current density along the *X* axis, equating to zero (10, 11) we find E'_y and E'_z, and substituting into (9)

$$j'_{ax} = \left(\sigma_a + \sigma_{2a}H_{0x} + \frac{\sigma^a_{1y}\sigma^a_z - \sigma^a_1\sigma^a_{1z}}{\sigma^a_{1y}\sigma^a_{2z} - \sigma^a_{2y}\sigma^a_{1z}}\right)E'_x;$$
$$j'_{bx} = \left(\sigma_b + \sigma_{2b}H_{0x} + \frac{\sigma^b_{1y}\sigma^b_z - \sigma^b_{1z}\sigma^b_1}{\sigma^b_{1y}\sigma^b_{2z} - \sigma^b_{2y}\sigma^b_{1z}}\right)E'_x. \quad (12)$$

The current densities along the *X* and *Z* axes, of course, have certain values, following the experiment, we consider them equal to zero, i.e. $j_x = j_y = 0$. Therefore, the values of the corresponding electrical conductivity have the following form

$$\sigma_{1y}^{a,b}=\sigma_{a,b}+\frac{\sigma_{1a,b}c}{\omega}\left(k_y-k_x\right),\sigma_{ya,b}=\frac{2\sigma_{2a,b}cE_{ox}}{\omega H_{0x}}k_z;$$
$$\sigma_{2y}^{a,b}=\sigma_{1,a,b}k_x-\frac{2\sigma_{2a,b}E_{ox}c}{\omega H_{0x}}k_x,\sigma_{za,b}=\frac{\sigma_{1a,b}ck_zE_{ox}}{\omega H_{0x}}-\frac{2\sigma_{2a,b}cE_{ox}}{\omega H_{0x}}k_y,$$
$$\sigma_{1z,a,b}^{a,b}=\frac{2\sigma_{2a,b}E_{ox}c}{\omega H_{0x}}k_x+\sigma_{1,a,b},\sigma_{2za,b}=\sigma_{a,b}-\frac{\sigma_{1a,b}ck_xE_{ox}}{\omega H_{0x}}-\frac{2\sigma_{2a,b}cE_{ox}}{\omega H_{0x}}k_y. \quad (13)$$

From (5) we obtain

$$\left(1-i\omega\tau_{21}\right)\operatorname{div}j'_{ax}=\left(1+i\omega\tau_{12}\right)\operatorname{div}j'_{bx}. \quad (14)$$

Considering, $\mu_aH_{ox}>c$ and $\mu_bH_{ox}<c$, and choosing the dimensions of the sample

$$L_x=L_y,L_z>>L_x,L_y \quad (15)$$

the dispersion equation under the above conditions (15) have the following form:

$$\tau_{21}\frac{\mu_a}{\mu_b}\phi_a^3\omega^4+\left(i\frac{\mu_a}{\mu_b}\phi_a^3-10\tau_{12}\omega_x\phi_a^3-3\tau_{12}\omega_x\phi_a^2\right)\omega^3-\left(i6\phi_a^2\frac{\mu_b}{\mu_a}+3\tau_{21}\omega_x\phi_a^2\frac{\mu_a}{\mu_b}+\right.$$
$$+4\tau_{21}\omega_x\phi_a^2\frac{\mu_b}{\mu_a}-i3\phi_a^2+\tau_{12}\omega_x\phi_a^2\frac{4\mu_b}{\mu_a}+\tau_{21}\omega_x\phi_a\frac{12\mu_a}{\mu_b}-i3\phi_a+\tau_{12}\omega_x\phi_a^2\frac{18\mu_b}{\mu_a}\Big)\omega_x\omega^2+$$
$$+\left(i\phi_a^34-3\tau_{21}\omega_x\phi_a-i32\phi_a\frac{\mu_b^2}{\mu_a^2}-24\tau_{12}\omega_x\phi_a^2\frac{\mu_b}{\mu_a}-i2\frac{\mu_a}{\mu_b}\phi_a^2+\tau_{21}\omega_x\frac{24\mu_a}{\mu_b}-\right.$$
$$\left.-4i_x\phi_a^2\frac{\mu_b}{\mu_a}-12\tau_{12}\omega_x\phi_a^2\right)\omega_x^2\omega-8\tau_{21}\omega_x^4\phi_a^3\frac{\mu_a}{\mu_b}-i\left(\frac{\mu_a}{\mu_b}\phi_a^348-12\phi_a^3\frac{\mu_b}{\mu_a}\right)12\phi_a^3\frac{\mu_a}{\mu_b}=0 \quad (16)$$

Here $\phi_a=\frac{\mu_aH_{ox}}{c}$, $\omega_x=ck_x$.

We can estimate the values of the magnetic and electric fields using the formula

$$E_0=2H_0\frac{\mu_b}{\mu_a},\ H_0=\sqrt{\frac{2}{3}}\frac{c}{\sqrt{\mu_a\mu_b}}; \quad (17)$$
$$\mu_a=10^5,\mu_в=10^4,\ x=\frac{\omega}{\omega_x}.$$

Then the fourth-order dispersion equation with respect to the frequencies of current oscillations has the following algebraic form

$$x^4+\left(\frac{i}{\tau_{21}\omega_x}-\frac{9\tau_{12}}{\tau_{21}}\right)x^3+\left[\frac{6}{\tau_{21}\omega_x}\left(\frac{\mu_b}{\mu_a}\right)^3-i\frac{3}{\phi_a}\frac{\mu_b}{\mu_a}+\frac{4\tau_{12}}{\tau_{21}\phi_a}+12\left(\frac{\mu_b}{\mu_a}\right)^2+\frac{2\tau_{12}}{\tau_{21}}\frac{\mu_b}{\mu_a}\right]x^2+$$
$$+\left[24-12\frac{\tau_{12}}{\tau_{21}}\left(\frac{\mu_b}{\mu_a}\right)^2\right]x-8\tau_{21}\omega_x-i48=0 \quad (18)$$

The solution of this equation in the general case (i.e. without assumption is not possible). Therefore, we will use the conditions and from (18)

we obtain

$$x^4-15x_0x_1-\frac{9\tau_{12}\omega_x}{5}x_0^3+\left(\frac{20\tau_{12}\omega_x}{\phi_a}+12\frac{\mu_b^2}{\mu_a^2}\right)x_0^2+\left(24+60\tau_{12}\omega_x\frac{\mu_b^2}{\mu_a^2}\right)x_0+\frac{2\mu_b}{\mu_a}x_1-\frac{8}{5}=0; \quad (19)$$

$$4x_0^3x_1+5x_0^3-\frac{27\tau_{12}\omega_x}{5}x_0^2x_1+2\left(\frac{20\tau_{12}\omega_x}{\phi_a}+12\frac{\mu_b^2}{\mu_a^2}\right)x_0x_1+\left(24+60\tau_{12}\omega_x\frac{\mu_b^2}{\mu_a^2}\right)x_1-\frac{2\mu_b}{\mu_a}x_0-48=0. \quad (20)$$

Then after isolating the real and imaginary parts of equation (18), we obtain the following two equations (19-20). When obtaining (19-20), we assumed for the transition times from valley "*b*" to valley "*a*" from the condition

$$\tau_{21}\omega_x = 5. \quad (21)$$

From the joint (19-20) the real and imaginary parts of the frequency oscillation are obtained as follows

$$x_0 = \frac{9}{5}\tau_{12}\omega_x. \quad (22)$$

Substituting (22) into (20), we easily obtain:

$$x_1 = \frac{3}{20}\tau_{12}\omega_x. \quad (23)$$

The ratio $\frac{x_1}{x_0} << 1$, this follows explicitly $\sigma_{12} << \sigma_{21}$.

Comparing (22) and (23), we obtain

$$\frac{\tau_{12}}{\tau_{21}} = \left(\frac{2}{27}\right)^{1/3}\frac{1}{2} << 1.$$

And this indicates that the transition time from valley "*a*" to valley "*b*" is less than the transition time from valley "*b*" to valley "*a*".

Thus, the frequency of current oscillations

$$\omega_0 = \frac{9}{5}\tau_{12}\omega_x^2,$$

the frequency of increase

$$\omega_1 = \frac{3}{20}\tau_{12}\omega_x^2.$$

With another value of the solution τ_{21}, the frequency and the increment of increase will have a completely different value.

Discussion

Thus, the conditions for excitation of increasing waves in two-valley semiconductors depend significantly on the choice of coordinate systems relative to external electric and magnetic fields. Of course, these conditions depend on the size of the sample. The obtained analytical formulas for the electric and magnetic fields correspond to the Gunn experiment. The time of transition from the second valley to the first valley $\tau_{21} = \frac{1}{5\omega_x} = \frac{1}{5ck_x} = \frac{L_x}{10c\pi}$ for $\tau_{21} \sim 10$. The characteristic time of transition from "*a*" to "*b*" and from "*b*" to "*a*" in addition to the specified values, other values can be obtained. However, the condition $\tau_{21} \sim \tau_{12}$ is not violated when obtaining current oscillations in the specified semiconductors. The orientation of the electric and magnetic fields plays a role in obtaining the corresponding oscillations. Of course, from all possible orientations, it is necessary to choose the orientation for which the required value is less than the value of the external electric field. This means that the direction of the magnetic and electric fields coincides and is directed along the electric field and the excitation of current oscillations occurs as in the Gunn experiment. To reduce the electric field, it is necessary to check other orientations $\vec{E}_0$ and $\vec{H}_0$. For the preparation of corresponding devices based on GaAs type semiconductors, it is practically advantageous at lower values of the external electric field.

Results

Analytical formulas for the purity of excited waves and for the growth increment of these waves are obtained. The dependence of the frequency and the growth increment of the growing wave on the external electric and magnetic fields is not the only one for obtaining a growing wave in the specified semiconductors. The obtained forms for the electric and magnetic fields are quite consistent with the Gunn experiment. The experimental data of the Gunn effect for the electric field are in good agreement with our theoretical studies for the electric field. However, there are no experimental values of the magnetic field and therefore the values of the magnetic field obtained by us theoretically were not compared with the experimental data. Numerical estimates of the transition times from valley "*a*" to valley "*b*" are of the order of the electron relaxation time. The value of the transition time from valley "*a*" to valley "*b*" and back, depending on the value of the external electric and magnetic fields may be different. However, in all cases, the transition time from valley

"*b*" to valley "*a*" is greater than the transition time from valley "*a*" to valley "*b*", i.e. $\tau_{21} > \tau_{12}$. This condition proves that the charge carriers (in this case, electrons) are scattered by the crystal lattice, lose energy and pass from the outer energy valley to the lower valley. There are no theoretical studies of the Gunn effect in alternating electric and magnetic fields. For such a theoretical analysis, it is necessary to solve nonlinear differential equations, for example, using the mathematical method of Bogolyubov-Metropolsky [18, 19, 20]. Such a study of the Gunn effect leads to the determination of the amplitude of the current oscillation, and, of course, to determine the amplitude of the emerging waves as a function of time.

The obtained analytical expressions of the electric and magnetic fields for certain sample sizes can be used in the preparation of semiconductor devices (generators, amplifiers, etc.).

References

1 Gunn, J.B. & Elliott, B.J. (1966). Measurement of the negative differential mobility of electron in GaAs, *Physics Letters, 22*, 369–3711.

2 Ridley, B.K. & Watkins, T.B. (1961). The Possibility of Negative Resistance Effects in Semiconductors. *Proc. Phys. Soc. 7*8, 17–36.

3 Hilsum, C. (1962). Transferred Electron Amplifiers and Oscillators. *Proceedings of the IRE, 50*, 2, 185–189.

4 Hutson, A.R., Jarayaman, A., Chynoweth, A.G., Corriell, A.S., & Feldmann, W.L. (1965). Mechanism of the Gunn Effect from a Pressure Experiment. *Phys. Rew. Letters, 14*, 639.

5 Shyam, M., Allen, L.W., & Pearson, G.L. (1966). Effect of variation of energy minima separation on Gunn oscillations. *IEEE Trans.*, *ED-13*, 63.

6 Heeks, L.S., Woode, A.D., & Sandbank, C.P. (1965). Wave propagation in negative resistance media. *Proc IEEE, 53*, 554.

7 McCumber, D.E. & Chynoweth, A.G. (1966). Hall effect in many-valley semiconductors at high electric field. *IEEE Trans., ED-13*, 4.

8 Kroemer, H. (1966). Hot-electron relaxation effects in devices. *IEEE Trans., ED-13*, 27.

9 Gunn, J.B. (1964). Current instabilities and potential distribution in GaAs and InP. *Plasma Effects in Solids*, 199–207.

10 Kozhevnikov, V.Y., Kozyrev, A.V., Konev V.Y., & Klimov A.I. (2022). The phase stability of nanosecond Gunn oscillators. *Vojnotehnicki glasnik — Military Technical Courier, 70*(2), 460–471.

11 Gunn, J.B. (1963). Microwave oscillations of current in a GaAs semiconductor. *Solid state comm, 1*, 88.

12 Ridley, B.K. (1966). The inhibition of negative resistance dipole waves and domains in n-GaAs. *IEEE Trans ED-13*, 41.

13 Pejman Taslimi (2005). An introduction to Gunn oscillator and electronics of TEDs, Shahed university of Tehran, 12.

14 Kalyon, G., Mutlu, S., Kuruoglu, F., Pertikel, I., Demir, I., & Erol, A. (2023). In GaAs-based Gunn light emitting diode. *Materials Science in Semiconductor Processing, 159*, 1, 107389.

15 Hua-Wei Hsu, Michael J. Dominguez, & Vanessa Si. H. (2020). Gunn threshold voltage characterization in GaAs devices with wedge-shaped tapering. *J. Appl. Phys., 128*, 074502.

16 Hasanov, E.R., Khalilova, Sh.G., Mammadova, G.M., & Mansurova, E.O. (2023). Excitation Of Unstable Waves In Semiconductors Such As Gaas Magnetic Fields. *JTPE, 15*, 2, 302–306.

17 Hasanov, E.R, Khalilova, Sh.G., & Mustafayeva, R.K. (2021). Instability in Two GaAs Valley Semiconductors in Electric and Magnetic Fields. *The 17th International Conference on "Technical and Physical Problems of Engineering"*, 60–63.

18 Bogolyubov, N.N., & Mitropolsky, Yu.A. (1955). Asymptotic methods in the theory of nonlinear oscillations Engineering, *Physics*, 408.

19 Richard, Krantz. (1990). Threshold Voltage and IV Characteristics of AlGaAs/GaAs MODFETs. Electronics Research Laboratory Laboratory Operations The Aerospace Corporation, 20.

20 Hasanov, E.R, Khalilova, Sh.G., & Mustafayeva, R.K. (2022). Instability in two GaAs valley Semiconductors in electric and magnetic fields. *International Journal on "Technical and Physical Problems of Engineering" IJTPE 14*(1), 228–232.

Э.Р. Гасанов, Ш.Г. Халилова, Р.К. Мустафаева

GaAs типті екі энергия минимумы бар жартылай өткізгіштердегі өсіп келе жатқан толқындар

$\vec{E}_0$ сыртқы электрлік және H_0 магнит өрістерінің әсерінен GaAs типті екі жолақты жартылай өткізгіштерде белгілі бір бағыттар бойынша $\vec{E}_0$ және H_0 токтың тербелісі белгілі бір жиілікте және

өсу қарқынымен алынады. $\vec{E}_0$ электрлік және H_0 магнит өрістерінің бағыты GaAs типті жартылай өткізгіштердегі өсу толқындарын қоздыру кезінде маңызды рөл атқарады. Электрлік және магниттік өрістердің мәндерін анықтау үшін аналитикалық өрнектер алынды. Тізбектегі токтың тербелісі қозған кезде өсу жиіліктері мен өсінділері анықталады. $L_z >> L_x$, L_y, $L_x = L_y$ кристалдың өлшемдері айқындалды. Егер үлгінің өлшемдері $L_z >> L_x$, L_y, $L_x = L_y$ жағдайдан өзгеше болса, толқындардың өсуі әлсіреуі немесе өсуі мүмкін. Бұл ретте тербелістің өсу жиілігі мен $\vec{E}_0$ электрлік және H_0 магнит өрістерінің мәндерін басқалар алады. Алқаптағы магнит өрісінің мәндері «*a*» күшті, яғни $\mu_a H_0 >> c$, «*b*» алқабында әлсіз, яғни $\mu_b H_0 >> c$. Егер «*a*» және «*b*» алқаптарындағы магнит өрісінің мәні күшті болса, онда электромагниттік толқындар басқа жиіліктермен де қозғалады. Магниттік, электр өрісінің және кристалл өлшемдерінің басқа мәндеріндегі теория жиілік пен өсу үшін басқа мәндерді көрсетеді. Жартылай өткізгіш құрылғыларды (генераторлар, күшейткіштер және т.б.) дайындау кезінде үлгінің өлшемдері маңызды рөл атқарады. Бұл жұмыста үлгілердің белгілі бір өлшемдерінде L_x, L_y, L_z электр және магнит өрісінің аналитикалық өрнектері алынды.

Кілт сөздер: тұрақты емес толқындар, флуктуациялар, Ганн эффектісі, сыртқы электрлік өрістер, жартылай өткізгіштік, магнит өрістер

Э.Р. Гасанов, Ш.Г. Халилова, Р.К. Мустафаева

Нарастающие волны в полупроводниках с двумя минимумами энергии типа GaAs

В двухдолинных полупроводниках типа GaAs под влиянием внешнего электрического $\vec{E}_0$ и магнитного H_0 полей при определённых ориентациях $\vec{E}_0$ и H_0 получено колебание тока с определённой частотой и инкрементом нарастания. Ориентация электрического $\vec{E}_0$ и магнитного H_0 полей играет существенную роль при процессе возбуждения нарастающих волн в полупроводниках типа GaAs. Получены аналитические выражения для определения значений электрического и магнитного полей. Определены частоты и инкременты нарастания при возбуждении колебаний тока в цепи. Размеры кристалла определяются $L_z >> L_x$, L_y, $L_x = L_y$. Если размеры образца отличаются от условия $L_z >> L_x$, L_y, $L_x = L_y$, то нарастая, волны могут затухать или нарастать. При этом частоты нарастания колебания, а также значения электрического $\vec{E}_0$ и магнитного H_0 полей будут получаться другими. Значения магнитного поля в долине «*a*» является сильным, т.е. $\mu_a H_0 >> c$, а в долине «*b*» является слабым $\mu_b H_0 >> c$. Если значение магнитного поля в долинах «*a*» и «*b*» становится сильным, тогда возникают электромагнитные волны с другими частотами. Теория при других значениях магнитного, электрического поля и размеров кристалла покажет другие показатели для частоты и инкремента нарастания. При приготовлении полупроводниковых приборов (генераторов, усилителей и т.д.) существенную роль играют размеры образца. В данной работе были получены аналитические выражения электрического и магнитного поля при определенных размерах образцах L_x, L_y, L_z.

Ключевые слова: нестабильные волны, флуктуации, эффект Ганна, внешнее электрическое поле, полупроводник, магнитное поле

Information about the authors

Hasanov, Eldar — PhD, Associate Professor, Department of Solid State Physics, Baku State University, Leader of Department of Encyclopedia and Terminology, Institute of Physics, Baku, Azerbaijan; e-mail: egasanov065@gmail.com; ORCID ID: https://orcid.org/0009-0009-6900-6148

Khalilova, Shahla (*corresponding author*) — PhD, Leading Researcher of Department of Encyclopedia and Terminology, Institute of Physics, Teacher of Department of Structure of Matter, Baku State University Physics, Baku, Azerbaijan; e-mail: shahlaganbarova@gmail.com; ORCID ID: https://orcid.org/0000-0003-4302-9674

Mustafayeva, Ruhiyya — PhD, Teacher, Department of Solid State Physics, Baku State University Physics, Baku, Azerbaijan; e-mail: ruhi-qrk@mail.ru; ORCID ID: https://orcid.org/0009-0005-2342-5399

Article
https://doi.org/10.31489/2025PH1/53-59
UDC 625.87

Received: 17.11.2024
Accepted: 27.01.2025

D.N. Kakimzhanov[1*], Z.A. Satbayeva[1, 2], M.K. Dautbekov[1],
Y.S. Turabekov[1], R.M. Kuanyshbay[1], A.S. Rustemov[1]

[1]PlasmaScience LLP, Ust-Kamenogorsk, Kazakhstan;
[2]Shakarim University, Semey, Kazakhstan;
[3]D. Serikbayev East Kazakhstan Technical University, Ust-Kamenogorsk, Kazakhstan
*(*Corresponding author's e-mail: d.kakimzhanov19@gmail.com)*

Influence of Spaying Parameters on the Property of Detonation Coatings Based on Ta

This paper investigates the influence of sputtering parameters on the properties of tantalum-based detonation coatings. One of the key parameters in sputtering is the volume of barrel filling, which affects the properties of the resulting coatings. Tantalum coatings were produced at various levels of barrel filling with explosive gas, specifically at 50–70% fill levels. The results demonstrated that the roughness of the coatings decreases as the barrel fill volume increases, leading to coatings with a more homogeneous structure. Additionally, the tests revealed that coatings produced at 60% fill exhibited superior corrosion resistance compared to the other samples. Based on these findings, the optimal barrel fill level for explosive gas was determined.

Keywords: detonation spraying, hardness, tantalum, corrosion, structure, coating, tribology

Introduction

Modern industries such as power generation, aviation, aerospace and medical technology are faced with the need to protect equipment from severe wear and corrosion. Various methods of spraying protective coatings are used to increase the durability of equipment and prevent its premature destruction [1–4].

Tantalum-based coatings have unique properties that allow them to withstand very high temperatures without losing their mechanical properties [5]. This makes it particularly valuable in industries such as aerospace, energy and chemicals, where materials are often subjected to extreme temperature conditions. For example, in the aerospace industry, tantalum is used in the production of parts for rockets and airplanes, where high strength and resistance to heat are required [6–8]. In addition, tantalum is characterized by high corrosion resistance, which allows it to retain its properties even in aggressive chemical environments. Tantalum-based coatings also demonstrate exceptional resistance to thermal cycling, which allows them to retain their characteristics even under abrupt temperature changes. Various sputtering methods are used to produce tantalum (Ta) coatings. The most efficient and advanced method is powder detonation sputtering, which has a number of important advantages over other sputtering technologies such as plasma or arc sputtering [9–11]. The main advantage of the detonation method is the very low porosity of the coating, which ensures high corrosion resistance even in the most aggressive environments. In addition, due to the high speed and energy of the process, detonation spraying produces coatings with high adhesion to the base material, which allows them to retain their properties even under intense mechanical and thermal stresses [12]. Unlike plasma spraying, which is often characterized by high porosity and requires sophisticated equipment for process control, detonation spraying produces coatings with a dense structure and fewer internal defects. This makes it the

preferred choice for protecting highly loaded parts such as turbine blades and power heat exchangers. Also in aviation and aerospace, this method can protect critical structural components from the damaging effects of extreme temperatures and pressures, making it indispensable for these industries [13].

The parameters of detonation sputtering (DS) significantly affect the properties of the resulting tantalum coating [14]. One of the important parameters of sputtering is the filling of the barrel with gas mixture. In this connection, the aim of this work is to study tantalum coatings obtained at different degrees of barrel filling.

Materials, equipment and methods of experiments

Heat-resistant low-alloy steel 12Kh1MF (equivalent to 14MoB63) was chosen as the substrate. The specimens were ground to obtain an even and smooth surface. After grinding, the specimens were sandblasted. Ta spherical shaped powder with size 15–45 μm was used for sputtering (Fig. 1). Detonation atomization was carried out using a CCDS2000 unit. The modes were alternated depending on the barrel filling volume (Table). The barrel is filled with gases through a high-precision gas distribution system controlled by a computer. The process begins by filling the barrel with carrier gas.

Table

Spray mode of detonation spraying

Sample	Fuel / oxide ratio littler	Stem fill volume, %	Spray distance, mm	Number of shots
1	1.026	50	150	15
2	1.026	60	150	15
3	1.026	70	150	15

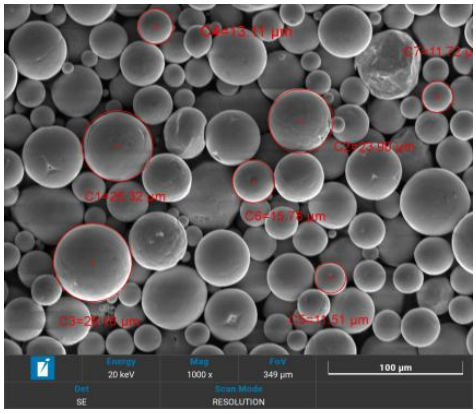

Figure 1. Image of Ta powder

A Tescan Vega 4 scanning electron microscope was used to analyze the powder morphology and coating structure.

Microhardness measurement was carried out on a METALAB 502 device in accordance with GOST 9450-76. Also tribological tests were carried out on tribometer TRB3 on the basis of standard method (international standards ASTM G99), based on the scheme “ball disk” (Fig. 2). Sample rotation speed — 3 cm/s, load 10 N, a steel ball 100Cr6 with a diameter of 6 mm was used as a counterweight.

Corrosion resistance was studied on a CS300-galvanostat potentiostat. It was tested at room temperature (25 °C) in a 3.5 % NaCl solution over an area of 1 cm^2. A three-electrode cell system was used in the experiment, in which a silver chloride electrode served as a comparison electrode and a platinum electrode served as an auxiliary electrode. Before each polarization experiment, the sample was exposed to the electrolyte by immersion in water for 60 min until a stable open circuit potential (PRC) state was found. The corrosion potential and current density were obtained from the polarization curves by Tafel extrapolation for the four samples.The potential was scanned from −0.1 to 0.1 in relative to OCP, and the scan rate was 0.5 mV/s. The tests were repeated three times for each sample, and the results were analyzed using CS Studio 6.

Results and discussion

Figure 2 shows the results of the coating surface roughness measurement. The measurement results showed that all coatings are characterized by moderate roughness. At 50 % of barrel filling the coating has

the highest roughness (Ra = 4.26 μm) this is probably due to the fact that the reduction of particle energy leads to the formation of protrusions and defects on the coating. When the barrel is filled to 60 % the roughness decreases compared to 50 %, indicating a more uniform distribution of material. The lowest value of roughness among all samples has a coating obtained at 70 % filling of the barrel, because the decrease in particle energy leads to complete melting of particles, which reduces the roughness.

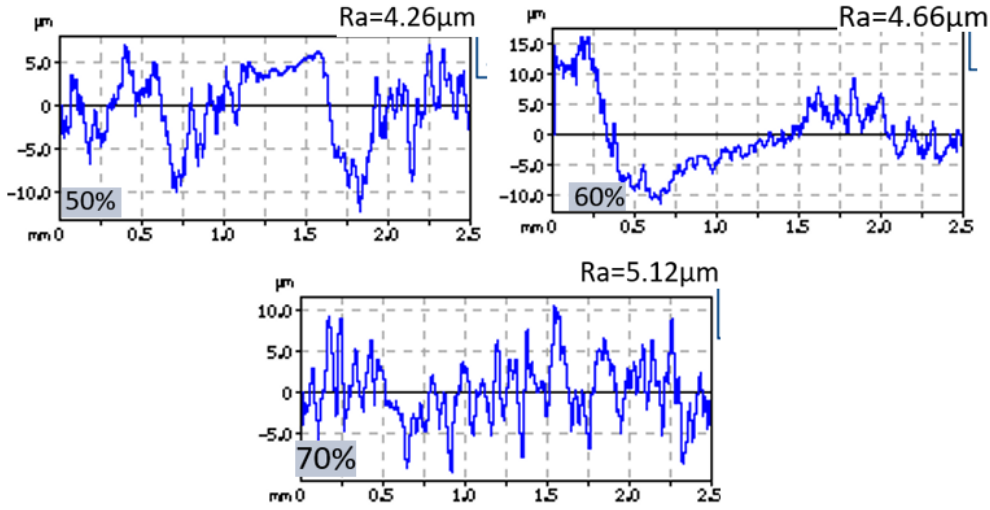

Figure 2. Results of roughness measurement

The corrosion resistance of tantalum-based coatings obtained with different barrel fillings was evaluated by testing with an open area of 1 cm^2 at room temperature (25 °C) in 3.5 wt% NaCl solution. The potentiodynamic polarization curves of the three types of coatings applied by detonation sputtering are shown in Figure 3. To obtain the electrochemical parameters, the Tafel area of both cathodic and anodic branches was extrapolated, and the point of intersection of these two lines was used to determine the corrosion current density (I_{corr}) and corrosion potential (E_{corr}).

The presented Tafel diagram (Fig. 2) shows the polarization dependences for coatings obtained at different degrees of filling of the detonation sputtering barrel: 50 %, 60 % and 70 %. In the region of positive potential displacements (relative to the corrosion potential) there is an increase in the current density, which is associated with the anodic dissolution of the coating material. The slope of the anodic branch varies with the degree of filling, indicating different rates of anodic processes. The corrosion potential shifts to a more negative side with increasing trunk filling degree: For 60 %: a more noble potential (E_{corr}) indicates better corrosion resistance.

For 50 % and 70 %: the potentials shift towards active values, indicating a decrease in the corrosion resistance of the coating.

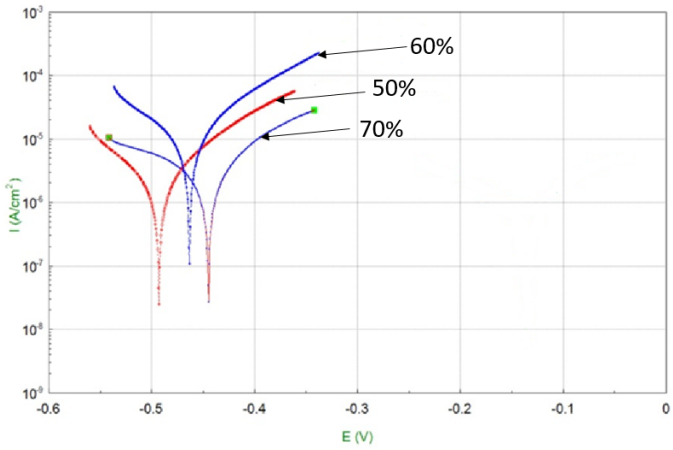

Figure 3. Corrosion test results

Figure 4 shows the cross-sectional morphology of the coatings obtained with varying barrel fill. The results of the study show that all coatings have a characteristic structure for detonation coatings. All coatings are tightly adhered to the substrate without any cracks and failures and no signs of delamination were observed. When filling the barrel, the coating has visible inhomogeneity, which may be due to insufficient particle energy during sputtering. And when the barrel is filled, the coating shows a more even surface and significantly lower porosity compared to 50 % and 70 %.When the barrel is filled to 70 %, the top layer again becomes less even, cracks and defects are observed, probably related to excessive particle energy.

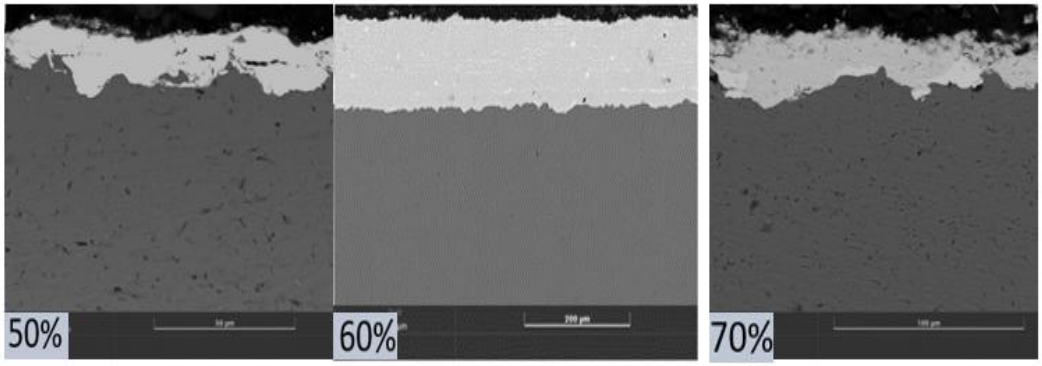

Figure 4. SEM images of cross-sectional morphology of tantalum coatings obtained with varying barrel fill

Figure 5 shows the dependence of coating hardness on the degree of barrel filling. Coatings obtained at 70 % of filling have low hardness compared to the rest of the samples. This is probably due to the formation of cracks or internal stresses due to excessive particle energy, which worsens the mechanical properties. At 60 % barrel filling the coating gives the best result in terms of coating hardness, which confirms the most favorable conditions for the formation of dense and defects of minimal structure.

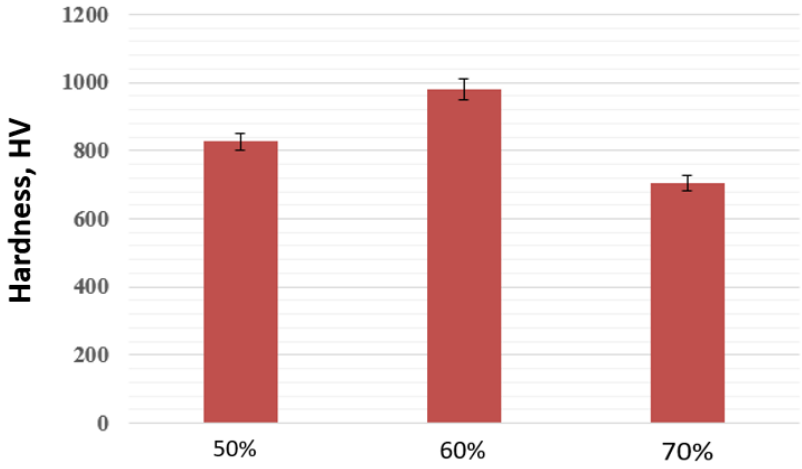

Figure 5. Graph of coating hardness distribution

The tribological study was carried out using the ball-disk method. Figure 6 shows a graph showing the results of the study of the wear volume and wear coefficient of the coating obtained at different fillings of the barrel. The results of the study showed that at 50 % fill rate the wear volume and wear coefficient are relatively low. This may be due to insufficient particle energy during sputtering, which leads to the formation of defects in which reduces the wear resistance of coatings. With the increase in filling percentage, we observe an increase in wear volume and wear coefficient, which may be due to the improvement in coating properties such as adhesion and coating density. Perhaps the coating at 60 % fill rate becomes denser and more resistant to stress, which improves its wear resistance. At 70 % fill rate, the highest volume and wear coefficient is observed which is probably due to excess particle energy.

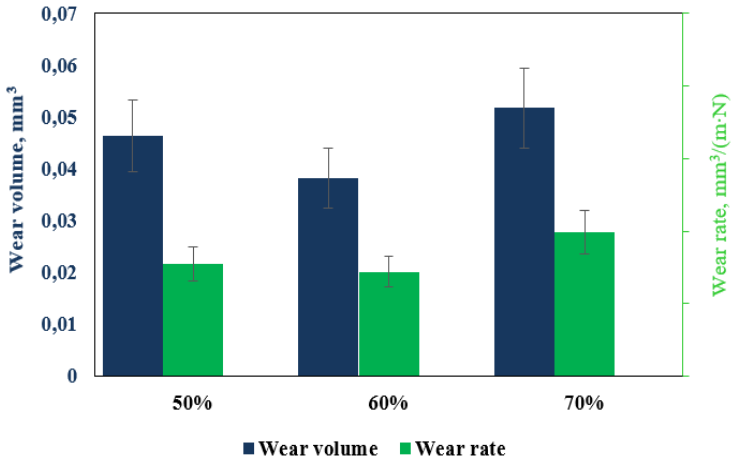

Figure 6. Graph of wear volume dependence on the degree of barrel filling

Conclusion

According to the evaluation and analysis of all the results obtained, the following main conclusions can be drawn on the present research work:

It was found that an increase in the volume of barrel filling leads to a decrease in the surface roughness value.

It has been established that at various degrees of barrel filling at detonation spraying coatings provide an increase in strength properties and hardness of the matrix without significant degradation of the surface.

The highest wear volume and wear rate are observed at a 70% fill rate, which may be attributed to the increased density of the coating, making it less elastic and more susceptible to microcracks and mechanical damage.

The results of coating hardness tests showed at optimum spraying mode the hardness increases from 742 HV to 986 HV

It has been established that detonation coating technologies provide, under optimal modes, the formation of wear-resistant and corrosion-resistant tantalum-based coatings.

Acknowledgments

This research has been funded by the Science Committee of the Ministry of Science and Higher Education of the Republic of Kazakhstan (Grant No. BR24992870).

References

1 Dudina, D.V., Batraev, I.S., Ulianitsky, V.Y., & Korchagin, M.A. (2014). Possibilities of the Computer-Controlled Detonation Spraying method: A chemistry viewpoint. *Ceramics International*, *40*(2), 3253–3260.

2 Wang, F., Li, C., Zhang, S., & Liu, H. (2020). Tantalum coated on titanium dioxide nanotubes by plasma spraying enhances cytocompatibility for dental implants. *Surface and Coatings Technology*, *382*, 125161.

3 Kuo, T.Y., Chin, W.H., Chien, C.S., & Hsieh, Y.H. (2019). Mechanical and biological properties of graded porous tantalum coatings deposited on titanium alloy implants by vacuum plasma spraying. *Surface and Coatings Technology*, *372*, 399–409.

4 Lu, H., Shang, J., Jia, X., Li, Y., Li, F., Li, J., & Nie, Y. (2020). Erosion and corrosion behavior of shrouded plasma sprayed Cr_3C_2–NiCr coating. *Surface and Coatings Technology*, *388*, 125534.

5 Ulianitsky, V.Y., Batraev, I.S., Shtertser, A.A., Dudina, D.V., Bulina, N.V., & Smurov, I. (2018). Detonation spraying behaviour of refractory metals: Case studies for Mo and Ta-based powders. *Advanced Powder Technology*, *29*(8), 1859–1864.

6 Wu, L., Dong, Y., Yao, L., Liu, C., Al-Bishari, A.M., Yie, K.H.R., & Wu, G. (2020). Nanoporous tantalum coated zirconia implant improves osseointegration. *Ceramics International*, *46*(11), 17437–17448.

7 Vetrivendan, E., Jayaraj, J., Ningshen, S., Mallika, C., Kamachi, & Mudali U. (2018). Argon shrouded plasma spraying of tantalum over titanium for corrosion protection in fluorinated nitric acid media. *Journal of Thermal Spray Technology*, *27*, 512–523.

8 Zhou, H., Wang, X., He, C., Li, Z., & Zhu, L. (2022). Tantalum coatings deposited on Ti6Al4V alloy by self-designed wire electrical explosion spraying. *Journal of Thermal Spray Technology*, *31*(3), 636–643.

9 Rakhadilov, B.K., Muktanova, N., Kakimzhanov, D.N., & Kowalewski, P. (2024). Effect of HVOF method spraying parameters on phase composition and mechanical and tribological properties of 86WC-10Co-4Cr coating. *Bulletin of the University of Karaganda – Physics*, 115, 29(3), 71–83.

10 Barnett, B., Trexler, M., & Champagne, V. (2015). Cold sprayed refractory metals for chrome reduction in gun barrel liners. *International Journal of Refractory Metals and Hard Materials, 53*, 139–143.

11 Rakhadilov, B.K., Nugumanova, A.B., Kowalewski, P., Kylyshkanov, M.K., Bayatanova, L.B., & Kakimzhanov, D.N. (2020). Obtaining functional gradient coatings based on Al_2O_3 by detonation spraying. *Bulletin of the University of Karaganda – Physics,* 100(4), 22–27.

12 Rakhadilov, B., Maulet, M., Abilev, M., Sagdoldina, Z., & Kozhanova, R. (2021). Structure and tribological properties of Ni–Cr–Al-based gradient coating prepared by detonation spraying. *Coatings, 2*, 1–14.

13 Rakhadilov, B., Buitkenov, D., Sagdoldina, Z., Seitov, B., Kurbanbekov, S., & Adilkanova, M. (2021). Structural Features and Tribological Properties of Detonation Gun Sprayed Ti–Si–C Coating. *Coatings, 11*, 141.

14 Rybin, D.K., Batraev, I.S., Dudina, D.V., Ukhina, A.V., & Ulianitsky, V.Y. (2021). Deposition of tungsten coatings by detonation spraying. *Surface and Coatings Technology*, 409, 126943.

Д.Н. Кәкімжанов, З.А. Сатбаева, М.К. Даутбеков,
Е.С. Тұрабеков, Р.М. Қуанышбай, А.С. Рүстемов

Тозаңдандыру параметрлерінің Та негізіндегі детонациялық жабындардың қасиеттеріне әсері

Мақалада тозаңдандыру параметрлерінің тантал негізіндегі детонациялық жабындардың қасиеттеріне әсері қарастырылған. Алынған бүріккіш жабындардың қасиеттеріне әсер ететін маңызды параметрлердің бірі — оқпанды жарылғыш газбен толтыру көлемі. Тантал жабындары оқпанды толтырудың әртүрлі деңгейлерінде алынды (50-70 %). Нәтижелер оқпанды толтыру көлемі ұлғайған сайын жабындардың кедір-бұдырлығы төмендейтінін және құрылымы біркелкі болатынын көрсетті. Сынақ нәтижелері 60% толтыру кезінде жабынның басқа үлгілермен салыстырғанда коррозияға төзімділігі жоғары екенін айқындады. Зерттеу нәтижелері бойынша оқпанды жарылғыш газбен толтырудың оңтайлы режимі анықталды.

Кілт сөздер: қатайту, детонациялық бүрку, қаттылық, тантал, коррозия, құрылым, жабын, трибология

Д.Н. Какимжанов, З.А. Сатбаева, М.К. Даутбеков,
Е.С. Турабеков, Р.М. Куанышбай, А.С. Рустемов

Влияние параметров напыления на свойства детонационных покрытий на основе Та

В статье рассмотрено влияние параметров напыления на свойства детонационных покрытий на основе тантала. Одним из важных параметров, влияющим на свойства получаемых покрытий напыления, является объём заполнения ствола взрывчатым газом. Были получены покрытия из тантала при разных степенях заполнения ствола (50–70 %). Результаты показали, что при увеличении объёма заполнения ствола шероховатость покрытий уменьшается, а структура становится более однородной. Результаты исследований показали, что при 60 % заполнения покрытие имеет высокую коррозионную стойкость по сравнению с другими образцами. По результатам исследования был определён оптимальный режим заполнения ствола взрывчатым газом.

Ключевые слова: упрочнение, детонационное напыление, твердость, тантал, коррозия, структура, покрытие, трибология

Information about the authors

Kakimzhanov, Dauir (*corresponding author*) — Director of PlasmaScience LLP, Ust-Kamenogorsk, Kazakhstan; e-mail: d.kakimzhanov19@gmail.com; ORCID ID: https://orcid.org/0000-0001-9453-0456

Satbayeva, Zarina — PhD, ProfessorScience of Shakarim University, Semey, Kazakhstan; Leading Researcher of PlasmaScience LLP, Ust-Kamenogorsk, Kazakhstan; e-mail: zarinavkgu@gmail.com; ORCID ID: https://orcid.org/ 0000-0001-7161-2686

Dautbekov, Merkhat — Leading Researcher, PlasmaScience LLP, Ust-Kamenogorsk, Kazakhstan; e-mail: nurbol.ber@gmail.com; ORCID ID: https://orcid.org/0009-0000-6880-6439

Turabekov, Yernar — Junior Researcher of PlasmaScience LLP, Ust-Kamenogorsk, Kazakhstan; e-mail: ernarturabekov28@gmail.com, ORCID: https://orcid.org/0009-0003-1946-3902

Kuanyshbai, Rashid — Junior Researcher of PlasmaScience LLP, Ust-Kamenogorsk, Kazakhstan; e-mail: rashidmaratly08@gmail.com, ORCID: https://orcid.org/0009-0009-7661-2605

Rustemov, Anuar — Junior Researcher of PlasmaScience LLP, Ust-Kamenogorsk, Kazakhstan; e-mail: anuarrustemovv05@gmail.com, ORCID: https://orcid.org/0009-0003-3962-294X

Article
https://doi.org/10.31489/2025PH1/60-67
UDC 620.92

Received: 17.06.2024
Accepted: 27.11.2024

N.K. Tanasheva[1, 2*], A.A. Potapova[1, 2], L.L. Minkov[3], A.S. Tussypbayeva[1], A.N. Dyusembaeva[1], E.K. Mussenova[1], B.B. Kutum[1], A.Z. Tleubergenova[1]

[1]*Karaganda Buketov University, Karaganda, Kazakhstan;*
[2]*"Alternative Energy" Research Center, Karaganda, Kazakhstan;*
[3]*National Research Tomsk State University, Tomsk, Russia*
*(*Corresponding author's e-mail: nazgulya_tans@mail.ru*

Influence of Climatic Parameters on the Photovoltaic Conversion Efficiency of a Polycrystalline Solar Panel

The efficiency of electricity generation by solar panels depends on many factors, one of which is the temperature of the semiconductor layer. An increase in this parameter leads to a decrease in the efficiency of the module, since the speed of electron movement increases, therefore, the resistance increases. Conversely, the lower the temperature of the silicon cells, the lower the resistance and the higher the efficiency. However, the temperature of the silicon cells depends on a number of parameters: wind speeds, insolation, and ambient temperatures. Therefore, depending on the region and time of year, the same solar module will have different performance. Based on this, an urgent issue when planning the use of solar panels is the possibility of determining how much the efficiency of photovoltaic conversion in a particular area will decrease. Therefore, to study the variability of efficiency indicators, a simulation of the temperature change of the semiconductor layer of the polycrystalline solar panel KZPV 220 M60 was carried out, taking into account climatic parameters in winter and summer days for three cities of Kazakhstan — Petropavlovsk, Karaganda and Shymkent. As a result of modeling, it was found that on July 12, solar cells reach their maximum temperature of 64.4 °C in Shymkent, 49.8 °C in Karaganda and 52.1 °C in Petropavlovsk, while efficiency decreases by 2.7 %, 1.7 % and 1.8 %, respectively, relative to the efficiency of the solar module under standard conditions (insolation 1000 W/m^2, temperature 25 °C, spectrum $AM = 1.5$). At the same time, on December 12, T_{max}: in Shymkent 11.5 °C, in Karaganda — 15.8 °C, in Petropavlovsk — 16.7 °C, and efficiency increases by 0.9 %, 2.7 %, 2.8 %, respectively.

Keywords: solar panel, photocells, temperature, wind speed, insolation, efficiency, atmospheric mass, zenith angle

Introduction

Solar energy has many disadvantages, such as: high cost, dependence on the location of photovoltaic panels, toxic components of solar cells, dependence of the production of photovoltaic panels on the time of day, time of year, the presence of rain and cloudy weather, a decrease in the efficiency of the panel with an increase in its temperature. However, despite all these disadvantages, solar energy is a promising source of electric energy due to the fact that the technology and composition of solar cells and their efficiency are constantly being improved [1].

The performance of solar panels is not constant. Also photovoltaic conversion efficiency is influenced by various factors: reflectance, thermodynamic efficiency, and charge carrier separation efficiency, charge carrier collection efficiency, quality of materials, surface contamination and climatic conditions.

Theoretically, the limit of thermodynamic efficiency, equal to the absolute maximum possible efficiency of converting sunlight into electricity, is about 86 %. This value is an approximation (i.e. the Chambadal-Novikov efficiency) associated with the Carnot limit and is based on the temperature of the photons emitted from the surface of the Sun. In contrast, the actual thermodynamic efficiency limit is significantly lower and is about 33 % in the case of single-compound technology. This means conversion efficiency is no more than 12–21 % for commercial PV panels or up to 24.5 % for high-efficiency single junction cells [2].

Moreover, it is widely known that photovoltaic conversion efficiency is strictly related to the operating temperature of the cells [3].

For example, in [4] it was found that efficiency decreases by 0.38–0.42 % (i.e., in relative percentage), and in [5] that electrical power decreases by 0.4–0.5 % for every 1 degree of temperature increase in silicon cells. The usual simplification is to consider a linear decrease in panel efficiency by 1 % (i.e., in absolute percentage) every 10 degrees [6]. The temperature of the photovoltaic module (PVM) increases due to the absorption of solar radiation in the semiconductor layer, and the efficiency of the solar photovoltaic system

(PVS) decreases when the module is poorly cooled [7]. Thus, the insolation level, air temperature and wind speed significantly impact the solar panel's efficiency.

Basically, crystalline silicon FEPs were in the greatest demand on the market. Over time, other designs have been developed, for example, thin-film, multilayer, transient, cascade, etc. The designs of thin-film SE worked more efficiently at high temperature, but the efficiency in comparison with crystalline ones turned out to be almost two times lower (6–8 %) [8].

During hot summer periods, solar panels heat up to an average of 75 °C, and in equatorial regions to 80–90 °C. Overheating of the solar panel not only reduces its efficiency, but also shortens its service life. Even in modern solar panels, the problem of overheating has not been solved, for example, gallium arsenide modules with an efficiency of 46 % at 25 °C lose 20 % of their output at 70 °C, and as much as 30 % at 90 °C [9].

Due to its geographical location, the change of seasons is noticeably pronounced in the territory of Kazakhstan, and there are also differences in climatic conditions in different regions of the country. Therefore, when designing a photovoltaic system, it is essential to consider the influence of climatic factors characteristic of the area. For example, in winter and summer, solar modules produce different amounts of electricity due to differences in the length of daylight hours and various degrees of heating of photocells due to differences in air temperature and wind speed.

Methods and materials

To simulate the variations in operating temperature of solar cells under different conditions, the ANSYS software was utilized to create a detailed three-dimensional finite element model of the KZPV 220 M60 polycrystalline solar panel (Fig. 1):

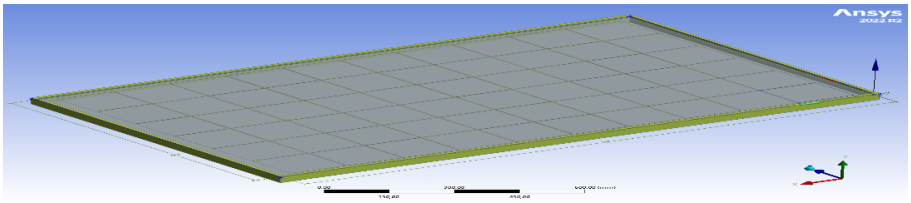

Figure 1. 3D model of a polycrystalline solar panel KZPV 220 M60 in ANSYS software

Main characteristics of the solar module under standard conditions:
– Rated maximum power — 220 W;
– Voltage at maximum power — 29.40 V;
– Current strength at maximum power — 7.5 A;
– Photocells — 60 polycrystalline cells;
– Cell size — 156×156 mm;
– Dimensions — 1.649×992×40 mm.

The climatic parameters of Petropavlovsk, Karaganda and Shymkent were chosen as boundary conditions at noon on one of the hottest days of summer — July 12, 2023, and at noon on one of the coldest days of winter — December 12, 2023 (Table):

T a b l e

Basic parameters for setting boundary conditions

City	Petropavlovsk		Karaganda		Shymkent	
Date	12.07.23	12.12.23	12.07.23	12.12.23	12.07.23	12.12.23
Air temperature, °C	36	–33	35	–28	39	–18
Wind speed, m/s	4	2	5	5	2	1
Insolation, W/m^2	907,86	625	924,2	759	922,7	833

Although Karaganda is more distant from the equator than Shymkent, the table shows that the insolation level of 12.07.23 in the first city is 1.5 W/m^2 higher than in the second. This difference can be explained by the difference in altitude above sea level — Karaganda is 553 m, Shymkent is 506 m — since the higher the object is located, the more solar radiation reaches its surface.

Air temperature and wind speed are taken from the source [10].

The insolation value is calculated based on atmospheric mass. Atmospheric mass is the length of the path light takes through the atmosphere relative to the shortest possible path (when the Sun is at its zenith). The formula for calculating atmospheric mass taking into account the curvature and sphericity of the Earth [11]:

$$AM = \frac{1}{\cos\theta + 0.50572\left(96.07995 - \theta\right)^{-1.6364}}, \quad (1)$$

where θ is the angle measured from the vertical (zenith angle).

The value of the zenith angle can be calculated from the equation:

$$\cos\theta = \cos\varphi\cos\delta\cos\omega + \sin\varphi\sin\delta, \quad (2)$$

where φ is the geographic latitude of the area, ω is the hour angle (at noon is 0), δ is the declination of the Sun, which can be found from the approximate Cooper equation:

$$\delta = 23.45\sin\left(360\frac{284+n}{365}\right), \quad (3)$$

where *n* is the serial number of the day of the year, counted from January 1.

The daily intensity of the direct component of sunlight can be determined as a function of atmospheric mass:

$$I_D = 1353 \cdot 0.7^{\left(AM^{0.678}\right)}, \quad (4)$$

where I_D is the intensity at the site perpendicular to the Sun's rays in W/m^2, AM is the atmospheric mass, 1353 W/m^2 is the solar constant, and 0.7 takes into account the fact that about 70 % of solar radiation arriving at the boundary of the atmosphere reaches the ground. The indicator 0.678 is an empirical coefficient that considers atmospheric layers' heterogeneity.

Diffuse radiation is about 10 % of direct radiation even in a clear sky. Therefore, on a clear day, the total intensity of radiation incident on the module is equal to:

$$I_G = 1.1 \cdot I_D. \quad (5)$$

The efficiency of a solar battery under standard conditions (insolation 1000 W/m^2, temperature 25 °C, spectrum AM = 1.5) can be determined by the formula [12]:

$$\eta = P_{STC} \div 1000\ \mathrm{W/m^2} \div S, \quad (6)$$

where P_{STC} is power under standard conditions, *S* is area.

Thus, equation (6) states that the efficiency of the KZPV 220 M60 polycrystalline solar panel is 15 %.

However, since it is known that the efficiency of photoelectric conversion decreases with increasing temperature of the solar module, the efficiency factor taking into account the heating of photocells is calculated by the formula [13]:

$$\eta_{pi} = \eta_0(1 - 0.0045(T_{pi} - 25)), \quad (7)$$

where η_{pi} is the panel efficiency, %; η_0 — solar panel efficiency at a temperature of 25 °C, %; T_{pi} — solar panel surface temperature, °C.

Results and discussions

Modelling of temperature changes and distribution as a result of heating a layer of photocells was carried out for each case separately, considering the boundary conditions corresponding to the climatic factors characteristic of the regions.

As a result, the values of the maximum temperature reached by the silicon layer when heated on December 12 and July 12 were obtained (Fig. 2).

Several conclusions can be drawn from the data in Figure 2.

Firstly, the most intense heating of the solar module in summer is observed in the climatic conditions of Shymkent — 64.4 °C, while in Karaganda and Petropavlovsk — 49.8 °C and 52.1 °C, respectively. The maximum temperature of the silicon layer in Shymkent is higher than the maximum temperatures in Karaganda and Petropavlovsk — by 14.6 °C and 12.3 °C, respectively. This difference is due to differences in climatic conditions, namely:

– Ambient temperature: Shymkent (39 °C) > Petropavlovsk (36 °C) > Karaganda (35 °C);
– Wind speed: Karaganda (5 m/s) > Petropavlovsk (4 m/s) > Shymkent (2 m/s);
– Insolation: Karaganda (924.2 W/m^2) > Shymkent (510.46 W/m^2) > Petropavlovsk (907.86 W/m^2).

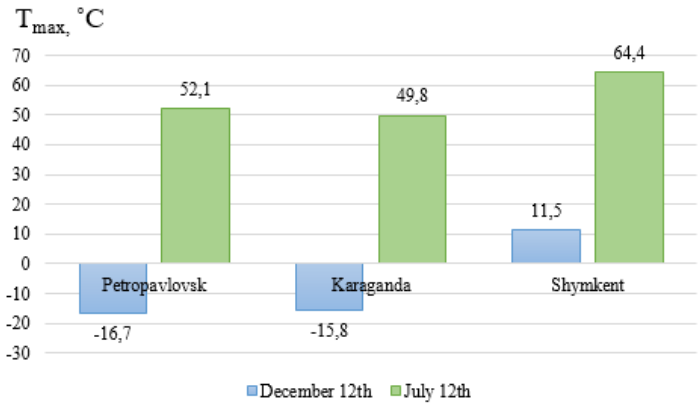

Figure 2. Maximum temperature reached by photocells

Thus, the reason for more intense heating of solar cells in Shymkent than in the other two cities is high air temperatures and insolation levels, which contribute to an increase in the temperature in the silicon layer, as well as the lowest wind speed, which provides insufficient cooling due to convection.

It can also be noted that the panel heated up more (by 2.3 °C) in Petropavlovsk than in Karaganda, even though Petropavlovsk is located north of Karaganda and has a lower insolation level. However, this result is because the module's cooling intensity in the first city is less than in the second since the air temperature in Petropavlovsk is 1 °C higher, and the wind speed, on the contrary, is 1 m/s less than in Karaganda.

Secondly, similar dynamics can be observed in winter: the panel in Shymkent heated up more than in the other two cities (up to 11.5 °C), but the difference between the temperature values is much more significant than in summer. In this case, the maximum temperature of solar cells in Shymkent is higher than the maximum temperatures in Karaganda and Petropavlovsk — by 27.3 °C and 28.2 °C, respectively. The results obtained are associated with more significant differences in the climatic conditions of cities than in the summer period:

– Ambient temperature: Shymkent (–18 °C) > Karaganda (–28 °C) > Petropavlovsk (–33 °C);

– Wind speed: Karaganda (5 m/s) > Petropavlovsk (2 m/s) > Shymkent (1 m/s);

– Insolation: Shymkent (833 W/m^2) > Karaganda (759 W/m^2) > Petropavlovsk (625 W/m^2).

The difference in insolation and air temperature for Shymkent and Karaganda is 74 W/m^2 and 10 °C and for Shymkent and Petropavlovsk — 208 W/m^2 and 15 °C.

Thus, the reason for the higher temperature of solar cells in Shymkent than in the other two cities, as in the first case, is the high values of air temperature and insolation level and the lowest wind speed.

It can also be noted that, in contrast to the first case, in Karaganda, the panel heated up more (by 0.9 °C) than in Petropavlovsk; in other words, in Petropavlovsk, the solar module has the lowest degree of heating due to the lowest ambient temperatures and insolation.

Let's consider how changing solar cell operating temperature affects photovoltaic conversion efficiency in both cases. The solar module's efficiency under standard conditions is 15 %; Figure 3 shows the efficiency values at maximum solar cell temperatures (T_{max}) on December 12 and July 12, 2023.

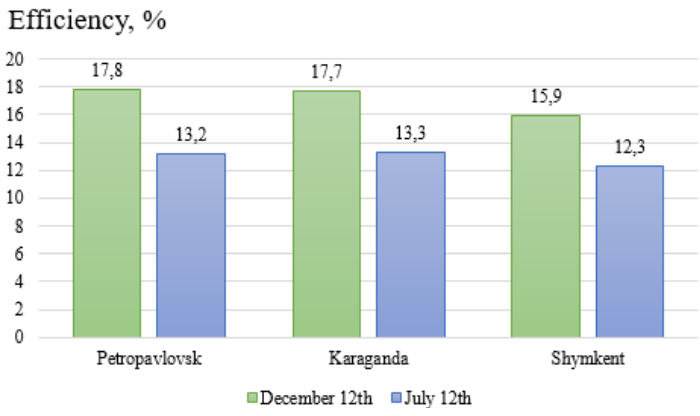

Figure 3. Efficiency values at maximum temperature of photocells

As shown in Figure 3, the efficiency of solar panels on December 12 is higher for all cities compared to July 12 because, during the winter period, the modules heat up significantly less than in the summer period, meaning thermal losses in energy production are less pronounced.

As a result, on July 12, when the layer of solar cells reaches the maximum temperature, the efficiency decreases by 1.8 % in Petropavlovsk, 1.7 % — in Karaganda and 2.7 % — in Shymkent, that is, the lowest efficiency corresponds to the city with the highest maximum temperature — Shymkent.

However, on December 12, the efficiency in all cities on the contrary, increased due to the lower temperature of the solar cells. However, in Shymkent, the efficiency of the module still remains the lowest, as in the first case — 15.9 %, while in Karaganda and Petropavlovsk — 17.7 % and 17.8 %, respectively.

It can be noted that on December 12, the efficiency of solar panels exceeded the value under standard conditions and was, on average, 4.3 % higher than on July 12. This is because the efficiency of solar panels in sunny winter weather is higher than in summer, as, at lower temperatures, electrons in the semiconductor layer move more slowly, which leads to reduced resistance and, consequently, increased efficiency.

Conclusion

As a result of the simulation, it was found that on July 12, solar cells reached their maximum temperatures of 64.4 °C in Shymkent, 49.8 °C — in Karaganda and 52.1 °C — in Petropavlovsk, while on December 12, the values were much lower: in Shymkent — 11.5 °C, in Karaganda — –15.8 °C, in Petropavlovsk — –16.7 °C.

Based on the obtained temperatures, the efficiency values were calculated: on July 12, when the layer of photocells reaches its maximum temperature, the efficiency decreases by 1.8 % in Petropavlovsk, 1.7 % — in Karaganda and 2.7 % — in Shymkent, but on December 12, on the contrary, it increases by 2.8 % in Petropavlovsk, 2.7 % — in Karaganda and only 0.9 % — in Shymkent. The difference in efficiency between the two dates averages 4.3 %.

Thus, the loss of efficiency in Shymkent due to increasing the temperature of solar cells is greater than in Karaganda and Petropavlovsk, which is caused by a hotter climate and a higher level of insolation.

The closer to the north and further from the equator, the solar module is located, the less intensely the solar cells heat up. This happens because as you move away from the equator, the amount of solar radiation reaching the Earth decreases, that is, the level of insolation, and the climate becomes colder; therefore, the air temperature decreases. Then, less solar energy reaches the surface of the solar panel, which means less of this energy is converted into heat due to absorption by silicon cells, and due to the lower ambient temperature, more efficient cooling occurs due to radiation and convection. At the same time, the lower the operating temperature of photocells, the greater their efficiency.

Acknowledgments

The work was carried out with the financial support of the Science Committee of the Ministry of Science and Higher Education of the Republic of Kazakhstan (IRN AP22785282 “Automation process detecting errors and improving efficiency operation compact combined power plant based on solar panels and wind generators”).

References

1 Дашеев С. Солнечная энергетика: состояние и перспективы / С. Дашеев, Е. Малышев // Вестник науки и образования. — 2018. — № 53. — С. 51–53.

2 Koyuncu T. Practical Efficiency of Photovoltaic Panel Used for Solar Vehicles / T. Koyuncu // IOP Conf. Ser.: Earth Environ. Sci. — 2017. — Vol. 83. — 012001.

3 Skoplaki E. On the Temperature Dependence of Photovoltaic Module Electrical Performance: A Review of Efficiency / Power Correlations / E. Skoplaki, J. Palyvos // Solar Energy. — 2009. — Vol. 83. — P. 614–624.

4 Evans D.L. Simplified method for predicting photovoltaic array output / D.L. Evans // Solar Energy. — 1981. — Vol. 27. — No. 6. — P. 555–560.

5 Green M.A. Solar cells: Operating principles, technology, and system applications. — Englewood Cliffs, 1982. — P. 92–98. ISBN 0-13-822270-3.

6 Incropera P.F., De Witt P.D. Fundamentals of heat and mass transfer / P.F. Incropera, P.D. De Witt. — 5th edition. — John Wiley and Sons, 2002. — ISBN 0-471-38650-2.

7 Виссарионов В.И. Солнечная энергетика / В.И. Виссарионов, Г.В. Дерюгина, В.А. Кузнецова, Н.К. Малинин; под ред. В.И. Виссарионова. — Изд. дом МЭИ, 2008. — 320 с.

8 Жураева З.И. Обзорный анализ основных видов солнечных элементов и выявление путей повышения эффективности их работы и применения [Электронный ресурс] / З.И. Жураева // Журнал Universum: технические науки. — 2018. — № 10(55). — Режим доступа: https://cyberleninka.ru/article/n/obzornyy-analiz-osnovnyh-vidov-solnechnyh-elementov-i-vyyavlenie-putey-povysheniya-effektivnosti-ih-raboty-i-primeneniya/viewer

9 Трембач С.А. Проблема перегрева солнечных панелей. Способы решения путем электронной тонировки / С.А. Трембач // Энергетический вестник. — 2020. — № 26. — С. 47–51.

10 Weather Spark. — [Electronic resource]. — Access mode: https://ru.weatherspark.com/

11 United Solar Technologies. — [Electronic resource]. — Access mode: http://ust.su/solar/media/section-inner12/637/

12 Мирзокобилова Ф. Влияние климатических условий на эффективность солнечной фотоэлектрической установки / Ф. Мирзокобилова, Д. Нозиров, С.Ф. Абдуллаев, К. Кабутов, М.А. Салиев // Инновационная наука. — 2020. — № 4. — С. 51–57.

13 Головко С.В. Анализ влияния климатических факторов на выбор типа солнечной панели / С.В. Головко, Д.А. Задоркин // Вестник Астраханского государственного технического университета. — 2020. — Т. 2 (70). — С. 21–26.

Н.К. Танашева, А.А. Потапова, Л.Л. Миньков, А.С. Тусыпбаева,
А.Н. Дюсембаева, Е.К. Мусенова, Б.Б. Кутум, А.Ж. Тлеубергенова

Климаттық параметрлердің поликристалды күн панелінің фотоэлектрлік түрлендіру тиімділігіне әсері

Күн батареяларының электр энергиясын өндірудің тиімділігі көптеген факторларға, яғни олардың бірі жартылай өткізгіш қабаттың температурасына байланысты. Бұл параметрдің жоғарылауы модульдің тиімділігінің төмендеуіне әкеледі, өйткені электрондардың қозғалыс жылдамдығы өседі, сондықтан қарсылық артады. Керісінше, шақпақ тас жасушаларының температурасы неғұрлым төмен болса, соғұрлым қарсылық аз болады және тиімділігі жоғары болады. Алайда, шақпақ тас жасушаларының температурасы бірқатар параметрлерге байланысты: желдің жылдамдығы, инсоляция және қоршаған орта температурасы. Демек, аймақ пен жыл мезгіліне байланысты бір күн модулі әртүрлі өнімділікке ие болады. Осыған сүйене отырып, күн батареяларын пайдалануды жоспарлаудағы өзекті мәселе белгілі бір аймақтағы фотоэлектрлік түрлендірудің тиімділігі қанша төмендейтінін анықтау мүмкіндігі. Сондықтан тиімділік көрсеткіштерінің вариативтілігін зерттеу үшін Қазақстанның үш қаласы — Петропавл, Қарағанды және Шымкент үшін қысқы және жазғы күндердегі климаттық параметрлерді ескере отырып, KZPV 220 M60 поликристалды күн панелінің жартылай өткізгіш қабатының температурасының өзгеруін модельдеу жүргізілді. Модельдеу нәтижесінде 12 шілдеде күн жасушалары Шымкентте 64,4 °С-қа, Қарағандыда 49,8 °С-қа және Петропавлда 52,1 °С-қа тең ең жоғары температураға жететіні анықталды, бұл ретте тиісінше ПӘК 2,7 %-ға, 1,7 %-ға және 1,8 %-ға төмендейді. Сонымен қатар, 12 желтоқсанда T_{max}: Шымкентте –11,5 °С, Қарағандыда –15,8 °С, Петропавлда –16,7 °С, ал тиісінше ПӘК 0,9 %, 2,7 %, 2,8 %-ға артады.

Кілт сөздер: күн панелі, фотоэлементтер, температура, желдің жылдамдығы, инсоляция, тиімділік, атмосфералық масса, зенит бұрышы.

Н.К. Танашева, А.А. Потапова, Л.Л. Миньков, А.С. Тусыпбаева,
А.Н. Дюсембаева, Е.К. Мусенова, Б.Б. Кутум, А.Ж. Тлеубергенова

Влияние климатических параметров на эффективность фотоэлектрического преобразования поликристаллической солнечной панели

Эффективность выработки электроэнергии солнечными батареями зависит от множества факторов, одним из которых является температура полупроводникового слоя. Увеличение данного параметра приводит к снижению КПД модуля, так как возрастает скорость движения электронов, следовательно, повышается сопротивление. И наоборот, чем меньше температура кремневых ячеек, тем меньше сопротивление и больше КПД. В свою очередь температура кремниевых ячеек зависит от других параметров: скорости ветра, инсоляции и температуры окружающей среды. Следовательно, в зависимости от региона и времени года один и тот же солнечный модуль будет иметь разную производительность. Исходя из этого, актуальным вопросом при планировании использования солнечных батарей является возможность определения снижения эффективности фотоэлектрического преобразования в той или иной местности. Поэтому для исследования вариативности показателей КПД было проведено моделирование изменения температуры полупроводникового слоя поликристаллической солнечной панели KZPV 220 M60 с учётом климатических параметров в зимний и летний период для трёх городов Казахстана — Петропавловска, Караганды и Шымкента. В результате моделирования было установлено,

что 12 июля солнечные ячейки достигали своей максимальной температуры, равной 64,4 °С в Шымкенте, 49,8 °С в Караганде и 52,1 °С в Петропавловске, при этом КПД снизилось на 2,7 %, 1,7 % и 1,8 % относительно стандартной температуры 25 °С. В то же время 12 декабря T_{max} в Шымкенте — 11,5 °С, в Караганде — минус 15,8 °С, в Петропавловске — минус 16,7 °С, а КПД повысилось на 0,9 %, 2,7 %, 2,8 %.

Ключевые слова: солнечная панель, фотоэлементы, температура, скорость ветра, инсоляция, КПД, атмосферная масса, зенитный угол.

References

1 Dasheev, S. & Malyshev, E. (2018). Solnechnaia energetika: sostoianie i perspektivy [Solar Energetics: State and Prospects]. *Vestnik nauki i obrazovaniia — Bulletin of Science and Education*, 53, 51–53 [in Russian].

2 Koyuncu, T. (2017). Practical Efficiency of Photovoltaic Panel Used for Solar Vehicles. *IOP Conf. Ser.: Earth Environ. Sci.*, *83*, 012001.

3 Skoplaki, E. & Palyvos, J. (2009). On the Temperature Dependence of Photovoltaic Module Electrical Performance: A Review of Efficiency / Power Correlations. *Solar Energy*, 83, 614–624.

4 Evans, D.L. (1981). Simplified method for predicting photovoltaic array output. *Solar Energy*, *27*(6), 555–560.

5 Green, M.A. (1982). Solar cells: Operating principles, technology, and system applications. *Englewood Cliffs,* 92–98. ISBN 0-13-822270-3.

6 Incropera, P.F. & De Witt, P.D. (2002). Fundamentals of heat and mass transfer (5th edition). *John Wiley and Sons*, ISBN 0-471-38650-2

7 Vissarionov, V.I., Deryugina, G.V., Kuznetsova, V.A., & Malinin N.K. (2008). *Solnechnaia energetika [Solar Energetics]* (Ed. by V.I. Vissarionov). Izdatelskii dom MJeI, 320 [in Russian].

8 Zhuraeva, Z.I. (2018). Obzornyi analiz osnovnykh vidov solnechnykh elementov i vyiavlenie putei povysheniia effektivnosti ikh raboty i primeneniia [A review analysis of the main types of solar cells and identification of ways to improve their efficiency and application]. *Zhurnal Universum: tekhnicheskie nauki — Journal Universum: Technical Sciences*, 10(55). Retrieved from https://cyberleninka.ru/article/n/obzornyy-analiz-osnovnyh-vidov-solnechnyh-elementov-i-vyyavlenie-putey-povysheniya-effektivnosti-ih-raboty-i-primeneniya/viewer [in Russian]

9 Trembach, S.A. (2020). Problema peregreva solnechnykh panelei. Sposoby resheniia putem elektronnoi tonirovki [The problem of overheating solar panels. Solutions using electronic tinting]. *Zhurnal Energeticheskii Vestnik — Journal Energy Bulletin*, 26, 47–51 [in Russian].

10 Weather Spark. Retrieved from https://ru.weatherspark.com/

11 United Solar Technologies. Retrieved from http://ust.su/solar/media/section-inner12/637/

12 Mirzokobilova, F., Nozirov, D., Abdullaev, S.F., Kabutov, K., & Saliev, M.A. (2020). Vliianie klimaticheskikh uslovii na effektivnost solnechnoi fotoelektricheskoi ustanovki [The Impact of Climate Conditions on Solar Photovoltaic Plant Efficiency]. *Zhurnal Innovatsionnaia nauka — Innovative Science Journal*, 4, 51–57 [in Russian].

13 Golovko, S.V. & Zadorkin, D.A. (2020). Analiz vliianiia klimaticheskikh faktorov na vybor tipa solnechnoi paneli [Analysis of the influence of climatic factors on the choice of solar panel type]. *Vestnik Astrakhanskogo gosudarstvennogo tehnicheskogo universiteta — Bulletin of the Astrakhan State Technical University*, *2* (70), 21–26 [in Russian].

Information about the authors

Tanasheva, Nazgul (*corresponding author*) — PhD, Associate Professor, Karaganda Buketov University, Karaganda, Kazakhstan; e-mail: nazgulya_tans@mail.ru; ORCID ID https://orcid.org/0000-0003-4273-0960

Tussupbayeva, Ardak — 1st year doctoral student, Karaganda Buketov University, Karaganda, Kazakhstan; e-mail: ardak.1888_04@mail.ru, ORCID ID https://orcid.org/0009-0007-5402-3434

Minkov, Leonid — Doctor of Physical and Mathematical Sciences, Professor, Tomsk State University, Tomsk, Russia; e-mail: lminkov@ftf.tsu.ru, ORCID ID https://orcid.org/0000-0001-6776-6375

Potapova, Arina — 3rd year undergraduate student, Karaganda Buketov University, Karaganda, Kazakhstan; e-mail: arina_no_way@mail.ru, ORCID ID https://orcid.org/0009-0000-7504-1569

Dyusembaeva, Ainura — PhD, Karaganda Buketov University, Karaganda, Kazakhstan; e-mail: aikabesoba88@mail.ru; ORCID ID https://orcid.org/0000-0001-6627-7262

Mussenova, Elmira — Candidate of Physical and Mathematical Sciences, Associate professor of the Physics and Nanotechnology Department, Karaganda Buketov University, Karaganda, Kazakhstan; e-mail: emusenova@mail.ruSCOPUS Author ID: 56242227100; ORCID ID - 0000-0001-5458-3641

Kutum, Bayan — Senior Lecturer, Karaganda Buketov University, Karaganda, Kazakhstan; e-mail: kuttykadam@mail.ru, ORCID: https://orcid.org/0000-0002-6410-4111

Tleubergenova, Akmaral — Doctoral student, Karaganda Buketov University, Karaganda, Kazakhstan; e-mail: akmaral.tzh7@mail.ru, ORCID ID: https://orcid.org/0009-0009-5152-0050

Article
https://doi.org/10.31489/2025PH1/68-76
UDC 621.7.02

Received: 28.11.2024
Accepted: 28.01.2025

L.G. Sulyubayeva, Zh. Sagdoldina, D.R. Baizhan, N.E. Berdimuratov*, S.D. Bolatov

Sarsen Amanzholov East Kazakhstan University, Ust-Kamenogorsk 070000, Kazakhstan
*(*Corresponding author's e-mail: nurbol.ber@gmail.com)*

The Analysis of Structure Change and Tribomechanical Properties of Alloyed Steel Surfaces Modified by Diffusion Electrolyte-Plasma Boriding Method

Nowadays, one of the key requirements in mechanical engineering when manufacturing parts from constructional steels is the hardness and wear resistance parameters. One of the relevant solutions to this issue could be diffusion-electrolytic-plasma boriding, as the steel surface is enriched with boron elements during treatment, while the core of the part remains in its original state. This study addresses the technological capabilities of the diffusion-electrolytic-plasma boriding method for steels. The steel 30CrMnSiA was treated on a diffusion-electrolytic-plasma boriding setup. The treatment duration was 5 and 7 minutes, using a 15 % sodium carbonate (Na_2CO_3) and 20 % borax ($Na_2B_4O_7$) aqueous solution as the electrolyte. It was established that the cross-sectional structure of the steel after diffusion-electrolytic-plasma boriding is characterized by zoning, with the formation of a modified layer approximately 650 μm thick. As a result of diffusion-electrolytic-plasma boriding, the microhardness of 30CrMnSiA steel is enhanced by 2.5 to 3 times in comparison to its original state, due to the formation of hardening phases.

Keywords: diffusion, electrolyte, plasma, boriding, structure, surface modification, surface, borax

Introduction

Traditional steel processing methods have focused on thermal processes such as heating and cooling, which have been used for a long time. These techniques require heating the metal in a furnace followed by cooling it in air, water, or oil [1]. However, these processes can be expensive due to the need for specialized equipment and extended processing times, and they often require large, cumbersome machinery [2]. Recently, an innovative method of processing steel parts, electrolyte-plasma heat treatment, has emerged that overcomes many of the limitations of traditional methods [3]. This method can significantly improve the physical and mechanical properties of steel in a short time — only a few seconds, unlike traditional methods, which can take hours and days. Electrolyte-plasma hardening is an intricate process that merges physical metallurgy with electrochemical technologies. It involves heating the sample in cathodic mode, enabling simultaneous phase transformation and deformation [4].

To improve the strength characteristics of structural and tool steels, a thermocyclic approach known as thermocyclic electrolytic-plasma treatment is used within the framework of electrolytic-plasma treatment [5]. Unlike other types of heat treatment, this method involves multiple repetitions of the heating and cooling cycle, which allows to significantly improve the quality of the material and achieve properties that cannot be obtained with a single heat treatment step. The changes from cycle to cycle are most commonly attributed to plastic deformation. The efficiency of thermocyclic electrolytic-plasma treatment is mainly influenced by the interactions between various phases and the structural transformations in alloys caused by microplastic deformation and the subsequent recrystallization process. Microplastic deformation boosts the strength of steel, while recrystallization enhances its ductility [6].

The effectiveness of electrolyte-plasma thermocyclic treatment is significantly influenced by factors such as cycle temperatures, the number of cycles, and the rates of heating and cooling [7]. The range of methods for thermocyclic electrolyte-plasma treatment, which differ in terms of their operational principles (including complete, partial, or no phase transformations) and energy requirements, which can vary by a factor of 20 to 50, offers potential for optimizing the process [8]. This highlights the necessity for developing and implementing more efficient technologies for the hardening of structural and tool steels to enhance product quality, operational lifespan, and reduce energy consumption, which is crucial for economic considerations.

Traditional furnace heat treatment methods face a number of restrictions, such as the risk of deformation, warping and cracking, long heating (1 to 20 hours) and cooling cycles, as well as limited automation and other difficulties.

In mechanical engineering, multi-component chemical heat treatment (CHT) is commonly applied to improve the surface characteristics of steels and alloys. This process involves either simultaneous or sequential diffusion of various chemical elements into the surface layers [9]. Techniques like nitriding and carbonitriding, which are part of CHT, significantly enhance the wear resistance, corrosion resistance, and other performance attributes of machine parts. However, the full understanding of how nitrided and carbonitrided layers form, with a combination of desirable properties such as high wear and corrosion resistance, is still incomplete [10]. Conventional chemical-thermal treatments, like nitriding in a gas environment and carburizing with solid carburizers, have limitations, including challenges in controlling the diffusion-active medium, the need for expensive equipment, and the necessity of multiple heat treatment cycles to achieve the final desired properties of the product.

A promising approach to enhancing the service life and performance of steel components is chemical-thermal treatment with electrolyte-plasma action (diffusion saturation). This method is used to introduce light elements such as nitrogen, boron, and carbon into the surface of materials [11]. Compared to traditional surface modification techniques, this technology offers several advantages, including faster processing times, lower costs, and the ability to combine diffusion saturation with hardening in a single technological process. The results of studies conducted by various scientific groups confirm the significant potential of electrolyte-plasma treatment of metals and alloys, but the tribological characteristic of this method remains insufficiently studied [12]. It is important to conduct a more detailed analysis of the wear mechanism in steel products following electrolytic-plasma treatment and examine it under a variety of conditions.

Due to the above, the aim of this paper is to analyze the changes in the structure and tribomechanical surface properties of alloyed steel before and after diffusion electrolyte-plasma boriding.

Materials and methods

In this research work, samples from 30CrMnSiA alloy steel with the size of 33×30×9 mm were selected as research objects for diffusion-electrolyte-plasma boriding (DEPB). Before the experiments, the samples were pre-treated with grinding paper with P2000 grit.

Figure 1 shows a general view of an image of the modernized diffusion-electrolyte-plasma boriding (DEPB) unit.

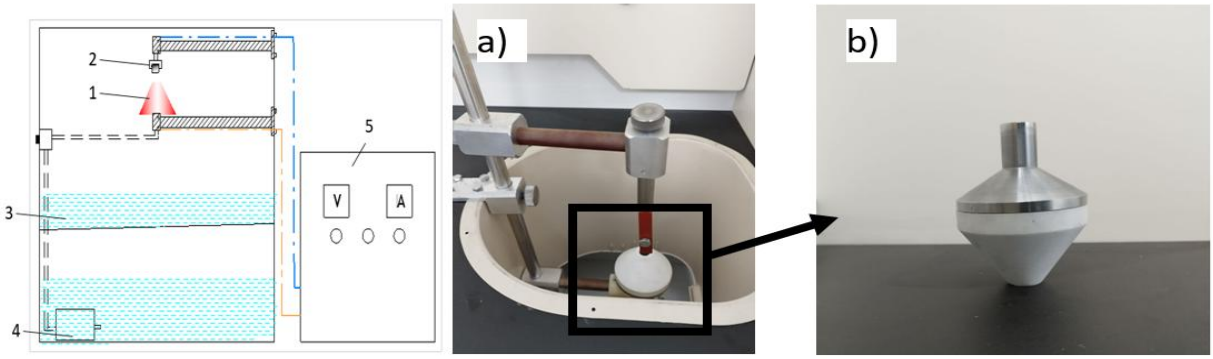

1 — anode; *2* — sample; *3* — electrolyte bath; *4* — pump; *5* — power supply; *a* — sample holder; *b* — nozzle

Figure 1. Image of the unit for diffusion-electrolyte-plasma boriding

The unit includes a high-power rectifier that provides direct current with a maximum output of 360 V and 100 A. The electrodes are composed of a cathode (sample) and an anode, which is shaped like a circular plate with perforations to ensure the even distribution of the electrolyte. The electrolyte used is an aqueous solution containing soda ash (Na_2CO_3) and borax ($Na_2B_4O_7$) in certain proportions, which is considered optimal for the formation of stable plasma [13].

The key factor in the process (DEPB) is the potential difference between the anode and cathode [14]. To determine the value of the potential difference of this process, the volt-ampere characteristics (VAC) of the anode and cathode were plotted (Fig. 2). The first region (I) region of linear dependence of current and voltage (U = 0–140 V i.e. (zone of classical electrolysis) [15]. The second region (II) of electrolyte boiling followed by vapor formation is characterized by a slow increase in current, which is explained by heating of the active electrode. Region (III–IV) is the zone of formation of a stable vapor-gas shell (VGS) around the cathode, which explains the sharp decrease in current. At further voltage increase, the breakdown of the VGS and the transition of the system to an unstable state occur [16].

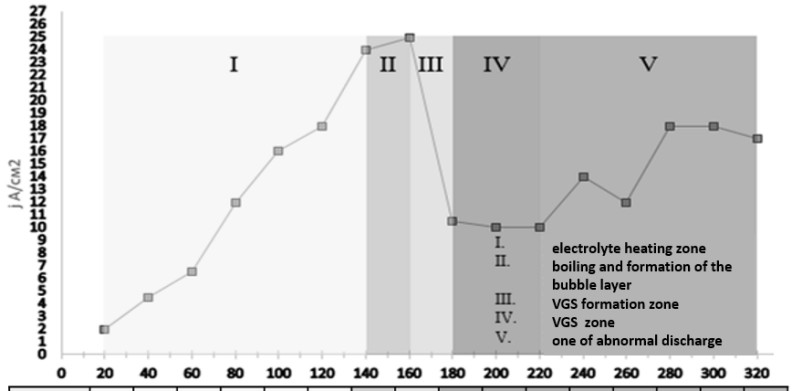

U, B	20	40	60	80	100	120	140	160	**180**	**200**	**220**	240	260	280	300	320
I, A	2	4.5	6.5	12	16	18	24	25	**10.5**	**10**	**10**	14	12	18	18	17

Figure 2. VAC plot of the DEPB process [17]

Experimental studies were carried out in the Research Center “Surface Engineering and Tribology” of S. Amanzholov East Kazakhstan University (Ust-Kamenogorsk, Kazakhstan). The phase composition of materials was determined using X'PertPro X-ray diffractometer (Philips, Netherlands). To reveal the microstructure of the samples we applied chemical etching using 4 % solution of nitric acid (HNO_3) in ethyl alcohol. The microstructure was studied using an Olympus BX53M optical metallographic microscope. The depth hardness was determined using a Vickers microhardness tester (Metolab 502, RF) equipped with a diamond indenter and a load cell up to 1000 g.

The values of coefficient of friction were determined on TRB3 tribometer, where rotation speed was 2 cm per second, radius of the track R = 2 mm; vertical load: 6 N; a 100Cr6 ball of 6 mm diameter was selected as a counterbody.

Results and Discussion

The samples underwent treatment for 5 minutes (№ 1) and 7 minutes (№ 2) with a DC current applied at 290 V, which corresponds to a temperature of 1000 °C. Thermocouples placed in predrilled holes on the surface of the samples were used to monitor their temperature. The experiments were performed in cathode mode, and the key process parameters are presented in Table 1.

Table 1

Table of DEPB modes

	U, V	T, °C	t, min	Electrolyte composition
Sample № 1	290	1000	5	65 % distilled water, 15 % sodium carbonate (Na_2CO_3) and 20 % borax ($Na_2B_4O_7$)
Sample № 2			7	

Figure 3 shows the microstructure of steel 30CrMnSiA before and after DEPB, the main structure of steel is martensite with strengthening structure of boride (light needle-like) and cementite (dark along the

grain boundaries of martensite). The study of steels with martensitic structure revealed their high hardness [18].

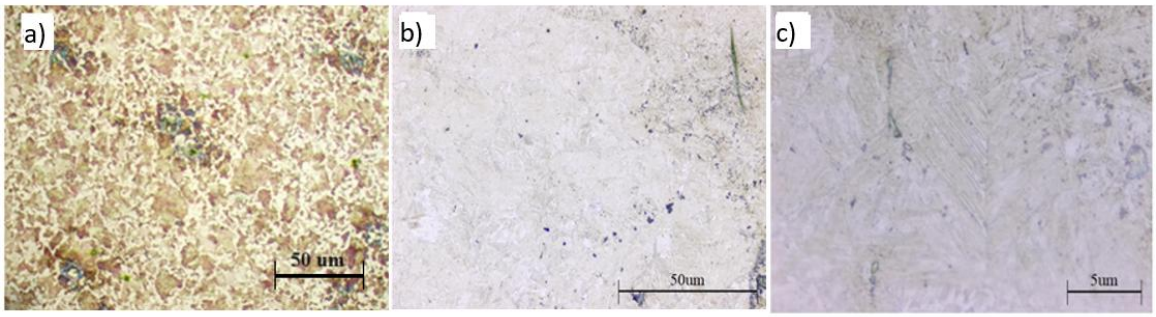

a — microstructure of steel in initial state, magnified in ×50; *b* — microstructure of sample № 1 after DEPB, magnified in ×50; *c* — microstructure of sample № 2 after DEPB, magnified in ×100

Figure 3. Microstructure of steel 30CrMnSiA before and after DEPB

It has been determined that the cross-sectional structure of 30CrMnSiA steel after DEPB has a zonal characteristic: 1 zone of the modified layer, which consists of boride and thermal influence zones, and 2 zone of the matrix — base of the treated material. The analysis of hardness distribution along the thickness of the modified layer after DEPB is particularly interesting. The study of microhardness along the depth showed the presence of a harder surface layer and a less hard layer under it, the extent of which is about 600 μm. The graph in Figure 4 shows that the microhardness gradually decreases from the surface to the middle of the specimen.

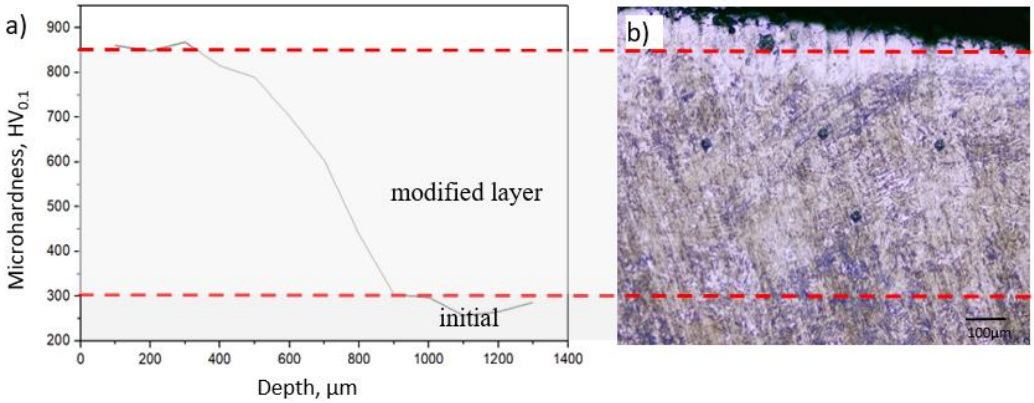

a — microhardness of hardened layers; *b* — microstructure of modified layer

Figure 4. Microhardness of 30CrMnSiA steel by thickness after DEPB (№ 2)

In the near-surface layers microhardness reaches an average of 960 $HV_{0.1}$, then with a smooth transition decreases to an average value of 613 $HV_{0.1}$ in the heat affected zone. In the initial state, the microhardness of the steel is 280±10.4 $HV_{0.1}$.

After DEPB steel 30CrMnSiA underwent significant qualitative and quantitative changes in the steel structure, and, as shown by the studies, the fine structure of steel and phase composition in the near-surface zone of the modified sample and in the transition zone (at a depth of ~650 μm) was significantly different.

As a result of the conducted research, it was found that the material of the near-surface layer is multiphase. However, the main component remains α′-phase (α′-Fe). It should be noted that no ferrite and pearlite grains were found on the sample surface after DEPB (Fig. 4, *b*).

Figure 5 shows the XRD-results of 30CrMnSiA steel before (Fig. 5 *a*) and after (Fig. 5 *b, c*) DEPB. In the initial state, 30CrMnSiA steel consists mainly of α-Fe phase with face-centered cubic lattice (FCC). After the DEPB process, cementite (Fe_3C), boride (Fe_2B), iron oxide (Fe_2O_3) and martensite (α′-Fe) phases are

found in 30CrMnSiA steel. Martensite is formed in the modified steel layer as a result of rapid cooling during the DEPB process. The results of X-ray phase analysis are in agreement with the results of studying the microstructure of 30CrMnSiAsteel after DEPB.

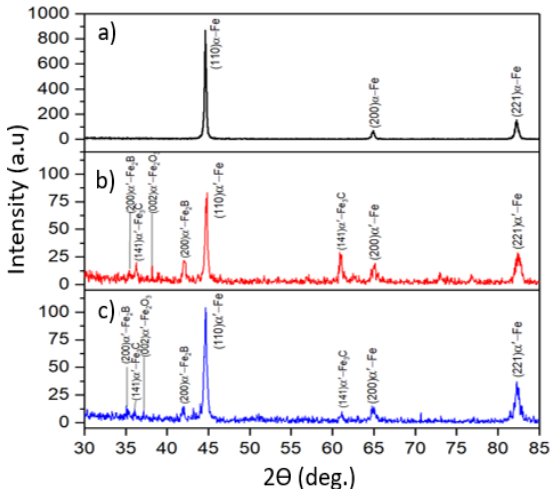

Figure 5. XRD of 30CrMnSiA steel before DEPB (*a*) and after DEPB № 1 (samples *b*) and № 2 (*c*)

During DEPB, 30CrMnSiA steel is exposed to high temperatures produced by electric current. These elevated temperatures may cause the austenite (the stable crystalline form of iron) to transform into more stable phases like martensite and cementite. The structure and properties after DEPB depend primarily on the temperature and duration of the interaction of the electrolyte with the sample surface and the composition of the electrolyte.

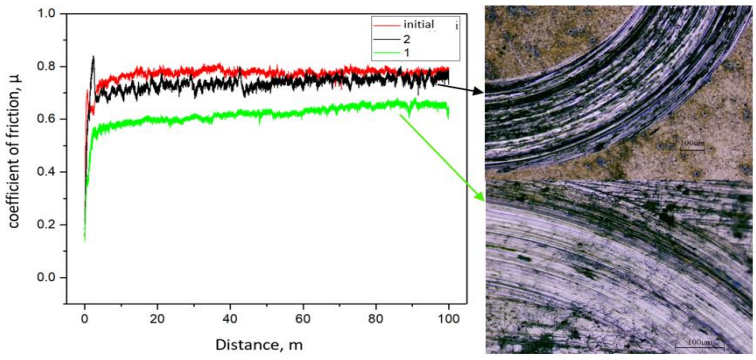

Figure 6: Histogram of sample friction readings and wear trace after tribological testing

The results of tribological tests of boronized steel showed (Fig. 6) that after DEPB, 30CrMnSiA steel has a lower coefficient of friction compared to the original sample. Thus, we can assume that after DEPB the wear resistance of 30CrMnSiA steel increased compared to the original sample.

Table 2

Correlation table of experimental data

	Phase	Microhardness, $HV_{0.1}$	Coefficient of friction, μ
Initial	Ferrite, perlite	280±10.4	0.89
Sample № 1 (5 min)	Cementite, boride, iron oxide and martensite	639.34±16.3	0.68
Sample № 2 (7 min)	Cementite, boride, iron oxide and martensite	659.76±16.7	0.76

Table 2 shows the correlation experimental data that were carried out during the study. From the Table 2, we can see that after DEPB, 30CrMnSiA steel underwent changes affecting not only its microhardness

but also its phase structures. According to the XRD results, martensite, cementite, boride and iron oxide phases are formed on the surface of 30CrMnSiA steel, but the martensite phase (α′-Fe) is the dominant phase in the steel structure following boriding. Also, after DEPB the wear resistance of the samples changed for the better. In the histogram in Figure 6 we see that the friction coefficient of the samples after DEPB is less than that of the original sample.

Conclusions

In this research work, diffusion electrolyte-plasma boriding of 30CrMnSiA steel has been investigated. According to the results, the diffusion electrolyte plasma boriding (DEPB) method can be considered as an effective method for steel modification, which allows different types of treatment depending on the conditions and choice of electrolyte. The DEPB method demonstrates excellent effectiveness in the surface treatment of steels and offers considerable benefits over traditional heat treatment techniques, including energy efficiency, shorter treatment times, and improved environmental safety [19].

It was found that the structure of the cross-section of 30CrMnSiA steel after DEPB is conditionally divided into 3 zones: boride layer, heat affected zone, which together will form a modified layer and the base of the treated material. The structure of the steel cross-section after DEPB is characterized by zonality, with the formation of a modified layer with a thickness of about 650 μm, containing different phases: α′-Fe-martensite, Fe_3C-cementite. The microhardness of 30CrMnSiA steel after DEPB increases 2.5-3 times compared to the initial state due to the formation of hardening phases.

To improve the DEPB plant, additional modules such as electrolyte plasma polishing, which is a finishing module, were retrofitted. The source for EPB was reassembled. The optimum mode for DEPB was selected, including parameters, electrolyte composition, VAC. A nozzle (Fig. 3, *b*) was assembled specially for the modernized DEPB unit.

Acknowledgment

This research is funded by the Science Committee of the Ministry of Science and Higher Education of the Republic of Kazakhstan (Grant No. AP19680473).

References

1 Pantelis D.I. Wear and corrosion resistance of laser surface hardened structural steel / D.I. Pantelis, E. Bouyiouri, N. Kouloumbi, P. Vassiliou, A. Koutsomichalis // Surface and Coatings Technology. — 2002. — Vol. 161 — P. 125–134.

2 Skeeba V.Y Peculiarities of High-Energy Induction Heating during Surface Hardening in Hybrid Processing Conditions / V.Y. Skeeba, V.V. Ivancivsky, N.V. Martyushev // Metals. — 2021. — Vol. 11. — P. 1354.

3 Belkin P.N. Plasma electrolytic hardening of steels: Review / P.N. Belkin, S.A. Kusmanov // Surface Engineering and Applied Electrochemistry. — 2016. — Vol. 52. — P. 531–546.

4 Kumruoglu L.C. Surface modification of medium carbon steel by using electrolytic plasma thermocyclic treatment / L.C. Kumruoglu, D.A. Becerik, A. Ozel, A. Mimaroglu // Mater. Manuf. Process. — 2009. — Vol. 24. — P. 781–785.

5 Kumruoğlu L.C. Surface Modification of AISI 4140 Steel Using Electrolytic Plasma Thermocyclic Treatment / L.C. Kumruoğlu, A. Özel // Mater. Manuf. Process. — 2010. — Vol. 25. — P. 923–931.

6 Rakhadilov B.K. Impact of Volume and Surface Heat Treatment on the Structure and Properties of Steel 30HGSA / B.K. Rakhadilov, R.S. Kozhanova, P. Kowalewski, D.R. Baizhan, Zh.B. Sagdoldina, L.G. Zhurerova, G.U. Yerbolatova // Bulletin of the University of Karaganda – Physics. — 2021. — Vol. 4. — P. 16–24.

7 Rahadilov B.K. Morphological changes in the dislocation structure of structural steel 20GL after electrolytic-plasma hardening of the surface / B.K. Rahadilov, L.G. Zhurerova, Z.B. Sagdoldina, A.B. Kenesbekov, L.B. Bayatanova // J. Surf. Investig. — 2021. — Vol. 15. — P. 408–413.

8 ArslanHafeez M. Nanoindentation-Based Micro-Mechanical and Electrochemical Properties of Quench-Hardened, Tempered Low-Carbon Steel / M. ArslanHafeez, M. Usman, M.A. Arshad, M. AdeelUmer // Crystals. — 2020. — Vol. 10. — P. 508.

9 Ayday A. The effects of overlapping in electrolytic plasma hardening on wear behavior of carbon steel / A. Ayday, D. Kırsever, A.Ş. Demirkıran // Trans. Indian Inst. Met. — 2022. — Vol. 75. — P. 27–33.

10 Dayança A. The cathodic electrolytic plasma hardening of steel and cast iron based automotive camshafts / A. Dayança, B. Karaca, L.C. Kumruoğlu // Acta Phys. Pol. A. — 2017. — Vol. 131. — P. 374–378.

11 Lisiecki A. Study of Optical Properties of Surface Layers Produced by Laser Surface Melting and Laser Surface Nitriding of Titanium Alloy / A. Lisiecki // Materials. — 2019. — Vol. 12. — P. 312.

12 Li W. Influence of Tool and Workpiece Properties on the Wear of the Counterparts in Contact Sliding / W. Li, L. Zhang, C. Wu, Z. Cui, C. Niu // J. Tribol. — 2022. — Vol. 144. — P. 021702.

13 Belkin P.N. Plasma electrolytic saturation of steels with nitrogen and carbon / P.N. Belkin, A.L. Yerokhin, S.A. Kusmanov // Surf. Coat. Technol. — 2016. — Vol. 307. — P. 1194–1218.

14 Kusmanov S.A. Modification of steel surface by plasma electrolytic saturation with nitrogen and carbon / S.A. Kusmanov, Y.V. Kusmanova, A.A. Smirnov, P.N. Belkin // Mater. Chem. Phys. — 2016. — Vol. 175. — P. 164–171.

15 Рахадилов Б.К. Электролитно-плазменная поверхностная закалка низколегированных сталей 65Г и 20ГЛ / Б.К. Рахадилов, Л.Г. Журерова, А.В. Павлов, В.К. Виелеба // Вестник Карагандинского университета. Сер. Физика. — 2016. — № 4(84). — С. 8–13.

16 Rakhadilov B.K. Change in high-temperature wear resistance of high-speed steel by plasma nitriding / B.K. Rakhadilov, L.G. Zhurerova, M. Scheffler, A.K. Khassenov // Bulletin of the University of Karaganda – Physics. — 2018. — № 3(91). — P. 59–65.

17 Сулюбаева Л.Г. Исследование современного состояния и технологических возможностей способа электролитно-плазменной химико-термической обработки сталей / Л.Г. Сулюбаева, Б.К. Рахадилов, Н.Е. Бердімуратов, З.А. Сатбаева // Вестник НЯЦ РК. — 2023. — № 3. https://doi.org/10.52676/1729-7885-2023-3-182-191

18 Baizhan D. Investigation of Changes in the Structural-Phase State and the Efficiency of Hardening of 30CrMnSiA Steel by the Method of Electrolytic Plasma Thermocyclic Surface Treatment / D. Baizhan, B. Rakhadilov, L. Zhurerova, Y. Tyurin, Zh. Sagdoldina, M. Adilkanova, R. Kozhanova // Coatings. — 2022. — Vol. 12. — P. 1696.

19 Khassenov A.K. Electric pulse method of processing cullet / A.K. Khassenov, B.R. Nussupbekov, D.Zh. Karabekova, G.A. Bulkairova, B.U. Shashubai, M.M. Bolatbekova // Bulletin of the University of Karaganda – Physics. — 2022. — Vol. 1. — P. 75–80.

Л.Г. Сулюбаева, Ж. Сагдолдина, Д.Р. Байжан, Н.Е. Бердімуратов, С.Д. Болатов

Диффузиялық электролиттік-плазмалық борлау әдісімен легірленген болаттардың модификацияланған беттерінің құрылымы мен трибомеханикалық қасиеттерінің өзгеруін талдау

Қазіргі уақытта конструкциялық болаттардан бөлшектер жасау кезінде машина жасау саласындағы ең өзекті талаптардың бірі қаттылық пен тозуға төзімділік параметрлерінің болуы. Бұл мәселеге қатысты тиімді шешімдердің бірі диффузиялық-электролиттік-плазмалық борлау әдісі болуы мүмкін, себебі өңдеу барысында болаттың беті бор элементтерімен қанығады, ал бөлшектің өзегі бастапқы күйінде қалады. Бұл жұмыста болаттарды диффузиялық-электролиттік-плазмалық борлау әдісінің технологиялық мүмкіндіктері қарастырылған. 30ХГСА болатты өңдеу диффузиялық-электролиттік-плазмалық борлау қондырғысында жүргізілді. Өңдеу уақыты 5 және 7 минут болды, ал электролит ретінде 15 % кальцинделген сода (Na_2CO_3) және 20 % бураның ($Na_2B_4O_7$) судағы ерітіндісі қолданылды. Анықталғандай, болаттың көлденең қимасының құрылымы диффузиялық-электролиттік-плазмалық борлаудан кейін зоналдық сипатқа ие, ал модификацияланған қабаттың қалыңдығы шамамен 650 мкм. Диффузиялық-электролиттік-плазмалық борлау процесінің нәтижесінде 30ХГСА болатының микроқаттылығы қатайту фазаларының түзілуіне байланысты бастапқы күйімен салыстырғанда 2,5–3 есе артады.

Кілт сөздер: диффузия, электролит, плазма, борлау, құрылым, бетті модификациялау, беті, бура

Л.Г. Сулюбаева, Ж. Сагдолдина, Д.Р. Байжан, Н.Е. Бердимуратов, С.Д. Болатов

Анализ изменения структуры и трибомеханических свойств модифицированных поверхностей легированных сталей методом диффузионного электролитно-плазменного борирования

В настоящее время одним из актуальных требований в сфере машиностроения при изготовлении деталей из конструкционных сталей, являются параметры твердости и износостойкости. Одним из решений этой проблемы может стать диффузионно-электролитно-плазменное борирование. При такой обработке поверхность стальной детали насыщается бором, в то время как сердцевина остается в исходном состоянии. В данной работе рассмотрены вопросы технологических возможностей способа диффузионно-электролитно-плазменного борирования сталей. Была проведена обработка стали 30ХГСА на установке диффузионно-электролитно-плазменного борирования. Продолжительность обработки составляла 5 и 7 минут при использовании в качестве электролита водного раствора 15 % кальцинированной соды (Na_2CO_3) и 20 % буры ($Na_2B_4O_7$). Установлено, что после диффузионно-электролитно-плазменного борирования, структура поперечного сечения стали характеризуется зональностью, с образованием модифицированного слоя толщиной около 650 мкм. В результате

образования упрочняющих фаз после диффузионно-электролитно-плазменного борирования, микротвердость стали 30ХГСА увеличивается в 2,5–3 раза по сравнению с исходным состоянием.

Ключевые слова: диффузия, электролит, плазменное, борирование, структура, модификация поверхности, поверхность, бура

References

1 Pantelis, D.I., Bouyiouri, E., Kouloumbi, N., Vassiliou, P., & Koutsomichalis, A. (2002). Wear and corrosion resistance of laser surface hardened structural steel. *Surface and Coatings Technology*, *161*, 125–134.

2 Skeeba, V.Y., Ivancivsky, V.V., & Martyushev, N.V. (2021). Peculiarities of High-Energy Induction Heating during Surface Hardening in Hybrid Processing Conditions. *Metals*, *11*, 1354.

3 Belkin, P.N., & Kusmanov, S.A. (2016). Plasma electrolytic hardening of steels: Review. *Surface Engineering and Applied Electrochemistry, 52*, 531–546.

4 Kumruoglu, L.C., Becerik, D.A., Ozel, A., & Mimaroglu, A. (2009). Surface modification of medium carbon steel by using electrolytic plasma thermocyclic treatment. *Mater. Manuf. Process*, *24*, 781–785.

5 Kumruoğlu, L.C., & Özel, A. (2010). Surface Modification of AISI 4140 Steel Using Electrolytic Plasma Thermocyclic Treatment. *Mater. Manuf. Process, 25*, 923–931.

6 Rakhadilov, B.K., Kozhanova, R.S., Kowalewski, P., Baizhan, D.R., Sagdoldina, Zh.B., Zhurerova, L.G., & Yerbolatova, G.U. (2021). Impact of Volume and Surface Heat Treatment on the Structure and Properties of Steel 30HGSA. *Bulletin of the University of Karaganda – Physics, 4*, 16–24.

7 Rahadilov, B.K., Zhurerova, L.G., Sagdoldina, Z.B., Kenesbekov, A.B., & Bayatanova, L.B. (2021). Morphological changes in the dislocation structure of structural steel 20GL after electrolytic-plasma hardening of the surface. *J. Surf. Investig, 15*, 408–413.

8 ArslanHafeez, M., Usman, M., Arshad, M.A., & AdeelUmer, M. (2020). Nanoindentation-Based Micro-Mechanical and Electrochemical Properties of Quench-Hardened, Tempered Low-Carbon Steel. *Crystals, 10*, 508.

9 Ayday, A., Kırsever, D., & Demirkıran, A.Ş. (2022). The effects of overlapping in electrolytic plasma hardening on wear behavior of carbon steel. *Trans. Indian Inst. Met.*, *75*, 27–33.

10 Dayança, A., Karaca, B., & Kumruoğlu, L.C. (2017). The cathodic electrolytic plasma hardening of steel and cast iron based automotive camshafts. *Acta Phys. Pol. A*., *131*, 374–378.

11 Lisiecki, A. (2019). Study of Optical Properties of Surface Layers Produced by Laser Surface Melting and Laser Surface Nitriding of Titanium Alloy. *Materials*, *12*, 312.

12 Li, W., Zhang, L., Wu, C., Cui, Z., & Niu, C. (2022). Influence of Tool and Workpiece Properties on the Wear of the Counterparts in Contact Sliding. *J. Tribol., 144*, 021702.

13 Belkin, P.N., Yerokhin, A.L., & Kusmanov, S.A. (2016). Plasma electrolytic saturation of steels with nitrogen and carbon. *Surf. Coat. Technol., 307*, 1194–1218.

14 Kusmanov, S.A., Kusmanova, Y.V., Smirnov, A.A., & Belkin, P.N. (2016). Modification of steel surface by plasma electrolytic saturation with nitrogen and carbon. *Mater. Chem. Phys*., *175*, 164–171.

15 Rahadilov, B.K., Zhurerova, L.G., Pavlov, A.V., & Vieleba, V.K. (2016). Elektrolitno-plazmennaia poverkhnostnaia zakalka nizkolegirovannykh stalei 65G I 20Gl. *Bulletin of the University of Karaganda – Physics,* 4(84), 8–13 [in Russian].

16 Rakhadilov, B.K., Zhurerova, L.G., Scheffler, M., & Khassenov, A.K. (2018). Change in high-temperature wear resistance of high-speed steel by plasma nitriding. *Bulletin of the University of Karaganda – Physics,* 3(91), 59–65.

17 Sulubaeva, L.G., Rakhadilov, B.K., Berdimuratov, N.E., & Satbaeva, Z.A. (2023). Study of the current state and technological capabilities of the method of electrolyte-plasma chemical heat treatment of steels. *Vestnik Natsionalnogo Yadernogo Tsentra Respubliki Kazakhstan — Bulletin of the National Nuclear Center of the Republic of Kazakhstan*, 3 https://doi.org/10.52676/1729-7885-2023-3-182-191

18 Baizhan, D., Rakhadilov, B., Zhurerova, L., Tyurin, Y., Sagdoldina, Zh., Adilkanova, M., & Kozhanova, R. (2022). Investigation of Changes in the Structural-Phase State and the Efficiency of Hardening of 30CrMnSiA Steel by the Method of Electrolytic Plasma Thermocyclic Surface Treatment. *Coatings*, *12*, 1696.

19 Khassenov, A.K., Nussupbekov, B.R., Karabekova, D.Zh, Bulkairova, G.A., Shashubai, B.U., & Bolatbekova, M.M. (2022). Electric pulse method of processing cullet. *Bulletin of the University of Karaganda – Physics, 1*, 75–80.

Information about the authors

Sulyubayeva, Laila — PhD, Associate Professor, Senior Researcher of Scientific Research Center “Surface Engineering and Tribology”, S. Amanzholov East Kazakhstan University, Ust-Kamenogorsk, Kazakhstan; e-mail: lsulyubayeva@gmail.com; ORCID ID: https://orcid.org/0000-0002-1924-1459

Sagdoldina, Zhuldyz — PhD, Associate Professor, Senior Researcher of Scientific Research Center "Surface Engineering and Tribology", S. Amanzholov East Kazakhstan University, Ust-Kamenogorsk, Kazakhstan; e-mail: zh.sagdoldina@gmail.com; ORCID ID: https://orcid.org/0000-0001-6421-2000

Berdimuratov, Nurbol (*corresponding author*) — Leading Researcher of Scientific Research Center "Surface Engineering and Tribology", S. Amanzholov East Kazakhstan University, Ust-Kamenogorsk, Kazakhstan; e-mail: nurbol.ber@gmail.com; ORCID ID: https://orcid.org/0009-0000-6880-6439

Baizhan, Daryn — Senior Researcher of Scientific Research Center "Surface engineering and Tribology", S. Amanzholov East Kazakhstan University, Ust-Kamenogorsk, Kazakhstan, 3rd year PhD, Shakarim University, Semey, Kazakhstan; e-mail: daryn.baizhan1@gmail.com, ORCID: https://orcid.org/0000-0002-9105-3129

Bolatov, Sanzhar — Junior Researcher of Scientific Research Center "Surface engineering and Tribology", S. Amanzholov East Kazakhstan University, Master's student of the 2nd year, Ust-Kamenogorsk, Kazakhstan; e-mail: sanzharbolatov94@gmail.com, ORCID: https://orcid.org/0009-0003-3136-0535

Article
https://doi.org/10.31489/2025PH1/77-88
UDC 621.785

Received: 17.12.2024
Accepted: 28.01.2025

L.G. Sulyubayeva[1], D.B. Buitkenov[1], D.R. Baizhan[1],
N.E. Berdimuratov[1], N.S. Raisov[1*], A.Zh. Zhumabekov[2]

[1]*Research Center Surface Engineering and Tribology, Sarsen Amanzholov East Kazakhstan University, Ust-Kamenogorsk, Kazakhstan;*
[2]*Toraigyrov University, Pavlodar, Kazakhstan*
*(*Corresponding author's e-mail: nurmakhanbetraisov@gmail.com)*

Influence of Thermocyclic Electrolyte-Plasma Treatment on Mechanical Properties of U9 Tool Steel

The article investigates the influence of thermocyclic electrolytic-plasma treatment (EPT) on the mechanical properties of carbon steel U9 tool steel. U9 steel is often used for manufacturing tools working in conditions that do not cause edge heating: woodworking tools, assembly tools, gauges of simple shape and reduced accuracy classes. In this work, thermocyclic electrolytic-plasma treatment was used as a method of improving mechanical properties. This method combines electrochemical reactions and intensive thermal influence, which allows the formation of surface layers with improved characteristics. As a result of the treatment, U9 steel shows a clear division of the microstructure into three zones: hardened layer, transition layer and base metal. The hardened layer, located up to a depth of 400 μm, is characterized by a finely dispersed structure consisting of martensite and bainite with high hardness (1400–1600 $HV_{0.1}$). This layer provides excellent wear resistance and resistance to mechanical stress. The transition layer (400–700 μm) serves as a buffer zone, distributing stresses evenly. It is characterized by a gradual decrease in hardness (800–1200 $HV_{0.1}$) and a change in structure due to a decrease in martensite content. The base metal, deeper than 700 μm, retains the original structure with hardness 400–600 $HV_{0.1}$, which ensures its ductility and durability. The results show that thermocyclic EPT significantly improves the performance properties of U9 steel by creating a functionally gradient structure. The technology is energy efficient and can be widely used in mechanical engineering and other industries where high mechanical characteristics of materials are required.

Keywords: heat treatment, thermocyclic electrolytic-plasma treatment, electric discharge phenomena, U9 tool steel, microstructure, micro hardness

Introduction

In conditions when traditional materials in mechanical engineering and equipment manufacturing exhaust their capabilities and do not meet the growing requirements of modern technologies, the introduction of innovative approaches and technologies becomes critical. Development and application of new materials and processing methods are necessary to improve the performance, strength and durability of assemblies and mechanisms. One of the key solutions is the modernization of technological processes aimed at improving the reliability and life of parts. This includes the use of advanced methods such as chemical-thermal treatment, thermocyclic hardening, anodic-spark oxidation and electrolyte-plasma technologies [1–6].

Electrolyte-plasma treatment (EPT) is a method that combines electrochemical reactions and thermal effects, creating optimal conditions for phase transformations and modification of the metal surface layer. Thanks to the combination of intensive heating and rapid cooling, this process ensures the formation of a finely dispersed structure including high-strength phases. This significantly improves the mechanical properties of the material, such as hardness, wear resistance and resistance to fatigue loads. The application of thermocyclic regimes in EPT promotes the accumulation of structural changes, which is achieved through multiple phase transformations and regulation of temperature parameters [7].

The choice of thermocyclic treatment parameters, such as temperature, number of cycles, heating and cooling rates, allows the method to be adapted to the specific requirements of industrial production. This makes electrolyte-plasma treatment not only highly efficient but also energy-efficient, which is especially important for modern manufacturing processes. Moreover, the possibility of combining EPT with other treatment and modification methods opens new horizons for complex improvement of materials performance [8].

The purpose of this study is to investigate the effect of thermocyclic electrolytic-plasma treatment on the mechanical properties of U9 tool steel. The work is aimed at detailed analysis of changes in microstructure, hardness and strength characteristics of the material after treatment. The results obtained will make it

possible to evaluate the potential of this method to improve the reliability and durability of parts used in mechanical engineering and equipment manufacturing.

Materials and methods of research

The object of the study was U9 carbon tool steel. The choice of the research material is justified by the fact that this steel is widely used in mechanical engineering, power engineering and other industries, where such properties as strength, wear resistance, ability to maintain mechanical characteristics under high loads are important [9]. U9 carbon tool steel has high hardness, which makes it indispensable in the production of cutting and measuring tools, as well as elements of stamping systems. Knives, cutters, drills, calipers, files, punches and dies are made of this steel. Chemical composition of U9 tool steel according to GOST 1435-99 is presented in Table 1.

Table 1

Chemical composition of U9 tool steel

C	Si	Mn	Ni	S	P	Cr	Cu	V	Mo
0.85–0.94	0.17–0.33	0.17–0.33	until 0.25	until 0.028	until 0.03	until 0.2	until 0.25	–	–

Samples were prepared on a Metapol-2000P surface grinding machine with subsequent polishing using diamond pastes. At least 5 samples were used for each batch for reliability of measurement results.

The microstructure of the samples was revealed by chemical etching method using 4 % nitric acid solution (HNO_3) in ethyl alcohol. The microstructure of initial and treated steels was studied by optical microscopy on Olympus BX53P microscope in reflected light at light field and scanning electron microscopy (SEM) on "TESCAN VEGA 4" microscope at magnifications ×4000, ×10000. The imaging was carried out in the regimes of secondary and backscattered electrons.

To determine the hardness by depth of the samples we used a hardness micro-measurer Metolab 502 equipped with a four-sided diamond Vickers pyramid with a square base and angle $\alpha = 136°$ between opposite faces at the apex in strict compliance with the requirements of GOST 9450-76 for the Vickers method. The diamond indenter under the load $F = 1$N was pressed in perpendicularly and held under the load for 10 s. The diagonals of the indentation $d1$, $d2$ were measured.

The study of electro-discharge phenomena in the "metal-electrolyte" system. Tests were carried out to determine the values of hydrogen ion activity (pH), as well as the values of the electric potential of electrolytes, and the molar concentrations of electrolytes were calculated.

The electrolytes were prepared on the basis of soda ash (Na_2CO_3) diluted with water (H_2O), the equation reaction is presented in formula (1).

$$Na_2CO_3 + H_2O \rightarrow HCO_3^- + 2Na^+ + OH^- \quad (1)$$

As a result of a chemical reaction, a salt solution formed by a strong base and a weak acid gives an alkaline reaction (excess OH ions). The end products of the reaction are hydrogen carbonate (carbonic acid), sodium ions and hydroxide ions.

Two types of electrolyte based on sodium carbonate were prepared to study the properties, with a difference in its content in solution, namely for the first electrolyte the mass fraction was 15 % (No. 1), for the second 10 % (No. 2).

For preparation of electrolyte No. 1, 3 kg of Na_2CO_3 and 17 kg of distilled water were used. For electrolyte No. 2, 4 kg of Na_2CO_3 and 16 kg of distilled water.

The concentration of electrolytes was determined and experimental work was carried out to measure pH, specific conductivity and mass concentration of dissolved solute. Measurement of pH was carried out on laboratory ionometer I-160MI (production of Russia) according to GOST 8.120-99 "State verification scheme for pH measuring instruments". The instrument consists of primary measuring transducers — electrode system and temperature sensor (hereinafter — temperature sensor), secondary measuring transducer (hereinafter — transducer) and a set of accessories for measurements [10]. The general view of the transducer and its design elements are shown in Figure 1.

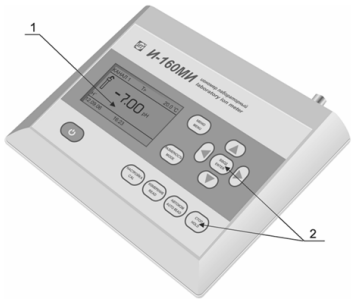

1 — Matrix display; *2* — Controls

Figure 1 Converter I-160MI

According to the methodology, before measurements, the electrodes are calibrated in buffer solutions with different pH values. No. 1 buffer solution pH = 1.65, No. 2 pH = 3.56, No. 3 pH = 9.18. Between each buffer solution and just before the measurements, the electrodes are cleaned from reagent residues with a stream of distilled water. Quality control of electrode cleaning from buffer solution residues is performed by measuring the pH value of distilled water. The pH value on the electrode surface should correspond to a neutral value (about 7) to exclude buffer solution residues. Once the electrodes have been calibrated, direct measurements are allowed. The electrodes are placed before the measuring part is immersed in the electrolyte for an average of 3 minutes. After that the display shows the finished values. Values were obtained for the initial electrolyte before TEPT, as well as after the 1st, 2nd, 3rd cycles. The results of pH, electrode potential measurements are presented in Table 2.

Calculations of molar concentration of electrolytes were carried out using formula 2. The data were obtained for 50 ml of electrolyte, which subsequently served as samples for the study of pH values, potentials.

$$C = \frac{m}{M \times V}, \tag{2}$$

where m — mass of sodium carbonate [g]; M — molar mass of sodium carbonate [g/mol]; V — volume of solution [l].

Thermocyclic electrolyte-plasma treatment of samples of steel U9 was carried out on the modernized unit in the Research Center “Surface Engineering and Tribology”. The modernized unit includes several key modules, which important elements are synchronization unit, microprocessor unit, power supply unit, power leads unit and control unit (Fig. 2 *A*). The synchronization unit is responsible for phasing and ensuring correct communication between the supply network and the thyristors. The microprocessor unit allows the thermal cycling parameters to be set, operating regimes to be set and the entire system to be automatically controlled. The power supply unit converts the input voltage to the necessary levels to support the operation of all other modules. The power output block provides high-power currents for processing steel samples, and the control block synchronizes the thyristors’ actions by switching them on and off at the right moments.

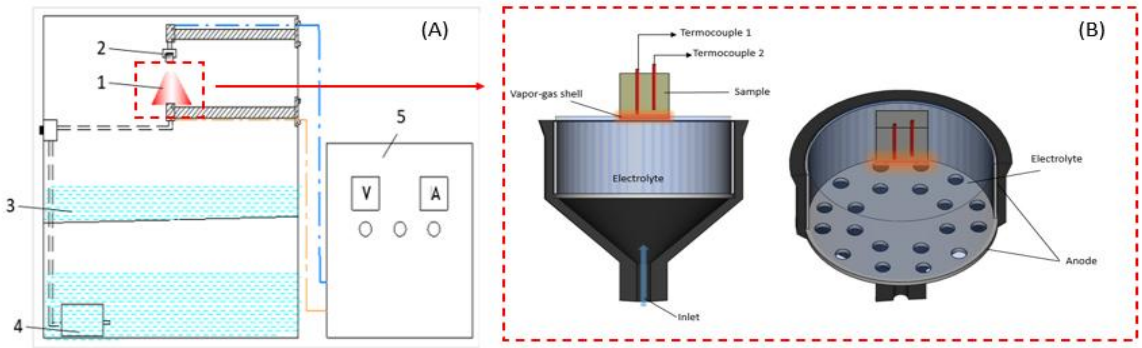

(*A*) Image of the unit for diffusion-electrolyte-plasma boriding:
1 — anode; *2* — sample; *3* — electrolyte bath; *4* — pump; *5* — power supply;
(*B*) Scheme of thermocouple placement in the surface layer of the sample

Figure 2. Schematic diagram of the general view of the EPT unit

During the experimental work, temperature measurements on the sample surface were carried out. For this purpose, thermocouples made by the method of natural thermal junction were used. Thermocouples were placed in two layers of the sample at a depth of 1.0 and 2.0 mm from the heated surface, which allowed recording temperature changes at different levels of the material (Fig. 2 *B*). When calculating the temperature at the sample surface, it was assumed that the entire heat flux propagates from the surface into the depth of the material. This assumption allows us to consider the thermal process unidirectional and take into account the influence of only those factors that are associated with energy transfer to the depth of the sample, without taking into account possible losses to radiation or convection. This approach simplifies the analysis and allows for a more accurate determination of the surface temperature [7, 8].

The essence of the thermocyclicelectrolyte-plasma treatment process is as follows. At low voltages (150 V), a classical electrochemical process is observed in an electrochemical cell containing an aqueous electrolyte solution. At higher voltages (300 V), an intensive electrode outgassing begins, leading to the formation of a near-electrode gas-liquid layer. As the voltage increases, the packing density of gas bubbles in the near-electrode gas-liquid layer increases, and the total cross-sectional area of electrolyte bridges between them decreases. As a result of Joule heat release, the electrolyte temperature in these bridges reaches the boiling point. During the transition from bubble boiling to film boiling, a thin (50–100 μm) vapor-gas shell (VGS) consisting of water vapor, activated OH^-, H^+ and Na^+ and CO_3^{2-} ions, which are part of the electrolyte, appears around the product immersed in the electrolyte. The electric field strength in VGS reaches 10^4–10^5 V/cm. At a temperature of about 100 °C, such a voltage can cause ionization of vapors, as well as emission of ions and electrons necessary to maintain a stationary electric discharge. And as a result, electrolyte plasma is formed [11]. Sodium carbonate (Na_2CO_3) solution was used as heating and cooling source.

A hardness tester “METOLAB 502” (GOST 6507-1-2007) was used to test the microhardness by the Vickers method. The indenter used for measurement was a diamond pyramid with an angle between two faces of 136°. The following regime was chosen to measure hardness by Vickers method: load 0.1 kg, load time 10 sec.

The study of surface microstructure and analysis of morphology of cross sections of coatings were carried out using scanning electron microscopy (SEM) on the equipment VEGA4 TESCAN in D. Serikbayev East Kazakhstan Technical University.

Results and discussion

The results of tests in the “metal-electrolyte” system are presented in Table 2.

Table 2

Results of electrochemical studies of TEPT electrolytes

	Cycle TEPT	1-Electrolyte composition: 15 % Na_2CO_3 + 85 % water	2-Electrolyte composition: 10 % Na_2CO_3 + 90 % water
Specific conductivity *s*, μSm/cm	1	83000	69000
	2	63000	43000
	3	51860	26400
Index, pH	1	10.759	10.675
	2	10.728	10.561
	3	10.778	10.620
Electrode potential, *E*°, mV	1	–223.6	–231.4
	2	–222.4	–227.7
	3	–223.6	–229.1
Molar concentration, *C*, mol/L	1	0.0047	0.0035
	2	0.0049	0.0036
	3	0.0043	0.0031

The initial pH values for electrolyte No. 1, No. 2 were 10.759 and 10.691, respectively. As can be seen from the data in Table 2, decrease in salt concentration and increase in water content decreases the pH value of electrolyte. The result of electrode potential measurement for the two electrolytes showed negative value, namely for electrolyte No. 1 –223.6 and for electrolyte No. 2 –231.4. This is due to the high concentration of OH^- ions in the electrolyte, which reduce the concentration of hydrogen ions and make the electric potential relative to the standard hydrogen electrode negative. As the pH value of the solution increases, the electrode

potential becomes more negative. This is an expected pattern because an increase in pH indicates a decrease in the concentration of H^+ ions, which shifts the equilibrium of the electrochemical reaction. According to the results of electrolyte concentration calculations, a slight change in molar concentrations is observed before and after several cycles [12–14].

Table 3 presents the results of electrolyte-plasma treatment experiments on U9 steel conducted in sodium carbonate (Na_2CO_3) solutions with 15 % and 10 % concentration. During the experiments, the effects of parameters such as voltage, current strength, heating duration and electrolyte concentration on steel surface temperature, current density and temperature changes of the electrolyte were studied. Using a 15 % Na_2CO_3 solution, the electrolyte temperature was 35–36 °C before heating and reached 39 °C after the third cycle. In the first cycle, at a voltage of 300 V, a current of 100 A and a heating time of 2 seconds, the steel surface temperature reached 374 °C at a current density of 33.3 A/cm². In subsequent cycles, despite short heating periods (300 V for 1–2 seconds), the surface temperature increased significantly, reaching 800 °C in the second cycle and 1000 °C in the third cycle. The intermediate voltage reduction to 150 V for 3 seconds helped to stabilize the process and to distribute the heat evenly, preventing overheating of the steel surface.

For the 10 % Na_2CO_3 solution, similar trends were observed, but with a lower heating intensity. The initial electrolyte temperature was slightly lower (34.9–36.7 °C) and the current density was 13.3 A/cm², which was about 2.5 times lower than that of the 15 % solution. The steel surface temperature reached 350 °C in the first cycle, 700 °C in the second cycle, and a maximum value of 1200 °C in the third cycle. Increasing the heating duration (up to 5 seconds at 300 V) combined with intermediate pauses at 150 V provided smoother surface heating. This makes the 10 % solution suitable for applications where a more gradual and delicate temperature rise is required without the risk of significant thermal stresses.

Table 3

Parameters of electrolyte-plasma treatment of U9 steel in Na_2CO_3 solutions with different concentrations

Steel	Electrolyte	*T*, °C	*U*, V	*t*, s	*I*, A	Cycle	*T*, °C Steel	*J*, A/cm²
U9	10 % Na_2CO_3	before 36.7	300	5	40	1	350	13.3
		after 37.4	150	5	9			3
			300	4	40			13.3
			150	5	9			3
		before 34.9	300	5	40	2	700	13.3
		after 36.3	150	5	9			3
			300	4	40			13.3
			150	5	9			3
		before 35.6	300	5	40	3	1200	13.3
		after 37.3	150	5	9			3
			300	4	40			13.3
			150	5	9			3
	15 % Na_2CO_3	before 36	300	2	100	1	374	33.3
		after 36.6	150	3	60			20
			300	1	100			33.3
			150	3	60			20
		before 35	300	2	100	2	800	33.3
		after 36.3	150	3	60			20
			300	1	100			33.3
			150	3	60			20
		before 35	300	2	100	3	1000	33.3
		after 39	150	3	60			20
			300	1	100			33.3
			150	3	60			20

Figure 3 shows the results of studies that were conducted to investigate the effect of electrolyte-plasma treatment on the microstructure and mechanical properties of U9 steels. The linear decrease in hardness with depth is associated with the appearance of zonal structure after TEPT. The highest hardness was shown by the samples processed in the mode of 3 cycles for both electrolyte compositions. Also the smallest difference for 3 cycles showed the samples treated with TEPT using the first electrolyte composition (15 % Na_2CO_3). In

further studies the samples hardened in the first electrolyte composition were used. In the dissertation work the author Z.A. Satbaeva gives similar data on the dependence of microhardness on the depth of hardened layer for steel U10. In this work, the dependence of hardness decreases with deepening into the hardened material [15].

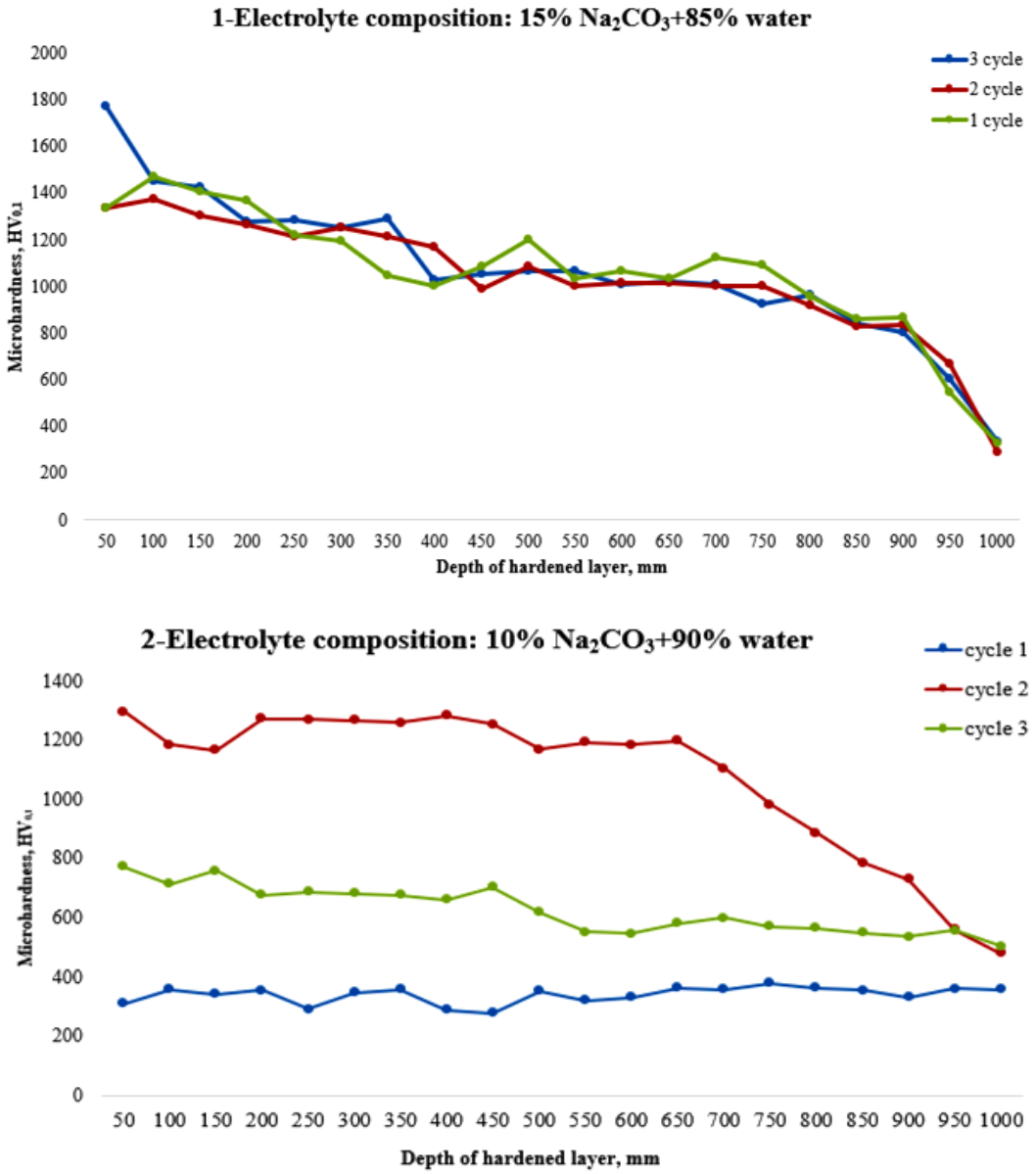

Figure 3. Dependence of microhardness of U9 steels on regimes of electrolyte-plasma treatment and electrolyte concentration

Figure 4 shows the results of electrolyte-plasma treatment of U9 steel in 10 % Na_2CO_3 solution at regime (cycle) No. 1. The microstructure of the material is clearly divided into three zones: hardened layer, transition layer and base metal. The hardened layer, located up to a depth of about 400 μm, shows a finely dispersed structure consisting of martensite and bainite, which provides a high hardness of the material at 1400–1600 $HV_{0.1}$. This layer is formed under the influence of intense heating and rapid cooling, resulting in phases with high strength. This structure provides a significant increase in the wear resistance of the surface, making it suitable for high mechanical stresses.

The transition layer, located at a depth of 400 μm to 700 μm, is characterized by a gradual change in the material structure. In this zone there is a decrease in hardness to the level of 800–1200 $HV_{0.1}$, which is associated with a decrease in thermal effects. Here, pre-eutectoid ferrite is isolated, which forms a mesh along grain boundaries, and the structure acquires a multigrain character. Slow cooling in this region favors the

preservation of fine phases, but the martensite content decreases, which leads to a decrease in strength properties [15, 16]. The transition layer plays an important role as a buffer zone, evenly distributing mechanical stresses between the hardened zone and the base metal, preventing abrupt changes in material properties.

In the base metal zone, deeper than 700 μm, the structure returns to the original structure. Here, an increase in ferrite content is noticeable both at grain boundaries and within them. Microhardness in this zone decreases significantly to 400–600 $HV_{0.1}$, indicating the recovery of properties characteristic of the base metal. This zone is practically not exposed to heat, and its properties correspond to the initial mechanical characteristics of the material. The microhardness graph clearly demonstrates a sharp decrease in hardness with increasing depth, starting from the hardened layer and moving to the base metal.

Thus, electrolyte-plasma treatment of U9 steel forms a high-strength hardened layer with a smooth transition to the transition zone and the base metal.

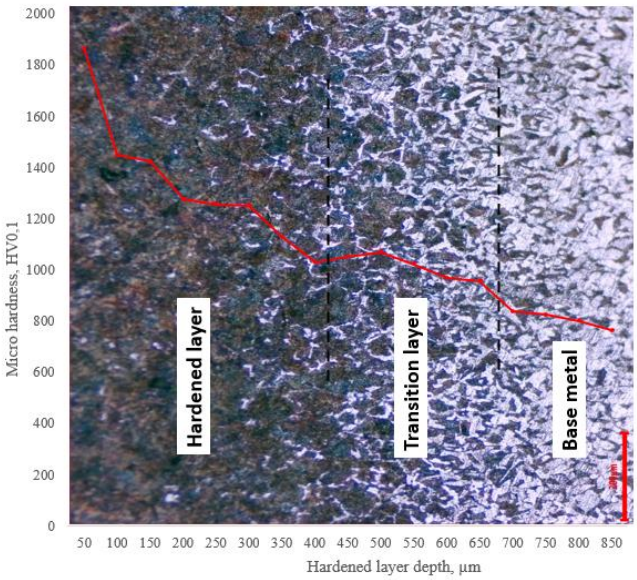

Figure 4. Microstructure and microhardness distribution of U9 steel after electrolyte-plasma treatment (regime No. 1, 15 % Na_2CO_3)

Figure 5 shows the microstructure of U9 steels after treatment with 15 % electrolyte, in three different regimes (No. 1, No. 2, No. 3), which allows us to draw conclusions about the influence of thermal conditions on the formation of structure and mechanical properties of materials. U9 steel, which has high carbon content, in regime No. 1 shows a microstructure mainly consisting of finely dispersed martensite, which confirms its quenched state and provides the highest hardness among all three regimes. In regime No. 2, the structure includes both martensite and bainite due to the milder cooling conditions. This results in intermediate properties between the quenched state and the slow cooling state. In regime No. 3, the microstructure of U9 steel is represented by ferrite and pearlite, which is characteristic of slow cooling. This leads to a significant decrease in hardness and return of the material to a state close to the initial.

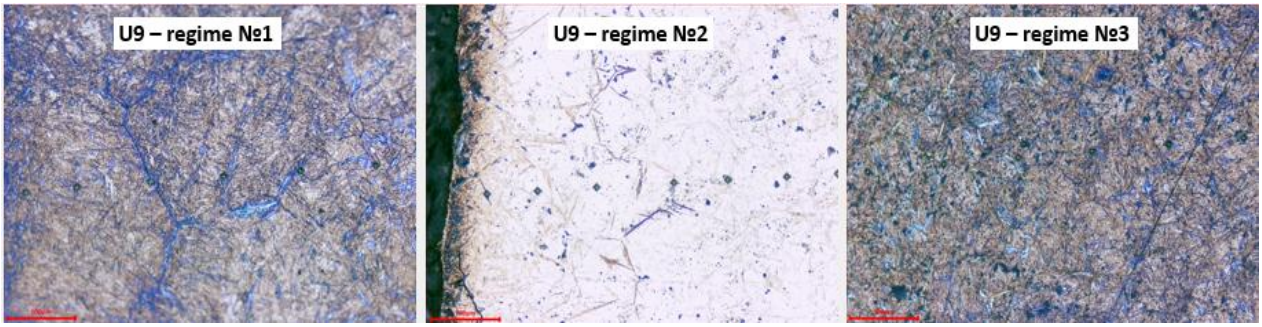

Figure 5. Cross-sectional microstructure of U9 steels after EPT in regimes No. 1, No. 2 and No. 3

To study in detail the structure of U9 steel after electrolyte-plasma treatment, the studies were carried out using scanning electron microscopy (SEM). The results of the analysis confirmed the presence of clearly defined three zones, each characterized by unique microstructure and mechanical properties (Fig. 6). The hardened layer, located at a depth of up to 400 μm, is formed under the influence of intense thermal heating and rapid cooling, resulting in the formation of finely dispersed phases such as martensite and bainite. This structure provides high hardness of the material, reaching 1400–1600 $HV_{0.1}$, which makes it extremely wear-resistant and suitable for high mechanical stresses. The micrographs obtained under magnification clearly show that the martensitic structure has a needle-like character, which confirms its high strength and stiffness. The transition layer, located at a depth of 400 μm to 700 μm, shows changes in the microstructure as it moves away from the hardened zone. In this region, a decrease in thermal stress is observed, leading to a decrease in martensite content and a gradual increase in the proportion of pre-eutectoid ferrite. Slow cooling in the transition zone favors the preservation of finely dispersed phases, but the overall strength of the material is lower here compared to the hardened layer. The transition layer plays a key role as a buffer zone, preventing abrupt changes in mechanical properties between the high-strength surface and the lower-strength base metal. The base metal deeper than 700 μm is virtually unaffected by heat during machining. Its structure reverts to the initial state characteristic of U9 steel and includes ferrite and pearlite. In micrographs, the base metal is characterized by the presence of large ferrite grains located both along the grain boundaries and inside the grains. The hardness in this zone is much lower, varying between 400–600 $HV_{0.1}$, which corresponds to the initial mechanical characteristics of the material. This region retains the ductility and toughness characteristic of the initial state of the steel and plays an important role in preventing brittleness of the structure as a whole. Thus, electrolyte-plasma treatment allows the creation of a functionally graded structure consisting of three zones with different mechanical properties: a high-strength hardened layer, a transition layer and the base metal. This distribution of properties ensures high operational reliability of the material, improves its wear resistance and resistance to mechanical loads.

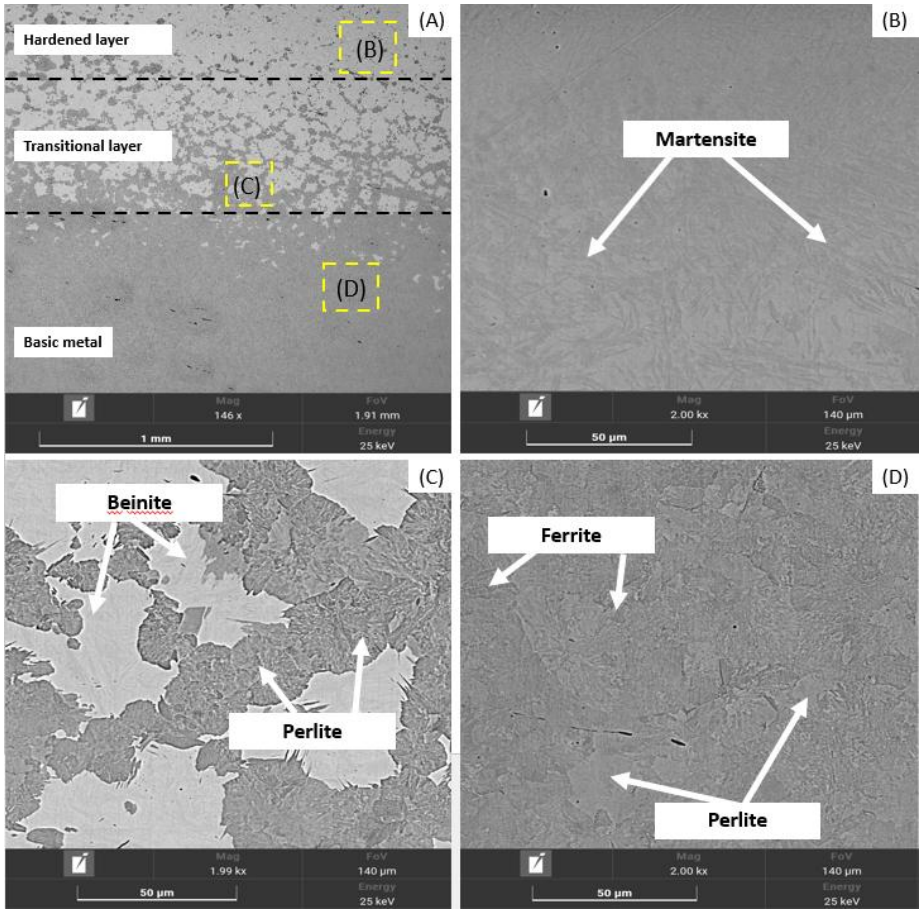

Figure 6. Microstructure of different zones of U9 steel after electrolytic-plasma treatment (regime No. 1)

Conclusion

Thus, according to the results obtained in this article, the following main findings and conclusions were made:

– the electrode potential becomes more negative as the pH value of the solution increases. According to the results of electrolyte concentration calculations, a slight change in molar concentrations is observed before and after several cycles.

– for the 10 % Na_2CO_3 solution, a decrease in heating intensity was observed. The initial electrolyte temperature was slightly lower (34.9–36.7 °C) and the current density was 13.3 A/cm², which is about 2.5 times lower than that of the 15 % solution. This makes the 10 % solution suitable for applications where a more gradual and delicate temperature rise is required without risks of significant thermal stresses.

– electrolytic-plasma treatment of U9 steel in 10 % Na_2CO_3 solution forms a hardened layer (up to 400 μm) with finely dispersed martensite and bainite structure and hardness of 1400–1600 $HV_{0.1}$, providing high wear resistance. The transition layer (400–700 μm) serves as a buffer, reducing hardness to 800–1200 $HV_{0.1}$ and evenly distributing stresses. In the base metal zone (deeper than 700 μm), the structure returns to its original structure with a hardness of 400–600 $HV_{0.1}$. The method creates a strong surface layer and a smooth transition to the basic material properties.

Acknowledgments

This research is funded by the Science Committee of the Ministry of Science and Higher Education of the Republic of Kazakhstan (Grant No. BR24992879).

References

1 Kusmanov S. Increasing Hardness and Wear Resistance of Austenitic Stainless Steel Surface by Anodic Plasma Electrolytic Treatment / T. Mukhacheva, I. Tambovskiy, A. Naumov, R. Belov, E. Sokova, I. Kusmanova // Metals. — 2023. — Vol. 13. — P. 872.

2 Belkin P.N. Plasma Electrolytic Saturation of Steels with Nitrogen and Carbon / P.N. Belkin // Critical Reviews in Solid State and Materials Sciences. — 2011. — Vol. 36(3). — P. 174–190.

3 Aliofkhazraei M. Nano-Fabrication by Cathodic Plasma Electrolysis / A.R. Aghdam, P. Gupta // Critical Reviews in Solid State and Materials Sciences. — 2011. — Vol. 36(3). — P. 174–190.

4 Meletis E.I. Electrolytic plasma processing for Cleaning and Metal coating of Steel Surface / X. Nie, F.L. Wang, J.C. Jiang // Surface and Coatings Technology. — 2002. — Vol. 150. — P. 246–256.

5 Kusmanov S.A. Anode plasma electrolytic nitrohardening of medium carbon steel / A.A. Smirnov, Yu.V. Kusmanova, P.N. Belkin // Surface and Coatings Technology. — 2015. — Vol. 269. — P. 308–313.

6 Смирнов А.А. Повышение коррозионной стойкости и износостойкости стали 45 с помощью анодного электролитно-плазменного азотирования / А.А. Смирнов, С.А. Силкин, П.Н. Белкин, И.Г. Дьяков, В.С. Севостьянова, С.А. Кусманов // Изв. вузов. Химия и хим. технолология. — 2017. — Т. 60. — Вып. 1. — С. 81-86.

7 Dautbekov M.K. A Technology for Making Detonation Coatings on Power Equipment Parts Made of Grade 12Kh1MF Steel / B.K. Rakhadilov, L.G. Zhurerova, D.N. Kakimzhanov, S.L. Elistratov, T.A. Segeda // Thermal Engineering. — 2022. — Vol. 69(12). — P. 989–995.

8 Baizhan D. Investigation of Changes in the Structural-Phase State and the Efficiency of Hardening of 30CrMnSiA Steel by the Method of Electrolytic Plasma Thermocyclic Surface Treatment / D. Baizhan, B. Rakhadilov, L. Zhurerova, Y. Tyurin, Z. Sagdoldina, M. Adilkanova, R. Kozhanova // Coatings. — 2022. — Vol. 12(11). — P. 1996.

9 Rakhadilov B.K. Study of the VAC of the EPCTT process with varying electrode parameters / B.K. Rakhadilov, N.E. Berdimuratov, L.G. Zhurerova, L.B. Bayatanova, Sh.R. Kurbanbekov, Z.A. Satbayeva // Bulletin of the University of Karaganda-Physics. — 2023. — Vol. 3(111). — P. 136–142. DOI: https://doi.org/10.31489/2023PH3/136-142.

10 Zhou L. Additive Manufacturing: A Comprehensive Review / L. Zhou, J. Miller, J. Vezza, M. Mayster, M. Raffay, Q. Justice, Z. Al Tamimi, G. Hansotte, L.D. Sunkara, J. Bernat // Sensors. — 2024. — Vol. 24(6). — P. 2668. DOI: https://doi.org/10.3390/s24092668.

11 Belkin P.N. Plasma electrolytic saturation of steels with nitrogen and carbon / P.N. Belkin, A.L. Yerokhin, S.A. Kusmanov // Surf. Coat. Technol. — 2016. — Vol. 307. — P. 1194–1218.

12 Kusmanov S.A. Modification of steel surface by plasma electrolytic saturation with nitrogen and carbon / S.A. Kusmanov, Y.V. Kusmanova, A.A. Smirnov, P.N. Belkin // Mater. Chem. Phys. — 2016. — Vol. 175. — P. 164–171.

13 Zhan S. Cathodic Discharge Plasma in Electrochemical Jet Machining: Phenomena / S. Zhan, Z. Lyu, B. Dong, W. Liu, Y. Zhao // Mechanism and Characteristics. Int. J. Mach. Tools Manuf. — 2023. — Vol. 187. — P. 104015. DOI: https://doi.org/10.1016/j.ijmachtools.2023.104015.

14 Gupta P. Plasma Formation and Material Removal Characteristics in Microwave-Metal Discharge-Based Machining of AISI 304 Stainless Steel. J. Manuf / P. Gupta, A.K. Sharma, I. Singh. // Process. — 2024. — Vol. 124. — P. 1159–1179. DOI: https://doi.org/10.1016/j.jmapro.2024.06.069.

15 Сатбаева З.А. Структурообразование в легированных сталях при электролитно плазменном поверхностном упрочнении: дис. ... д-ра философии (PhD) : 6D060400 — Физика / З.А. Сатбаева. — Усть-Каменогорск, 2022. — 119 с.

16 Tang W. Experimental Investigation of Discharge Phenomena in Electrochemical Discharge Machining Process / W. Tang, Y. Zhu, X. Kang, C. Mao // Micromachines. — 2023. — Vol. 14 — P. 367. DOI: https://doi.org/10.3390/mi14020367.

17 Asmael M. A Review on Recent Achievements and Challenges in Electrochemical Machining of Tungsten Carbide / M. Asmael, A. Memarzadeh // Archives of Advanced Engineering Science. — 2023. — Vol. 2(1). — P. 1–23. DOI: https://doi.org/10.47852/bonviewaaes3202915.

Л.Г. Сулюбаева, Д.Б. Буйткенов, Д.Р. Байжан,
Н.Е. Бердімуратов, Н.С. Райсов, А.Ж. Жумабеков

У9 құралдық болаттың механикалық қасиеттеріне термоциклдік электролитті-плазмалық өңдеудің әсері

Мақалада термоциклдік электролитті-плазмалық өңдеудің (ЭПӨ) У9 көміртекті құралдық болаттың механикалық қасиеттеріне әсері қарастырылған. У9 болаты ағаш өңдеу құралдары, слесарлық-монтаждық аспаптар, қарапайым пішінді калибрлер және дәлдік кластарын төмендетуде жиектерін қыздырмайтын жағдайларда жұмыс істейтін құралдарды өндіру үшін кеңінен қолданылады. Осы жұмыста механикалық қасиеттерді жақсарту әдісі ретінде термоциклдік электролитті-плазмалық өңдеу пайдаланылды. Бұл әдіс электрхимиялық реакциялармен қарқынды термиялық әсерді біріктіріп, жақсартылған сипаттамалары бар беттік қабаттардың пайда болуына мүмкіндік береді. Өңдеу нәтижесінде У9 болаты микроқұрылымның үш аймаққа анық бөлінуін көрсетеді: берiктелген қабат, өтпелі қабат және негізгі металл. 400 мкм тереңдікте орналасқан беріктендірілген қабат ұсақдисперсті құрылыммен сипатталады. Ол мартенсит пен бейниттен тұрады, қаттылығы жоғары (1400–1600 $HV_{0{\cdot}1}$). Бұл қабат жоғары тозуға төзімділікті және механикалық жүктемелерге беріктікті қамтамасыз етеді. 700 мкм тереңдікте орналасқан өтпелі қабат кернеулерді біркелкі тарататын буферлік аймақ қызметін атқарады. Ол қаттылықтың бірте-бірте төмендеуімен (800–1200 $HV_{0{\cdot}1}$) және мартенсит құрамының төмендеуіне байланысты құрылымның өзгеруімен сипатталады. Тереңдігі 700 мкм-ден асатын негізгі металл 400–600 $HV_{0{\cdot}1}$ қаттылығымен өзінің бастапқы құрылымын сақтайды, бұл оның икемділігі мен ұзақ мерзімділігін қамтамасыз етеді. Алынған нәтижелер ЭПӨ термоциклдік функционалды градиент құрылымын жасай отырып, У9 болатының эксплуатациялық қасиеттерін айтарлықтай жақсартатынын көрсетеді. Бұл технология энергия тиімділігі тұрғысынан үнемді және машина жасауда және материалдардың жоғары механикалық сипаттамаларын қажет ететін басқа да салаларда кеңінен қолданылуы мүмкін.

Кілт сөздер: термоөңдеу, термоциклдік электролитті-плазмалық өңдеу, электр разрядтық құбылыстар, У9 құралдық көміртекті болаты, микроқұрылым

Л.Г. Сулюбаева, Д.Б. Буйткенов, Д.Р. Байжан,
Н.Е. Бердимуратов, Н.С. Райсов, А.Ж. Жумабеков

Влияние термоциклической электролитно-плазменной обработки на механические свойства инструментальной стали У9

В статье исследуется влияние термоциклической электролитно-плазменной обработки (ЭПО) на механические свойства инструментальной углеродистой стали У9. Сталь У9 широко используется для изготовления инструментов, работающих в условиях, не вызывающих разогрева кромки, таких как инструмент для обработки дерева, слесарно-монтажный инструмент, калибры простой формы и пониженных классов точности. В данной работе методом улучшения механических свойств используется термоциклическая электролитно-плазменная обработка. Этот метод объединяет электрохимические реакции и интенсивное термическое воздействие, что позволяет формировать поверхностные слои с улучшенными характеристиками. В результате обработки сталь У9 демонстрирует чёткое разделение микроструктуры на три зоны: упрочнённый слой, переходный слой и основной металл. Упрочнённый слой, расположенный до глубины 400 мкм, характеризуется мелкодисперсной структурой. Она состоит из мартенсита и бейнита, с высокой твёрдостью (1400–1600 $HV_{0{\cdot}1}$). Этот слой обеспечивает превосходную износостойкость и устойчивость к механическим нагрузкам. Переходный слой, расположенный до глубины 700 мкм, служит буферной зоной, равномерно распределяя напряжения. Он характеризуется постепенным снижением твёрдости (800–1200 $HV_{0{\cdot}1}$) и изменением структуры за счёт

уменьшения содержания мартенсита. Основной металл, глубже 700 мкм, сохраняет исходную структуру с твёрдостью 400–600 $HV_{0.1}$, что обеспечивает его пластичность и долговечность. Полученные результаты показывают, что термоциклическая ЭПО значительно улучшает эксплуатационные свойства стали У9, создавая функционально градиентную структуру. Данная технология эффективна с точки зрения энергоэкономичности и может найти широкое применение в машиностроении и других отраслях, требующих высоких механических характеристик материалов.

Ключевые слова: термообработка, термоциклическая электролитно-плазменная обработка, электроразрядные явления, инструментальная углеродистая сталь У9, микроструктура

References

1 Kusmanov, S., Mukhacheva, T., Tambovskiy, I., Naumov, A., Belov, R., Sokova, E., & Kusmanova, I. (2023). Increasing Hardness and Wear Resistance of Austenitic Stainless-Steel Surface by Anodic Plasma Electrolytic Treatment. *Metals*, *13,* 872.

2 Belkin, P.N. (2011). Plasma Electrolytic Saturation of Steels with Nitrogen and Carbon. *Critical Reviews in Solid State and Materials Sciences, 36*(3), 174–190.

3 Aliofkhazraei, M., Aghdam, A.R., & Gupta, P. (2011). Nanofabrication by Cathodic Plasma Electrolysis. *Critical Reviews in Solid State and Materials Sciences*, *36*(3), 174–190.

4 Meletis, E.I., Nie, X., Wang, F.L., & Jiang, J.C. (2002). Electrolytic plasma processing for Cleaning and Metal coating of Steel Surface. *Surface and Coatings Technology*, *150,* 246–256.

5 Kusmanov, S.A., Smirnov, A.A., Kusmanova, Yu.V., & Belkin, P.N. (2015). Anode plasma electrolytic nitrohardening of medium carbon steel. *Surface and Coatings Technology*, *269,* 308–313.

6 Smirnov, A.A., Silkin, S.A., Belkin P.N., Dyakov I.G., Sevostyanova V.S., & Kusmanov S.A. & (2017). Povyshenie korrozionnoi stoikosti i iznosostoikosti stali 45 s pomoshchiiu anodnogo elektrolitno-plazmennogo azotirovaniia [Improvement of corrosion and wear resistance of 45 steel with anode plasma electrolyte nitriding]. *Izvestiia Vysshikh Uchebnykh Zavedenii. Seriia "Khimiia i Khimicheskaia Tekhnologiia" — News of Higher Educational Institutions. The series "Chemistry and Chemical Technology", Vol. 60(1), Issue1,* 81–86 [in Russian].

7 Dautbekov, M.K., Rakhadilov, B.K., Zhurerova, L.G., Kakimzhanov, D.N., Elistratov, S.L., & Segeda, T.A. (2022). A Technology for Making Detonation Coatings on Power Equipment Parts Made of Grade 12Kh1MF Steel. *Thermal Engineering*, *69*(12), 989–995.

8 Baizhan, D., Rakhadilov, B., Zhurerova, L., Tyurin, Y., Sagdoldina, Z., Adilkanova, M., & Kozhanova, R. (2022). Investigation of Changes in the Structural-Phase State and the Efficiency of Hardening of 30CrMnSiA Steel by the Method of Electrolytic Plasma Thermocyclic Surface Treatment. *Coatings*, *12*(11), 1996.

9 Rakhadilov, B.K., Berdimuratov, N.E., Zhurerova, L.G., Bayatanova, L.B., Kurbanbekov, Sh.R., & Satbayeva, Z.A. (2023). Study of the VAC of the EPCTT process with varying electrode parameters. *Bulletin of the University of Karaganda-Physics*, *3*(111), 136–142. DOI: https://doi.org/10.31489/2023PH3/136-142.

10 Zhou, L., Miller, J., Vezza, J., Mayster, M., Raffay, M., Justice, Q., Al Tamimi, Z., Hansotte, G., Sunkara, L.D., & Bernat, J. (2024). Additive Manufacturing: A Comprehensive Review. *Sensors*, *24*(6), 2668. DOI: https://doi.org/10.3390/s24092668.

11 Belkin, P.N., Yerokhin, A.L., & Kusmanov, S.A. (2016). Plasma electrolytic saturation of steels with nitrogen and carbon. *Surf. Coat. Technol*, *307*, 1194–1218.

12 Kusmanov, S.A., Kusmanova, Y.V., Smirnov, A.A., & Belkin, P.N. (2016). Modification of steel surface by plasma electrolytic saturation with nitrogen and carbon. *Mater. Chem. Phys*, *175*, 164–171.

13 Zhan, S., Lyu, Z., Dong, B., Liu, W., & Zhao, Y. (2023). Cathodic Discharge Plasma in Electrochemical Jet Machining: Phenomena Mechanism and Characteristics. *Int. J. Mach. Tools Manuf*, *187,* 104015. DOI: https://doi.org/10.1016/j.ijmachtools.2023.104015.

14 Gupta, P., Manuf, J., Sharma, A.K., & Singh, I. (2024). Plasma Formation and Material Removal Characteristics in Microwave-Metal Discharge-Based Machining of AISI 304 Stainless Steel. *Process*, *124,* 1159–1179. DOI: https://doi.org/10.1016/j.jmapro.2024.06.069.

15 Satbaeva, Z.A. (2022). Strukturoobrazovanie v legirovannykh staliakh pri elektrolitno plazmennom poverkhnostnom uprochnenii [Structure formation in alloy steels during electrolytic plasma surface hardening]. *Doctor's thesis.* Ust-Kamenogorsk [in Russian].

16 Tang, W., Zhu, Y., Kang, X., & Mao, C. (2023). Experimental Investigation of Discharge Phenomena in Electrochemical Discharge Machining Process. *Micromachines*, 14, 367. DOI: https://doi.org/10.3390/mi14020367.

17 Asmael, M., & Memarzadeh, A. (2023). A Review on Recent Achievements and Challenges in Electrochemical Machining of Tungsten Carbide. *Archives of Advanced Engineering Science*, *2*(1), 1–23. DOI: https://doi.org/10.47852/bonviewaaes3202915.

Information about the authors

Laila, Sulyubayeva — PhD, Associate Professor, Senior Researcher of Scientific Research Center "Surface Engineering and Tribology", S. Amanzholov East Kazakhstan University, Ust-Kamenogorsk, Kazakhstan; e-mail: lsulyubayeva@gmail.com; ORCID ID: https://orcid.org/0000-0002-1924-1459

Dastan, Buitkenov — PhD, Leading Researcher of Scientific Research Center "Surface Engineering and Tribology", S. Amanzholov East Kazakhstan University, Ust-Kamenogorsk, Kazakhstan; e-mail: buitkenov@gmail.com; ORCID ID: https://orcid.org/0000-0002-0239-5849

Baizhan, Daryn — Senior Researcher of Scientific Research Center "Surface Engineering and Tribology", S. Amanzholov East Kazakhstan University, Ust-Kamenogorsk, Kazakhstan, 3rd year PhD of Shakarim University, Semey, Kazakhstan; e-mail: daryn.baizhan1@gmail.com, ORCID: https://orcid.org/0000-0002-9105-3129

Berdimuratov, Nurbol — Leading Researcher of Scientific Research Center "Surface Engineering and Tribology", S. Amanzholov East Kazakhstan University, Ust-Kamenogorsk, Kazakhstan; e-mail: nurbol.ber@gmail.com; ORCID ID: https://orcid.org/0009-0000-6880-6439

Nurmahanbet, Raisov (*corresponding author*) — Engineer of Scientific Research Center "Surface Engineering and Tribology", S. Amanzholov East Kazakhstan University, Ust-Kamenogorsk, Kazakhstan; e-mail: nurmakhanberraisov@gmail.com; ORCID ID: https://orcid.org/0009-0007-1698-957X

Almar, Zhumabekov — Doctor PhD of Physics, Associate Professor, Faculty Computer Science, Toraigyrov University, Pavlodar, Kazakhstan; e-mail: almar89-89@mail.ru; ORCID: https://orcid.org/0000-0003-2360-3747